UNIVERSITA' DEGLI STUDI DI ROMA
TorVergata
Dipartimento di Scienze e Tecnologie Chimiche

Consiglio Nazionale delle Ricerche
IMM - Istituto per la Microelettronica e Microsistemi
Sezione di Roma

Ph'D Thesis on

Materials for The Environment and Energy

(*XVII Ciclo*)

MESOPOROUS SILICA THIN FILM SYNTHESIZED BY SELF-ASSEMBLY PROCESSES OF NO-IONIC BLOCK COPOLYMERS AND THEIR APPLICATION AS SENSING MEMBRANE

Student MIO BERTOLO Johnny

Tutor Prof. INNOCENZI Plinio
Co-Tutor Dott. BEARZOTTI Andrea

A.A. 2001/2004

Contents

Introduction

During the three years of the PhD course on "Materials for the environment and energy", we have characterized and studied mesoporous silica thin films obtained by block-copolymers supramolecolar self-assembling processes. Moreover we have evaluated their possible applications as sensing membranes for chemical sensor devices: in fact, a control of pores dimension can enhance their selectivity to gas molecules that can be adsorbed on silica surface.

In sensor applications, the aim is optimization of several device features: for example output response maximization, absence of instrumental noise, selectivity, fast output variation for environmental changes. At this purpose it is fundamental a right choice of the sensing material that may interact with external environment. Our studies have been focused on humidity sensing material because the omnipresence of water vapours, their influence in several chemical processes (and therefore the importance of their monitoring), the necessity of a RH sensor device to correctly understand output response for other species sensors.

Because interactions between vapour molecules and sensing membrane are superficial ones, mesoporous material are very interesting since have porosity with wide surface. Moreover their pores dimensions and communicatibility favour accessibility trough capillary phenomena and their raise the number of vapour molecules that can interact with the sensing material. To interact with water molecules, silica choice is explain by its synthesis easiness and idroxide groups native richness.

In first chapter, meaning of some terms frequently used in the sensors field will be described and a brief overview of main research area will be showed.

In second chapter mesoporous material synthesis methods and their main related problem will be mentioned and briefly considered. Attention will be then focused on synthesis and application of ordered mesoporous metal oxide thin films, overall sensing properties of silica-based films.

In third chapter, block-copolymer templated films will be characterized as a function of the calcination temperature by Fourier Transform Infrared Spectroscopy (FT-IR) to obtain compositional informations, Low Angle X-Ray Diffraction (LAXRD), Grazing Incidence

Small Angle X-ray Scattering (GI-SAXS), X-Ray Energy Dispersive experiment (EDXD and reflectometry) to obtain structural characterization.

In last chapter we will describe the substrate processing and the sensor devices production. We will study the sensors response both to relative humidity than alcohols vapours changes using our designedly testing apparatus. We will at last study electrical properties and conduction phenomena in the sensing membrane trough Electrochemical Impedance Spectroscopy (EIS) measurements.

Chapter 1

Gas Sensors

Introduction

The aim of sensors research and development is to obtain the optimization of their sensoristic properties like sensitivity, stability, selectivity and resolution (SSSR). All these properties must be considered together to evaluate the sensor quality and they are strictly related to physic-chemical nature of measurable properties chosen like response of sensor device, to their transduction process in electrical or optical signal, to electronic circuits useful in response elaboration and sensor conditioning.

Chemical sensoristic studies concentrate their attention on unsolved problems related to SSSR and above all to selectivity. Chemical sensor is defined as a device able to change an electrical or optical property in function of a chemical quantity variation (like concentration of a chemical species) in the environment. A sensor highly selective is said *specific* and its response is just related to an only chemical species concentration. If a sensor isn't a specific one, it is not possible to directly go back to concentration value.[1]

In chemical sensors, selectivity often clashes with its reversibility, which is another important parameter to consider in sensor development. Reversibility is sensor ability to spontaneously come back to initial conditions when input measurand has stopped. Sensor working is based on chemically active material as interface between sensor and environment. This material is characterized by the presence of chemical sites that are able to capture (by chemical bonds) molecules on surface from outside. Sensor selectivity is strongly dependent on chemical bonds selectivity. Because coordination mechanisms are thermodynamically and

kinetically controlled, chemical bonds could be selective only if are strong and so not reversible ones.

In this chapter, meaning of some terms frequently used in the sensors field will be described and a brief overview of main research area will be showed.

1.1 Definitions of sensors properties

The continuous progress in microtecnologies and microelectronic with development in material science has sustained sensor area growth and improvement in chemistry, biology, medicine, surface science, nanotechnology, simulation tools and everyday life. Therefore is suitable to well understand meaning of key terms frequently used in the field of sensors.

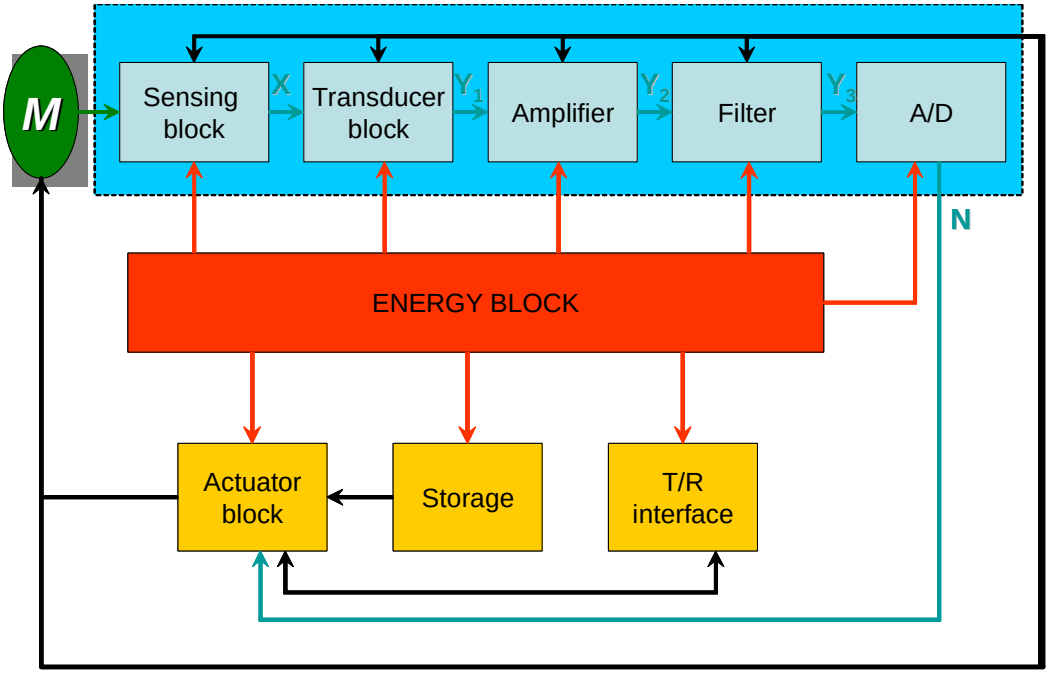

Figure 1 *Schematic block representation of a sensor device.*

Sensors structure can be simplified as in Figure 1. We recognize the generalized input *measurand* (M, which can be a physical, chemical or biological quantity), the transduction part, the preamplifier, the filter, the analogical to digital block, a microprocessor for data processing and storage, a display block, the transmission/receiver interface and the energy block allowing the operability of each part of sensor device.

1.1.1 Sensor Response Curve

The output response of a sensor is the representation of its output as function of the measurand applied to its input. For example if we consider a chemical sensor based on electrical properties variation in function of changes of input concentration of a given volatile compound, we can choose as output response the resistance R, the relative resistance R-R_0 (where R_0 is the resistance value if measurand is not applied, that is the reference value) or the relative change of the resistance $(R-R_0)/R_0$. Analogous definition are of great help if we consider conductance in place of resistance.

In the case of a quartz-based sensor, it is possible to use the frequency value (f), its relative value or relative changes; for a chemical MOSFET, with its gate sensitive to a given chemical species, output current intensity or output voltage are more obvious choices.

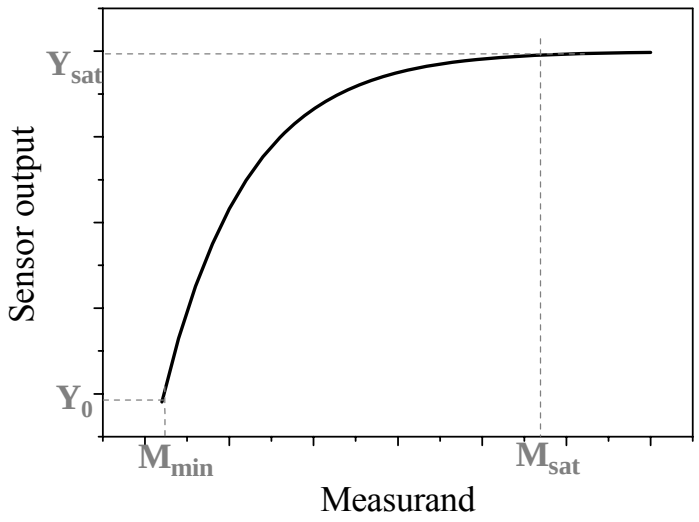

Figure 2 *Example of general response of a sensor device.*

In Figure 2, an example of a general output response (Y) in function of an input measurand (M) is shown: function start from Y_0 corresponding to minimum of M ad saturate to Y_{sat} above the saturation value M_{sat}.

1.1.2 Sensitivity

Sensitivity, by definition, point out the sensor output change with input variations. Because response curve as a rule is non-linear in character, sensitivity is usually obtained by a derivative procedure from the response function

$$S = \frac{\partial(Y - Y_0)}{\partial M} \qquad (1.1)$$

where Y could be conductance (G), resistance (R), frequency (f), output voltage (V_{out}) or current intensity (I_{out}). In Figure 3, an example of sensitivity curve (corresponding to response curve represented in Figure 2) is shown.

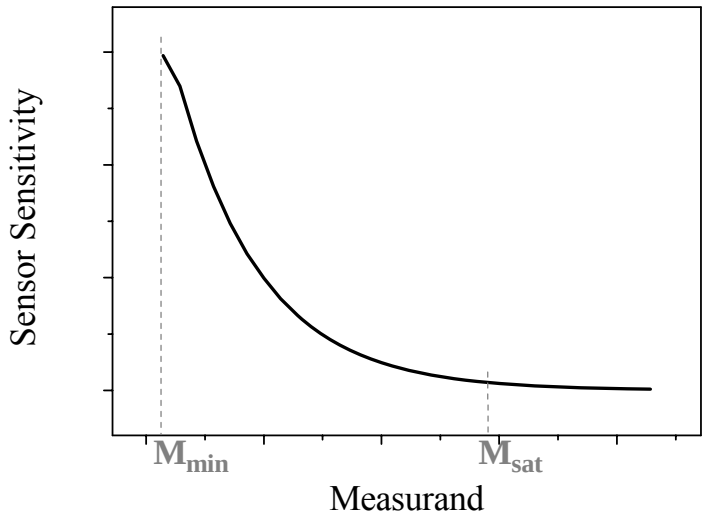

Figure 3 *Example of sensitivity curve for a sensor device.*

	N.L.C.	*L.C. with Offset*	*L.C. without Offset*	
^{i}S	$\frac{\partial X}{\partial M}$	$\frac{\Delta X}{\Delta M}$	$\frac{X}{M}$	***Internal Sensitivity***
^{T}S	$\frac{\partial Y_1}{\partial M}$	$\frac{\Delta Y_1}{\Delta M}$	$\frac{Y_1}{M}$	***Transduction Sensitivity***
^{A}S	$\frac{\partial Y_2}{\partial M}$	$\frac{\Delta Y_2}{\Delta M}$	$\frac{Y_2}{M}$	***Transamplification Sensitivity***
^{F}S	$\frac{\partial Y_3}{\partial M}$	$\frac{\Delta Y_3}{\Delta M}$	$\frac{Y_3}{M}$	***Analog Filter Sensitivity***
^{O}S	$\frac{\partial Y}{\partial M} = f\left(\frac{\partial Y_1}{\partial M} \quad \frac{\partial Y_2}{\partial M} \quad \frac{\partial Y_3}{\partial M}\right)$	$\frac{\Delta Y}{\Delta M}$	$\frac{Y}{M}$	***OVERALL SENSITIVITY***

Table 1 *Definitions of several kind of sensitivities for a sensor device.*

When the degree of non-linearity can be neglected, leaving the possibility of an offset, sensitivity can be simplified from a function to a single value (Table 1) if the interval of

measurand concentration to which the linearity behaviour is specified. Moreover, because sensor output depend on sensor structure (see Figure 1), its components influence also the overall sensitivity: its value change if we consider the output next to transducer, amplifier and filter, so we can define a transduction, transamplification or analog filter sensitivity. The internal sensitivity ${}^{i}S$ is defined as the related one to overall sensing block.

1.1.3 Noise, Resolution and Drift

Chemical, physical and biological quantities have unavoidable fluctuations that are the origin of electrical ***noise***, evaluated as the root mean square of the sensor output fluctuations. Different kind of noise may be present in given sensor, such as Johnson (thermal), shot, generation-recombination (g-r), contact, Flicker noise (*1/f*).

How much noise influences a sensor response can be quantified by ***resolution*** (*R*) obtained through a limit procedure

$$R = \lim_{Y \to Y_{noise}} \frac{Y}{S} = \frac{Y_{noise}}{S} \tag{1.2}$$

where sensitivity *S* and noise level Y_{noise} are function of the operating point. Resolution might be therefore specified with accurate specification of its operating point and for each sensor will be a working point corresponding to an optimal resolution value (i.e. a minimum value). Because noise, resolution cannot approach the zero value. Resolution evaluated in presence of the minimum noise value and maximum sensitivity level is defined as the "minimum detectable level" (*MDL*).

The ***drift*** is a slow change of the sensor output correlated to the aging of the sensing material and electronic components. It can be detected only through a long time observation and it reduce the accuracy of a sensor.

1.1.4 Selectivity

Sensor, even if is designed to be sensitive to a definite measurand always show often undesired internal sensitivities to other physical or chemical quantities (but in any recent applications this multiple sensitivity has been considered useful[2]). Therefore output signal of a sensor sensible to *n* measurand can be write (remembering the internal sensitivity definition) as a first order expansion

$$Y = Y_0 + \frac{\partial Y}{\partial X_1}\Delta X_1 + \ldots + \frac{\partial Y}{\partial X_n}\Delta X_n$$
$$= Y_0 + {}^{i}S_1\Delta X_1 + \ldots + {}^{i}S_n\Delta X_n \qquad (1.3)$$

and the ***selectivity*** toward the measurand X_i can be defined as

$$Sel_{X_i} = \frac{\frac{\partial Y}{\partial X_i}}{\frac{\partial Y}{\partial X_j}} \qquad (1.4)$$

considering all $j \neq i$. The (1.3) is valid if sensitivities are independent of each other, otherwise should also include the cross and second term of the expansion. In the independent selectivities case, selectivity can be estimated determining the response to one measurand per time in a given domain values.

In the dependent selectivities case, we must use an array of m sensor, with $m \geq n$. Response can be expressed as a system of m equation

$$\begin{cases} y_1 = f_1(x_1 \ldots x_n) \\ \ldots\ldots\ldots\ldots\ldots \\ y_m = f_m(x_1 \ldots x_n) \end{cases} \qquad (1.5)$$

and sensitivity is defined through the Jacobian matrix

$$S = \begin{bmatrix} \frac{\partial f_1}{\partial x_1} & \cdots & \frac{\partial f_1}{\partial x_n} \\ \vdots & & \vdots \\ \frac{\partial f_m}{\partial x_1} & \cdots & \frac{\partial f_m}{\partial x_n} \end{bmatrix} \qquad (1.6)$$

The maximum selectivity is achieved when the Jacobian matrix is diagonal; this correspond to the case of an array composed of n specific sensors.

1.2 Gas-sensor interactions

Interactions between a solid surface and a chemical species in gas phase can be both physical and chemical. Solid is defined as ***adsorbent***, molecules cling to surface are named ***adsorbed molecules***, if they seep into material are named ***absorbed molecules*** (Figure 4).

Molecules can be adsorbed on a site of the solid surface by interactions with all atoms of more superficial layers: the sum of these interactions give a total potential U (Figure 5). Bond nature determine the minimum potential value U_0, equilibrium distance r_0 and curvature of

potential hole where absorbed molecule is entrapped. If $U_0 >> kT$ absorption is mobile (or *unlocalized*), otherwise it is *localized*.

Physical interactions usually are controlled by weak forces (as example Van der Waals forces) between molecules and surface: bond energies are usually between 5 to 20 KJ·mol^{-1}. Process occurs without dissociations, it is reversible and the involved volatile component doesn't change its chemical identity.

Chemical interactions consist in chemical bond formation (typically with a strong covalent component) between the adsorbed molecule and a superficial site. Bond distance is similar to one present in a normal molecule and involved energies are from 40 to 600 KJ·mol^{-1}. Process involve chemical dissociation of adsorbed molecule and it is irreversible.

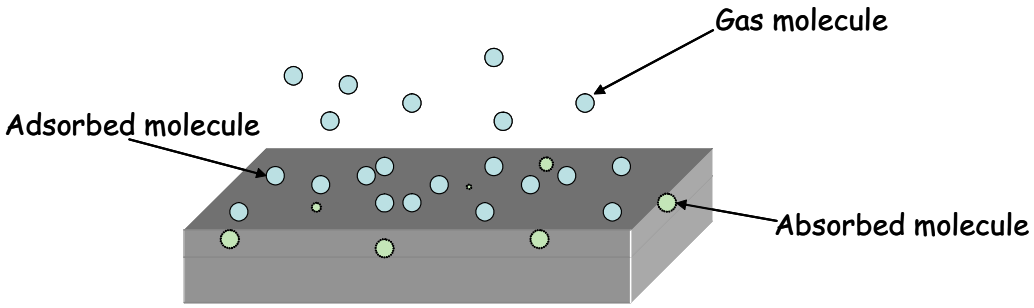

Figure 4 *Interactions between vapour molecules and a solid surface: adsorption and absorption*

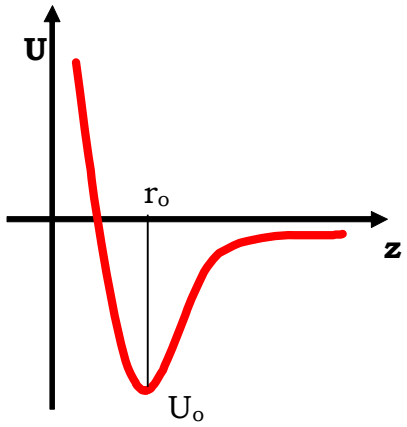

Figure 5 *Total Potential Energy U for vapour molecule-solid surface interactions.*

1.2.1 Langmuir model

Adsorbed molecules number ($\mathscr{N}$) is function of partial pressure p (or concentration), temperature and affinity between volatile compound and superficial chemical group

$$\mathscr{N} = f(p, T, k) \tag{1.7}$$

and average occupation density is the occupied sites vs. total ones ratio

$$\theta = \frac{N}{N_o} \tag{1.8}$$

Langmuir model (that is valid for localized adsorption) is based on the following hypothesis:

- Gas molecules are independent particles
- Constant value of temperature T (isothermal conditions)
- Interactions with gas molecule do not modify the absorbent lattice
- Each surface site can adsorb only one molecule
- All sites are equally probable and interactions are independent from occupation of near sites
- Equilibrium adsorption rate is equal to equilibrium desorption rate

Absorption rate can be kinetically expressed in fuction of gas concentration or partial pressure

$$R_{ads} = kC^X = k'p^X \tag{1.9}$$

where k and k' are the rate constants and X is the kinetic order. It is dependent on approaching rate of molecules to surface (and therefore on gas flux F) and on absorption probability S

$$R_{ads} = \overline{F} \bullet \overline{S} \tag{1.10}$$

Flux is the molecule number incident on surface unit for time unit and it is related to perfect gas density n by

$$\overline{F} = \frac{1}{4} n\bar{c} \qquad\qquad n = \frac{N}{V} = \frac{P}{RT} \tag{1.11}$$

Considering the Maxwell-Boltzmann distribution of rates in a gas

$$c = \sqrt{\frac{8k_B T}{m\pi}} \tag{1.12}$$

where m is molecular weight, k_B the Boltzmann constant ($1.38\ 10^{-23} JK^{-1}$) and R the ideal gas constant ($8.31\ JK^{-1}$). By substitution of rate c (1.12) in flux expression (1.11) and mole number of perfect gas equation, we obtain

$$F = \frac{p}{N_A \sqrt{2\pi m k T}} \tag{1.13}$$

where N_A is the Avogadro number (6.02 10^{23} mol^{-1}). Therefore molecular flux F is directly proportional to gas pressure p.

Absorption probability S is a property of absorbed substance related to absorbent substrate and its value is between 0 and 1. It is related to several factors, as example gas concentration or existence of an activation energy barrier E_a for absorption process: a general expression is

$$S = f(\theta) e^{-\frac{E_a}{RT}} \tag{1.14}$$

where $f(\theta)$ is a function of free sites number. Therefore absorption rate (1.10), using equation (1.13) and (1.14) can be expressed with

$$R_{ads} = \left(\frac{\partial \theta}{\partial t}\right)_{ads} = \frac{f(\theta) p}{\sqrt{2\pi m k_B T}} e^{-\frac{E_a}{RT}} \tag{1.15}$$

that in simpler case (for $f(\theta)=N(1-\theta)$ and $T=cost$), becomes

$$R_{ads} = k_a p N (1-\theta) \qquad k_a = \frac{e^{-\frac{E_a}{RT}}}{\sqrt{2\pi m k_B T}} \tag{1.16}$$

where k_a is the absorption rate constant.

Analogously to absorption rate, we can use for *desorption rate* the expression

$$R_{des} = \left(\frac{\partial \theta}{\partial t}\right)_{des} = -k_d N \theta \tag{1.17}$$

and at equilibrium, poning absorption rate (1.16) equal to desorption one (1.17),

$$k_a p N (1-\theta) = k_d N \theta$$
$$k_a p N = k_d N \theta + k_a p N \theta$$

we obtain

$$\theta = \frac{k_a p}{k_d + k_a p} = \frac{Kp}{1+Kp} = \frac{p}{K+p} \tag{1.18}$$

that defines the ***Langmuir isotherm equation*** (Figure 6). Rearranging equation (1.18) to solve it for gas pressure,

$$p = K\frac{\theta}{1-\theta} \tag{1.19}$$

that is the saturation pressure value (the adsorbate concentration in gas-phase that need to completely cover absorbant surface) is directly proportional to $K = k_a/k_d$, like deduced from Figure 6.

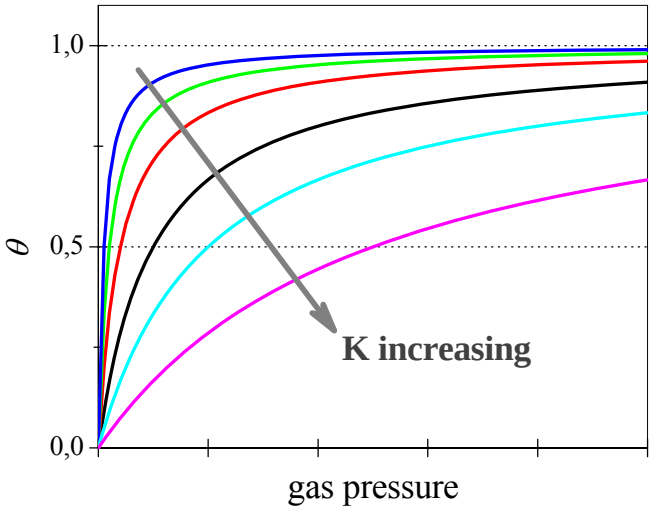

Figure 6 *Langmuir isotherm functions changing the kinetic absorption and desorption constants ratio K.*

Langmuir isotherm is suitable to describe low-pressure equilibrium: if adsorbate partial pressure increase over $1/4$ saturation value the hypothesis of single layer is not yet effective, therefore we have deviation from Langmuir model. BET theory describes a multilayers absorption

$$\theta = \frac{c\dfrac{p}{p_0}}{\left(1-\dfrac{p}{p_0}\right)\left[1-\dfrac{p}{p_0}(1-c)\right]} \tag{1.20}$$

where p_0 is adsorbate saturation pressure value and c a relative constant that quantify "resistance" to absorption compared to condensation process. Value of c constant is related to absorption and condensation enthalpies

$$c \cong \frac{e^{-\frac{\Delta H_{ads}}{RT}}}{e^{-\frac{\Delta H_{vap}}{RT}}}. \tag{1.21}$$

Multilayers absorption have no limits. BET isotherms have not saturation effects and doesn't assume the site independence and equivalence: experimental evidence of enthalpy increasing with θ value can be explained only with different site occupation probabilities. Energetically favourite sites are therefore occupied from the very beginning, the others only afterwards.

1.3 Water vapours measurements

Water vapour in air is known as *humidity* whereas it is called *moisture* in liquid or solid. Both humidity and moisture values are critical parameter in several industrial processes, so the necessity of their continuous monitoring.

Water vapour saturation pressure is function of temperature (611 Pa at 0°C, 2339 at 20°C, 7383 at 40°C) and it matches with water condensation. Otherwise, water vapour behaves as an ideal gas in air if it is far from this saturation point.

1.3.1 Humidity definitions

There are different ways to quantify the humidity value:

- ***Vapour pressure*** that is the water contribution to the total pressure expressed by the Dalton law:

$$P = p_{H_2O} + p_{N_2} + p_{O_2} + p_{other} \tag{1.22}$$

  where P is the total pressure given by all the partial pressure of species in the gas.

- ***Absolute humidity*** (or vapour concentration or vapour density) that is the water vapour mass for volume unit.
- ***Dew-point temperature*** that is the temperature at constant pressure to which gas get to saturation (if condensate becomes ice, temperature is called "***frost-point***").
- ***Relative humidity*** that is given by the ration between the vapour pressure and the saturated vapour pressure at same temperature:

$$RH = \left(\frac{p_{H_2O}}{p_s} \right)_{P,T} \times 100 \tag{1.23}$$

  where RH is the relative humidity (expressed as percent value) and p_s is the dew-point pressure (or frost point pressure, depending on considered conditions)

- ***Mixing ratio*** that is the ratio between water vapour and dry gas masses (if mass is related to wet gas mass, ratio is called "***specific humidity***").
- ***Molar fraction*** that is water vapour moles vs. total moles of all species present in the considered gas.

Water molecules, in fact, have asymmetrical distribution of electrical charges and can easily adsorb on solid surfaces, where they form mono- or multi-layers. They can modify many physical or chemical properties of materials (organic material structure, conductibility and weight of hygroscopic materials or chemical absorbents, electrical impedance of several materials, colour of chemical substance, refraction index in air or liquid phases, electromagnetic wave rate in air or solids, thermo-conductibility), therefore humidity sensors can be based on capacitive, resistive[3], hygrometric[4], optical[5] or gravimetric[6] measures.

1.3.2 Humidity sensing membrane

Humidity sensors have been widely studied in last decades. They are very interesting because water or water vapour are present everywhere.

Capacitive sensors are based on change of dielectric properties of sensing membrane (a thin film, for example) with exposure to water vapours. Sensor response is related to material hygroscopic behaviour and electrodes geometry[7]. Measured dielectric constant can be expressed by

$$\varepsilon = \varepsilon' - i\varepsilon'' = \varepsilon' - i\frac{\sigma}{\omega} \tag{1.24}$$

where ε' is the real dielectric constant and ε'' is the dielectric loss factor, σ is the conducibility and ω is the applied electrical field frequency. In a porous material (ceramic materials like Al_2O_3 as example)[8,9], capillary condensation with exposure to water vapours takes place in pores if their dimension is smaller than Kelvin radius[10]

$$r_K = \frac{2\gamma M_w \cos\theta}{\rho RT \ln\left(p_s / p\right)} \tag{1.26}$$

where γ is the superficial pressure, M_w the molar weight, θ the contact angle, ρ the liquid density. As several sensors based on water molecules adsorption, capacitive ones show a non-linear response vs. RH. An empirical relation that describes response trend is

$$\frac{C}{C_0} = \left(\frac{\varepsilon}{\varepsilon_d}\right)^n \tag{1.26}$$

where C_0 and ε_d are capacitance and dielectric constant in dry conditions and n is a factor related to dielectric morphology. A critical limit to ceramic based capacitive sensors is diffusion of possible contaminants (powers or aggressive agents) that can worse their performance if don't heat for impurities removal.[11]

Resistive sensors show an impedance variation with the RH value. For ceramic materials resistance (or impedance)[12] is valid the empiric relation

$$\log\left(\frac{R}{R_0}\right) = \frac{\log a - \log b \cdot (Rh)^n}{1 + \frac{b}{(Rh)^n}} \tag{1.27}$$

where R_0 is the resistance value in dry conditions, Rh is the relative humidity value and a and b are factors related to chemical composition and pores structure in ceramic material. A critical limit to ceramic based capacitive sensors is diffusion of possible contaminants (powers or aggressive agents) that can worse their performance if don't heat for impurities removal. Polymers sensing membrane are instead usable at high RH value for more narrow time or lower working temperature but they have a more linear response than ceramic films.

Gravimetric sensors[13] are piezoelectric plates (as quartz balance) covered by hygroscopic layer. Assuming that adsorbed vapour act as rigid body, resonance frequency is shifted with absorption (Sauerbrey equation)

$$\Delta f = -2\frac{1}{A}\frac{f_0^2}{\sqrt{\mu\rho}}\Delta m \tag{1.28}$$

where A is surface area, f_0 the resonance frequency in dry conditions, μ, ρ the density and Δm the mass variation because of absorption. These devices are suited to lower humidity concentrations: mass changes of 10^{-8} to 10^{-10}g.

Optical sensors can be based on amplitude E_0, polarization, frequency ω or phase φ measurement in electromagnetic wave propagation

$$E = E_o \cos(\omega t - \varphi) \tag{1.29}$$

For example, using optical fibres[14], vapour absorption on SiO_2 or TiO_2 can change the wave frequency

$$\Delta f = \frac{c}{2nd} \tag{1.30}$$

where c is velocity of light, d is sensing membrane thickness and n the refractive index (that change with vapour absorption).

1.4 Protonic conduction

1.4.1 Water ionization

Because of electric field fluctuations caused by nearby dipole librations[15] resulting from thermal effects, water molecules ionize. Ions may separate by means of the Grotthus mechanism but normally recombine within a few femptoseconds. Rarely (about once every eleven hours per molecule) the localised hydrogen bonding arrangement breaks before allowing the separated ions to return, and the pair of ions (H^+, OH^-) hydrate independently and continue their separate existence for an average time of 70 ms

$$H_2O \rightleftharpoons H^+ + OH^-$$

$$K_w = [H^+][OH^-] \qquad (1.31)$$

and finally they give a neutralization process.

Even if hydrogen ions are produced already hydrated (i.e. as hydronium ions, H_3O^+; also called oxonium or hydroxonium ions), it do not have any free existence as isolated protons, the above equations are better written as:

$$2\ H_2O \rightleftharpoons H_3O^+ + OH^-$$

$$K_w = [H_3O^+][OH^-] \qquad (1.32)$$

The concentrations of H_3O^+ and OH^- are taken as the total concentrations of all the small clusters including these species. Morover other water molecules are required to promote the hydrolysis, the equation below includes the most important.

$$4\ H_2O \rightleftharpoons H_5O_2^+ + H_3O_2^- \qquad (1.33)$$

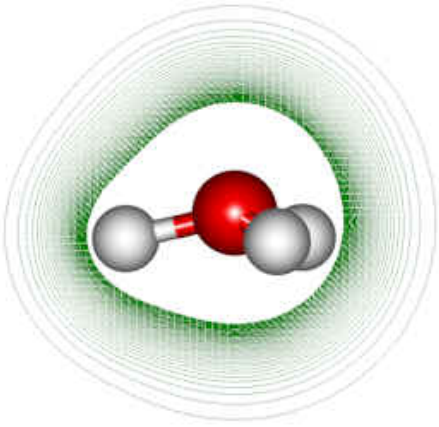

Figure 7 *Molecule structure of hydronium ion.*

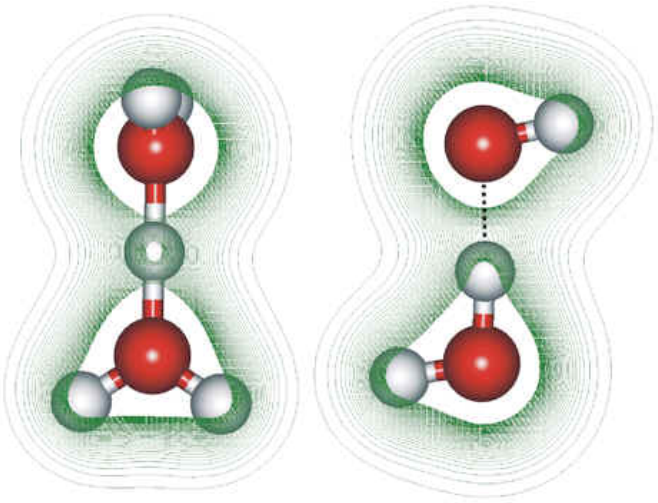

Figure 8 *Molecular structures of dihydronium ion and $(H_2O)_2$.*

The concentration of hydronium and hydroxide ions produced is therefore equal to the square-root of the ionization constant (K_w) as deduced from (1.32). K_w is strongly dependent on temperature: it increases with temperature (i.e. from 0.001 x 10^{-14} at -35°C (pH 8.5)[16], 0.112 x 10^{-14} at 0°C (pH 7.5), to 0.991 x 10^{-14} at 25°C (pH 7.0), to 9.311 x 10^{-14} at 60°C (pH 6.5)[17]) in agreement with the high positive standard free energy ($\Delta G° = 79.830$ kJ mol^{-1}at 25°C). In ice, where the local hydrogen bonding rarely breaks to separate the constantly forming and re-associating ions, the ionization constant is much: for example $K_w = 2 \times 10^{-20}$ at -4°C. Ionization also depends on the solute concentration and ionic strength: K_w goes through a maximum of about 2 x 10^{-14} at about 0.25 M ionic strength (using tetramethylammonium chloride, where possibly the stronger hydrogen bonding caused by clathrate formation encourages ionization) before dropping to a value of about 1 x 10^{-16} at 5 M, because higher concentrations disrupting the hydrogen bonding.

Ab initio calculations show that hydronium ion H_3O^+ (*ab initio* calculation using the 6-31G** basis set; high densities around the oxygen atoms have been omitted for clarity, Figure 7) has a flattened trigonal pyramidal structure (O-H bond length 0.961 Å, H-O-H angle 114.7°).The O-H bond length of the OH^- ion is calculated as 0.958 Å.

The hydronium ion is the most stable hydrated proton species in liquid water, being slightly more stable than dihydronium $H_5O_2^+$ represented in Figure 8 showing a section through the electron density distribution (*ab initio* calculation using the 6-31G** basis set with high densities around the oxygen atoms omitted for clarity): due to electronic delocalization in fact is preferred over nuclear delocalization[18]. In $H_5O_2^+$, all O-H bonds are the same length (0.949

Å) except the one involved in the hydrogen bond which is equally-spaced (1.18 Å; similar to that in ice-ten[19]- see phase diagram in Figure 9- and as found by neutron diffraction in some crystals)[20] mid way between the oxygen atoms. A slightly more stable form of $H_5O_2^+$ (above right) involving a longer O···O distance (2.40 Å) and hydrogen bond (1.32 Å) is found using the 6-31G** basis set. However, other more thorough *ab initio* treatments have found the equally-spaced hydrogen-bonded structure to be the global minimum by about 0.6 kJ/mol.

The presence of these three similar energy minima for the proton lying so close between the two oxygen atoms is surely the major reason for the ease of transfer of protons between water molecules; the proton moving between the extremes of triply-hydrogen bonded H_3O^+ ($H_9O_4^+$, 'Eigen cation') ions through symmetrical $H_5O_2^+$ ions ('Zundel cation')[21]. When the extra proton is shared equally between more than one water molecule, an approximate structure can be deduced considering resonance structures; for example, the two shared protons in $H_7O_3^+$ give rise to bond lengths half way between those in $(H_2O)_2$ and $H_5O_2^+$ (Figure 10)

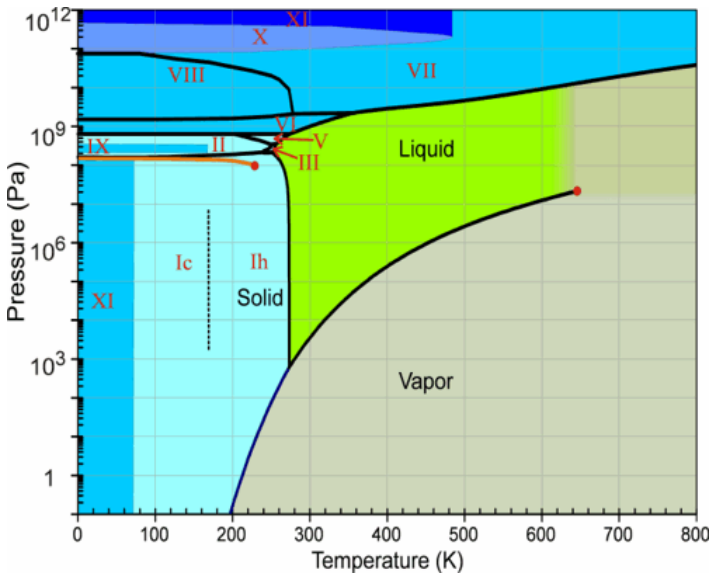

Figure 9 *Phase diagram of water.*

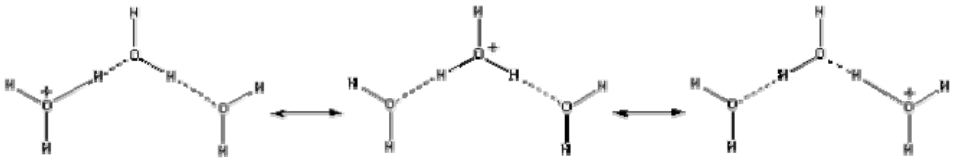

Figure 10 *Resonance structures for $H_7O_3^+$.*

and the three shared protons in $H_9O_4^+$ giving rise to bond lengths a third of the way between those in $(H_2O)_2$ and $H_5O_2^+$ (Figure 11).

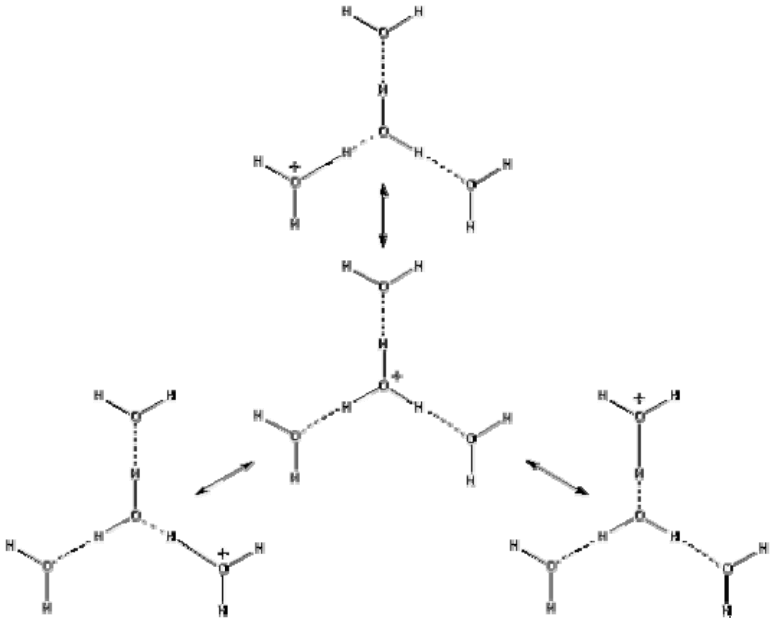

Figure 11 *Resonance structures for $H_9O_4^+$.*

In acid solutions, there will be many contributing structures giving rise to particularly broad stretching vibrations associated with the excess protons (e.g. magic number ions)[22].

The tetrahedral ion $H_7O_4^-$ (Figure 12) is probably the most stable hydrated hydroxide ion being slightly favored over $H_3O_2^-$. The O···O distance in $H_7O_4^-$ and $H_3O_2^-$ are slightly greater (~2.67 Å and ~2.50 Å respectively) and the O-H slightly shorter (~0.98 Å and ~1.05 Å respectively) than in $H_5O_2^+$. Also, the hydrogen atom lies significantly asymmetrically.

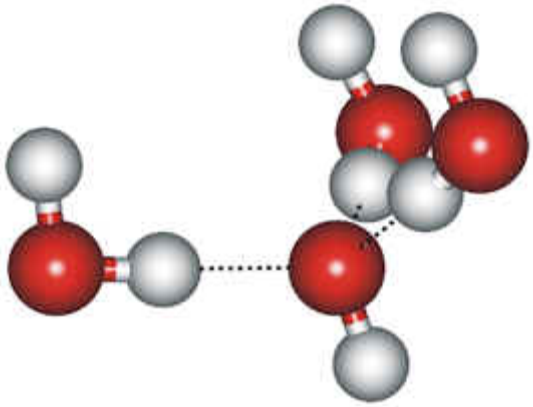

Figure 12 *Molecular structure of $H_7O_3^+$.*

It is generally thought that protons and hydroxide ions rapidly diffuse in liquid water, with protons diffusing almost twice as fast (and seven times as fast as Na^+). It should be recognized that these diffusivities are determined from movement in an electric field, where the special mechanisms described below are operational, and the true movements of the ions may be somewhat less, as can be recognized by the proton diffusional limitations that take place at the surface of some immobilized enzymes[23]. The mean lifetime of a hydronium ion (1 ps; about the same as that of a hydrogen bond) is such that the charge could be associated with over 10^7 molecules of water before neutralization.

1.4.2 Grotthus model

The Grotthus mechanism[24], whereby protons tunnel from one water molecule to the next via hydrogen bonding, is the usual mechanism given for proton mobility (note that aquaporin water channels deliberately re-orient water molecules to preclude such sequential hydrogen bonding so preventing proton transfer, in a similar manner to that causing the ions (H^+, OH^-) to initially separate on auto-ionization) as shown in Figure 13.

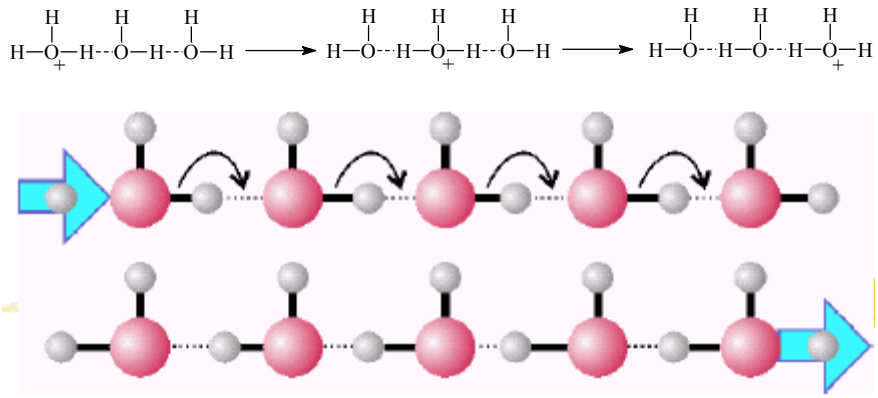

Figure 13 *Proton transfer from a water molecule to a near one described by Grotthus mechanism.*

A similar process can be given for hydroxide mobility (Figure 14).

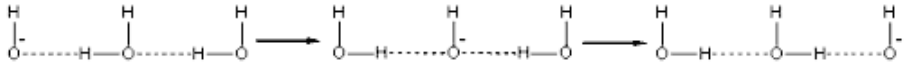

Figure 14 *Hydroxide transfer from a water molecule to a near one described by Grotthus mechanism.*

In the Grotthus model of aqueous proton transport, H_3O^+ transfers one of its protons to a recipient H_2O molecule in its first coordination shell, which thereafter passes a different proton to a further recipient water molecule, and so on. For the recipient H_2O to become a three-coordinated H_3O^+ ion, it has to change from the average hydrogen-bond coordination number of four to only three. Some have speculated[25] that the rate-limiting step involves the breaking of an H bond to the O atom of the recipient H_2O molecule before the proton transfer. This is supported by classical and quantum molecular dynamics simulations[26, 27]. The need for the recipient H_2O molecule to have a lower than usual hydrogen-bond coordination number is exactly analogous to the role of the two-coordinated dangling-O molecule on the ice surface.

The concept of hydrogen-bond coordination numbers helps us to understand proton transport in water. The simplest view of a hydrated proton is the H_3O^+ ion, which has an average coordination number of three. In order to migrate the ions must be associated with hydrogen bonded clusters; the stronger and more extensive the cluster, the faster the migration (e.g. hydronium mobility in hexagonal ice at -10°C is twenty times as fast as in water at 25°C). Stronger hydrogen bonding causes the O···O distance to be shorter, so easing the further shortening required for transfer. A limiting factor in mobility for both ions is the breakage of an outer shell hydrogen bonds. As a first step, this enables the hydrogen to transfer from H_3O^+ or, as a last step, the release of water by the newly formed hydroxide ion in $H_7O_4^-$ [18]. Both transfers involve the additional energy requirements of stretching the outer hydrogen bonds due to the contraction of the O···O distance.

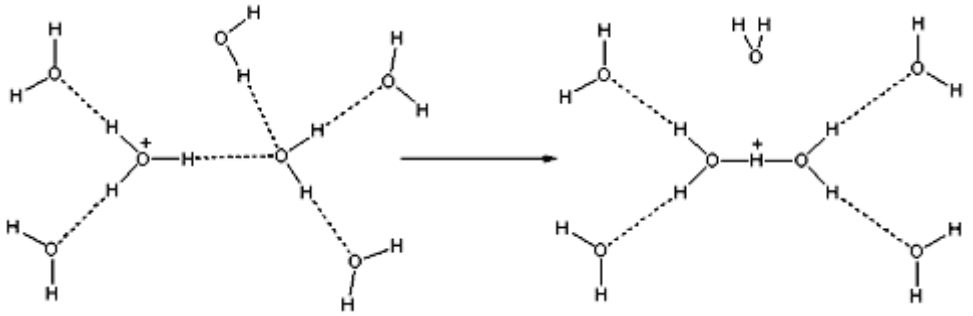

Figure 15 *Proton transfer in protonated trimer $H_7O_3^+$.*

The symmetrical structure during proton transfer (Figure 15), involving a triangular arrangement of water molecules, has been found in the protonated trimer ($H_7O_3^+$)[28].

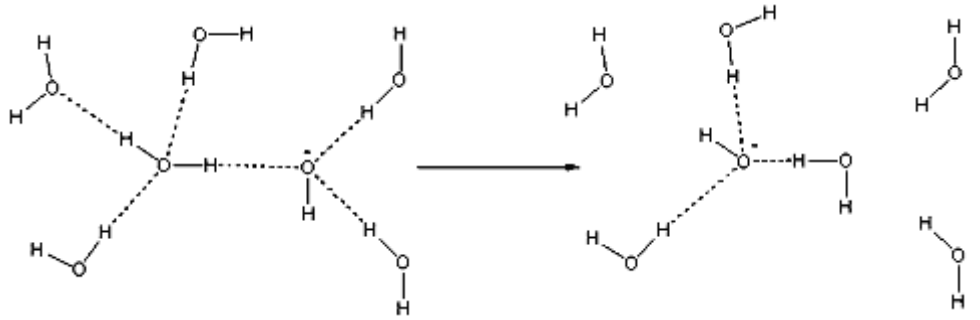

Figure 16 *Hydroxide transfer in $H_7O_4^-$.*

The reduced mobility of the hydroxide ion, over the hydronium ion, may be due to the extra activation energy required for the hydrogen atom to jump the gap between the two oxygen atoms and the loss of two further hydrogen bonds from $H_7O_4^-$ as it closes up to form $H_3O_2^-$ prior to transfer (Figure 16).

Recent theory has focused on the interplay between the triply coordinated hydronium $H_3O^+(H_2O)_3$ (the 'Eigen cation') and $H_5O_2^+$ (the 'Zundel cation'). In the latter, the proton is bound between two water molecules with 'stretched' bonds.

Researchers at the Pacific Northwest National Laboratory have experimental evidence that has overthrown the Grotthus model of proton transport in crystalline water (such as ice). The model assumed the apparent proton movement was temperature independent, and that could occur even at zero K. Theoreticians had reservations about the model. The polarity of a water molecule changes when a water molecule accepts a proton and becomes a hydronium ion, causing the molecule to reorient itself. In theory, neighbouring molecules would reorient in such a way that the negatively charged ends would all point to the positively charged proton (and hence each other), creating a negatively charged well from which the proton could not escape. Energy would be required to reorient the water molecules back to a state that facilitated proton transport. Thus, the theorists argued, the tunnelling could not take place at very low temperatures.

References of Chapter 1

1. J. Gardner and P.Barlet, *Sensors and sensory systems for an electronic nose*, Kluver Acd. Publ., Dordrecht (Holland), **1992**
2. C. Di Natale, A. Mantini, A. Macagnano, D. Antuzzi, R. Paolesse, A. D'Amico *Physiological Measurement.* **1999** 20 1
3. W. Qu and J.U. Meyer*, Meas. Sci. Technol*. **2000**, 11, 1111-1118
4. K. Sager, G. Gerlach and H. Schmidt, *Sens. Actuators B* **1994**, 18, 85-88
5. M.N. Weiss, R. Srivastava and H. Groger*, Electron Lett*. **1996**, 32, *9*, 842-843
6. D.W. Galipeau, P.R. Story, K.A. Vetelino, R.D. Mileham, *Smart Mater. Struct.* **1997**, 6, 658-667
7. J.G. Korvink, L. Chandran and other, *Sens. Mater*. **1993**, 4, *6*, 323-335
8. T. Seyama, N. Yamazoe, H. Arai, *Sens. Actuators B* **1983**, 4, 85-96
9. E. Traversa, *Sens. Actuators B* **1995**, 23, 1335-1356
10. K. Bratzeler, *Adsorption von gasen und dämpfen in laboratorium und technik*, Theodor Steinkopf, Desden **1944**
11. W.A. Clayton, P.J. Freud, R.D. Baxter, *Proceedings of the Conference on Humidity and Moisture*, Washington DC **1995**, 535-544
12. J.Ying, C. Wan, P. He, *Sens. Actuators B* **2000**, 63, 165-170
13. Y. Sakai, Y. Sadaoka, M. Matsuguchi, H. Sakai, *Sens. Actuators B* **1995**, 25, 689-691
14. F. mitschke, *Opt. Lett.* **1989**, 14, 967-969
15. P. L. Geissler, C. Dellago, D. Chandler, J. Hutter and M. Parrinello, *Science* **2001**, 291, 2121-2124
16. F. Franks, *Water: 2nd Edition A matrix of life*, Royal Society of Chemistry, Cambridge, **2000**
17. A. K. Covington, M. I. A. Ferra and R. A. Robinson, *J. Chem. Soc. Faraday Trans. I* **1977**, 73, 1721
18. N. Agmon, *Chem. Phys. Lett.* **2000**, 319, 247-252.
19. H. Suga, *Thermochim. Acta,* **1997**, 300, 117-126
20. F. F. Muguet, *J. Mol. Struct. (Theochem)* **1996**, 368, 173-196
21. D. Marx, M. E. Tuckerman, J. Hutter and M. Parrinello, *Nature* **1999**, 397, 601-604
22. M. P. Hodges and D. J. Wales, *Chem. Phys. Lett.* **2000**, 324, 279-288

23.M. F. Chaplin and C. Bucke, *Enzyme technology* (University Press, Cambridge, 1990) pp. 115-119

24.C. J. T. de Grotthuss, *Ann. Chim.* **1806**, LVIII, 54-74

25.N. Agmon, *Chem. Phys. Lett.* **1995**, 244, 456-462

26.D. Marx, M.E. Tuckerman, J. Hutter, M. Parrinello, *Nature* **1999**, 397, 601-604

27.T. Day, U. Schmitt, G. Voth, *J. Am. Chem. Soc.* **2000**, 122, 12027-12028

28.P. L. Geissler, T. Van Voorhis, C. Dellago, *Chem. Phys. Lett.* **2000**, 324, 149-155.

Chapter 2

Mesoporous Materials

Introduction

First materials with realized nanoporosity were zeolites, highly attractive because their catalytic properties but with narrow applications because too small pores. Since the early 1990s, the supramolecular templating and co-assembly have replaced the use of individual molecules to control the properties of porous materials.

Starting from a new class of materials discovered by Mobil Research Development Corporation using ionic surfactants[1], many efforts were been carried out to make the materials stable, expand the range of reachable pore size, extend the framework composition and examine new supramolecular templates[2]. As a result of these studies, it is at the present possible to obtain mesoporous or mesostructured materials with pore size from 2 to 50 nm. Moreover, different chemical compositions of the final material are achievable: metal oxides, transition metal oxides[3], metal sulphides, hybrid silica/organic compound. For the large pore dimensions, high surface area (near to 1000 $m^2 g^{-1}$) and thermal stability, many interest there is either in using these materials as catalysts and supports or in developing their electronic, optical or sensing applications. These factors certainly can improve the overall properties of a sensor device based on mesoporous oxides. In particular, the controlled accessibility of external chemical species to the pore surface could allow reaching a greater sensing selectivity and the large specific area improves the response to vapour concentration changes.

In this chapter mesoporous material synthesis methods and their main related problem will be mentioned and briefly considered. Attention will be then focused on synthesis and

application of ordered mesoporous metal oxide thin films, overall sensing properties of silica-based films.

2.1 Sol-gel process technology and chemistry

Silicon esters are compounds that contain oxygen bridge from silicon to an organic group (i.e. ≡Si-OR). If organic silicon compounds contain four oxygen bridges are named as derivatives of orthosilicic acid $Si(OH)_4$: the most conspicuous material is *tetraethyl orthosilicate* $Si(OC_2H_5)_4$. An alternative organic nomenclature by which these compounds are named as alkoxy derivates is diffused: tetraethyl orthosilicate therefore becomes *tetraethoxysilane*. The most conspicuous property of metal alkoxides is ease of hydrolysis: speed of hydrolysis is generally proportional to the electropositive character of the metal or its ability to enter a hyper-coordinate state.

Applications for tetraalkoxysilane cover a broad range and can be classified according to whether Si-OR bond is expected to be hydrolyzed or not in the final product. Applications in which this bond is hydrolyzed (reactive applications) are as binders for refractories, resins, coatings, sol-gel glasses, cross linking agents and adhesion promoters. Application in which Si-OR bond remains intact include heat-transfer and hydraulic fluids. Lower molecular weight compounds are generally used in reactive application whereas higher molecular weight ones are associated with mechanical applications.

Tetraalkoxysilanes possess excellent thermal stability and liquid behaviour over a broad temperature range. Moreover generally exhibit low level of toxicity. They are often viewed as liquid sources of silicon dioxide (SiO_2):

$$Si(OR)_4 + nOH^- \leftrightarrow Si(OR)_{4-n}(OH)_n + OR^- \qquad \textit{hydrolysis}$$

$$\equiv Si\text{-}OH + HO\text{-}Si\equiv \leftrightarrow \equiv Si\text{-}O\text{-}Si\equiv \qquad \textit{condensation}$$

Silicon dioxide never forms directly by hydrolysis in an acid- or base-catalyzed condensation, but reaction progresses through intermediate ethoxy derivates of silicic acid and polyilicates until most or all of ethoxy groups are removed and a nonlinear network of Si-O-Si remains. Solution viscosity increases until gelation or precipitation. Acid-catalyzed hydrolysis generally proceeds more rapidly than base one and leads to more liner polymers: base-catalyzed hydrolysis has significant differences from this one in the rates of first and second alkoxy group hydrolysis. For binder preparation, diluted hydrochloric or acetic acids are therefore preferred. When more complete condensation or gelation is desired, wider range of catalysts (including moderately basic ones) are employed.

Tetraalkoxisilane are usually preferred to alkyl- and aryl-trialkoxysilane in silicon dioxide synthesis because Si-OR bond is more reactive than Si-C and it has four rather than three matrix coordination leading to more rigid structures. Change in physical properties in several coating applications need changes in the choice of precursors.

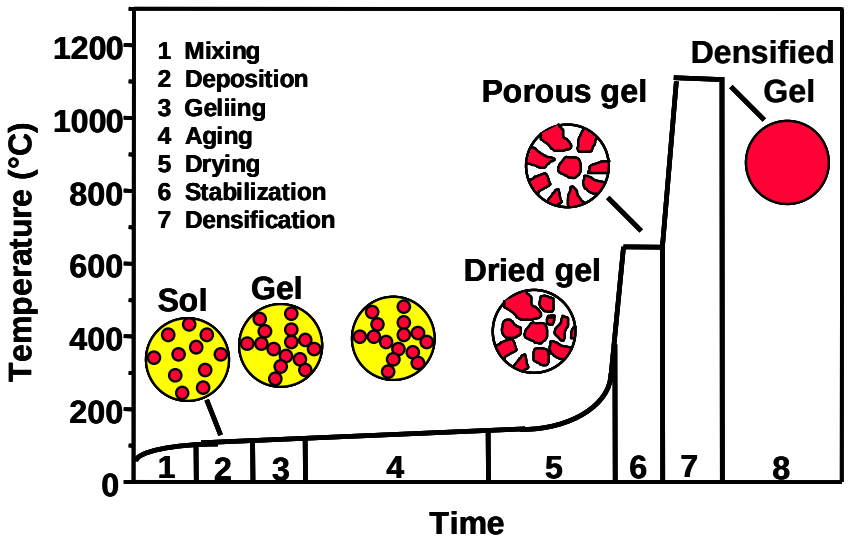

Figure 17 *Change in physical properties starting from a sol-gel solution in function of time and temperature.*

Complete hydrolysis of alkoxysilanes under controlled conditions is associated with sol-gel technology. Sol-gel method[4] consist to obtain metal oxide glasses or ceramics by hydrolyzing one or more chemical precursors that pass through a solution state and a gel state before being dehydrated to a glass or ceramic. Sol-gel route to oxides synthesis proceeds through three basic steps, here presented sequentially even if they occurs simultaneously in reaction solution:

1. ***partial hydrolysis*** of metal alkoxides to form reactive monomers;
2. ***poly-condensation*** of monomers to form colloid-like oligomers;
3. ***gelation*** and ***cross-linking*** that lead to a three-dimensional matrix.

Finally, trough suitable thermal treatments, dried, porous and densified gel can be obtained (Figure 17).

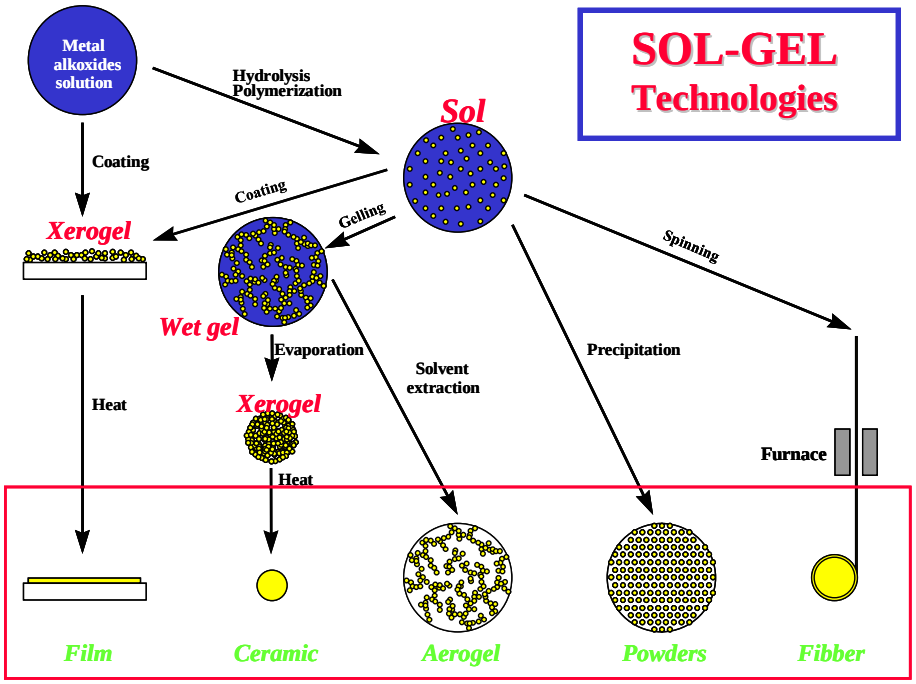

Figure 18 *Techniques based on sol-gel method.*

A variety of techniques have been developed to prepare fibbers, microspheres, thin films, fine powders and monoliths with several applications: protective coatings, cathalysts, piezoelectric devices, waveguides, lenses, superconductors, nuclear waste encapsulations, insulating materials and high strength ceramics (Figure18).

2.2 Self-assembly processes in mesoporous materials synthesis

Mesoporous materials form when inorganic oxides (e.g. silica) polymerize in the presence of surfactants, which serve as structure directing agents for the oxide framework: after calcination, porosity and eventually aligned pore orientation is retained.

The use of silica-organic interface interactions that are weak compared to other competing assembly forces, together with kinetic control of the silica polymerization makes it possible to simultaneously control the periodic mesostructure and particle shape. Electrostatic or hydrogen bonding interactions between the surfactant and the growing inorganic species usually leads to a phase separation into a surfactant-rich gel phase and a dilute isotropic solution in which polymerization to the final product occurs. The structure of the resulting inorganic solid depends sensitively on the reaction conditions such as concentration, temperature and pH. Moreover, during the synthesis phase transitions may occur in the

surfactant assembly thus complicating the situation even more[5]. During synthesis and processing and before the extensive silica polymerization, the inorganic/organic structures may readily undergo structural changes or transformation to relieve stress trough rotational displacements of the surface (disciplination defects): the use of weaker interaction at the silica/surfactant interface, like hydrogen-bonds, enhances precursor fluidity and synthesis processing

The early synthesis of mesoporous materials was carried out in basic media with anionic silica species and cationic surfactant. In this case the surfactant is positively charged and is balanced by a negative charge of the silica walls. The formation of the inorganic-organic composites is based on electrostatic interaction between the positively charged surfactants and the negatively charged silicate species. First, the oligomeric silicate polyanions act as multidentate ligands for the cationic surfactant head groups, leading to a strongly interacting surfactant/silica interface with lamellar phase. In second step the charge density matching (S^+I^- where S^+ = cationic surfactants and I^- = inorganic species), can directly lead to a phase transformation to, for example, hexagonal or cubic phase[6] (Figure19). Using the same surfactant but in an acid halide media, there are neutral silica walls with one halide ion associated with each surfactant ion in the pores: these can be removed, by a simple water/ethanol wash instead to use calcination or strong acid solution[7]. Until now, calcination is the more used method to remove organic templating agents, but often it leads to decrease long-range ordering of mesostructure or to partial collapse of mesoporous channels. Moreover, calcination often produces a great deal of CO_2 gases and organic compounds. Solvent extraction is a good alternative, not only because it is environmentally friendly and the surfactant could be recycled, also because the mesostructure could be easily maintained after this treatment[8].

The preferred shape of self-assembled surfactant molecules in the final material depends on the effective mean molecular parameters that establish the value of the packing parameter *g*. This parameter is defined as

$$g \equiv \frac{V}{a_0 l_c} \qquad (2.1)$$

where V is the effective volume of the hydrophobic chain, a_0 is the mean aggregate surface area per hydrophilic head group and l_c is the critical hydrophobic chain length. The parameter g depends on the molecular geometry of the surfactant molecules, such as the number of

carbon atoms in the hydrophobic chain, the degree of chain saturation and the size and charge of the polar head group.

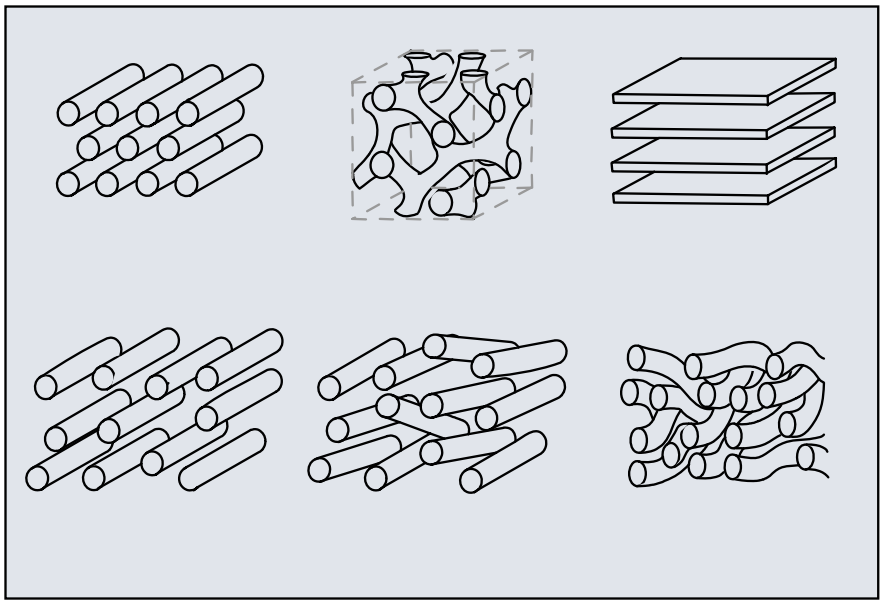

Figure 19 *Examples of possible mesophase structure by self-assembly processes.*

g	**Expected structure**
⅓	Cubic (*Pm3n*)
½	Hexagonal (*p6*)
½ - ⅔	Cubic (*Ia3d*)
1	Lamellar

Table 2. *Surfactant packing parameter g and expected structure of mesophase*

In addition, the effects of solution conditions, including ionic strength, pH, co-surfactant concentration, temperature, are implicitly in V, a_0 and l_c. In classical micelle chemistry, mesophase transition occurs when the g value is increased above critical values: the phase transitions also reflect a decrease in surface curvature from the cubic over the hexagonal to the lamellar phase (Table 2). Moreover, spherical aggregates are preferentially formed by

surfactants possessing large polar head groups: if the head groups are small and packed tightly, the aggregation number increases, resulting in rod-like or lamellar aggregates.

2.3 Block Copolymers

Considerable effort has been devoted to increasing the inorganic mesophase ordering length scale using different organic surfactant species. Especially non-ionic surfactants (alkyl polyoxyethylenes) and block copolymers (polyoxyalkylenes) are advantageous structure-directing agents compared to cationic surfactants because of their low cost, non-toxicity and variable hydrophobic/hydrophilic segment size. Compared with low molecular weight surfactants, amphiphilic block copolymers do not only allow the realization of mesoporous silica with larger pore sizes (up to 30 nm) and improve the ductility and elasticity of the resulting composite, but the slower relaxation times of copolymers also lead to an higher control over the structure thus allowing the exploitation of even kinetically hindered structures or micellar aggregates as templates.

There are a lot of kinds of non-ionic block-copolymers that are commercially available on the market, that are not expensive and that can be easily removed from the matrix. For simplicity, we can classify them as:

1) ***Di-block copolymers***: their molecular structure have one hydrophobic and one hydrophilic part,
2) ***Tri-block copolymers***: they have two hydrophilic terminal groups and a central hydrophobic chain,
3) ***Star copolymers***: in them there are more hydrophilic and one hydrophobic

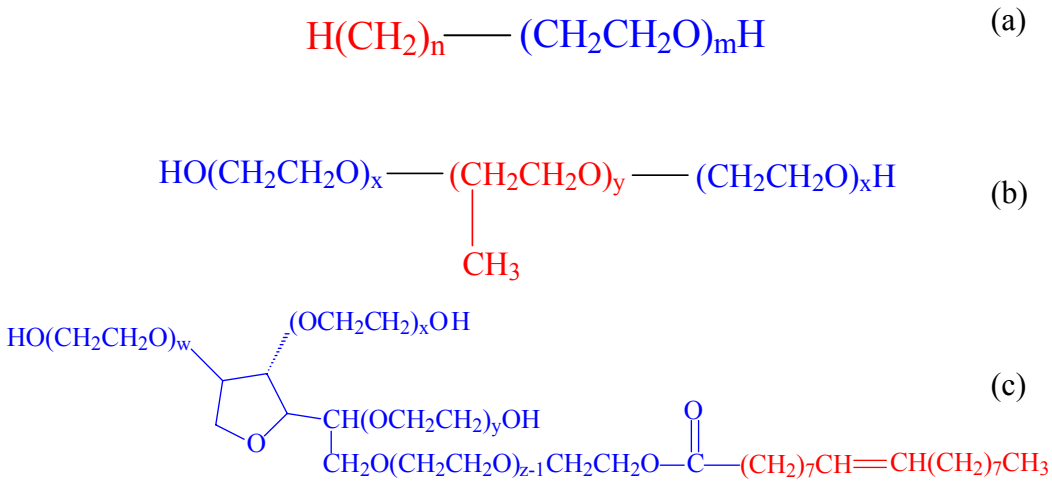

Figure 20 *Molecular structures of Brij (a), Pluronic (b) and Tween (c).*

terminations.

As example of these surfactant families, we can cite Brij (two-block linear), Pluronic (tree-block linear) and Tween (star copolymer): their general molecular formulas are represented in Figure 20.

In polar environment, because they have amphiphilic properties, the non-ionic block-copolymers reorganise to form macro-molecular structures (*micelles*) where the non-polar groups of each molecule are closed inside by the polar ones (Figure 21).

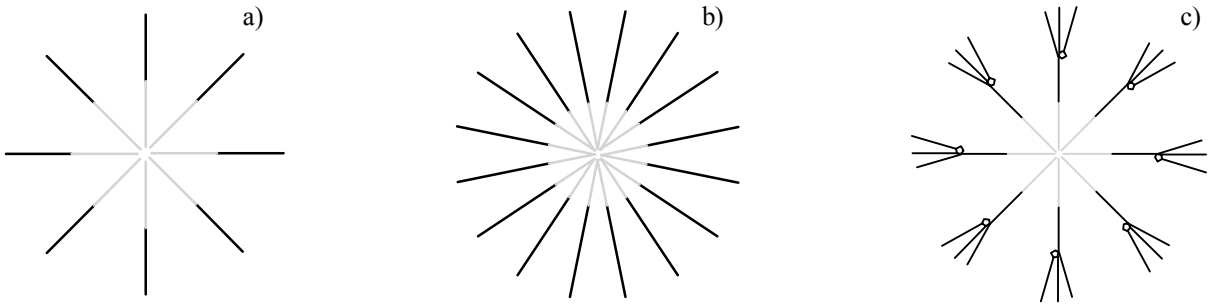

Figure 21 *Micellar section in polar environment: different self-assembled structures for Brij (a), Pluronic (b) and Tween (c). Black lines represent polar groups and grey lines apolar ones of copolymers.*

Moreover, these self-assembled structures can give rise to different mesophases (i.e. phase separation with dimension of the order of ten nanometres) according to the effective concentration of copolymer in solution and the particular types of used copolymer: via control of the concentration we can obtain cubic, hexagonal or lamellar mesophases[9] while dimension of pore can be controlled using different types of copolymers[10].

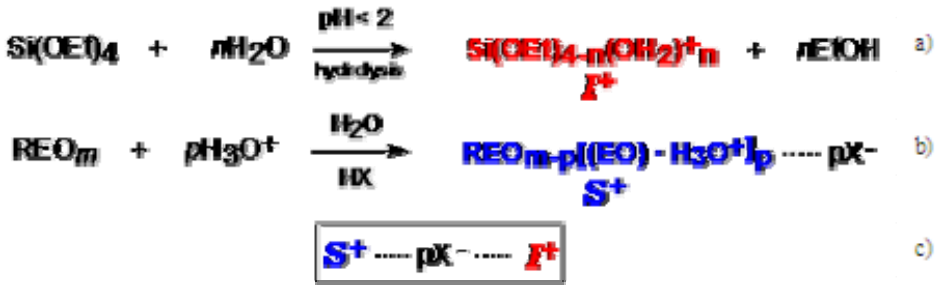

Figure 22 *Possible interaction between block-copolymer and silica precursor: hydrolysis of silica precursor (a), interaction of polar groups of copolymer with anionic species (b) and complessive interaction (c)*

Interaction between polar groups of block copolymers and inorganic precursors could be understood as illustrated in Figure 22. In fact, when non-ionic block-copolymer (REO) is introduced in a solution for the sol-gel process in acidic conditions, its polar block could react with hydronium ions and so it interact with anionic species in solution (X^- that come from acid dissociation). These anionic species could have task to be like a "bridge" between copolymer and hydrolyzed species of silica precursor (like, for example, tetraethylorthosilicate).

2.4 Ordered Mesoporous Metal Oxide Thin Films

Self-assembled mesostructured oxide thin films are potential candidates to replace non-porous silicon oxide as the standard insulating layers in microelectronics: the large porosity reduces the dielectric constant of the material compared to silicon oxide[11, 12], whilst does not modify the high thermal stability, the good mechanical properties, the low ion contents and

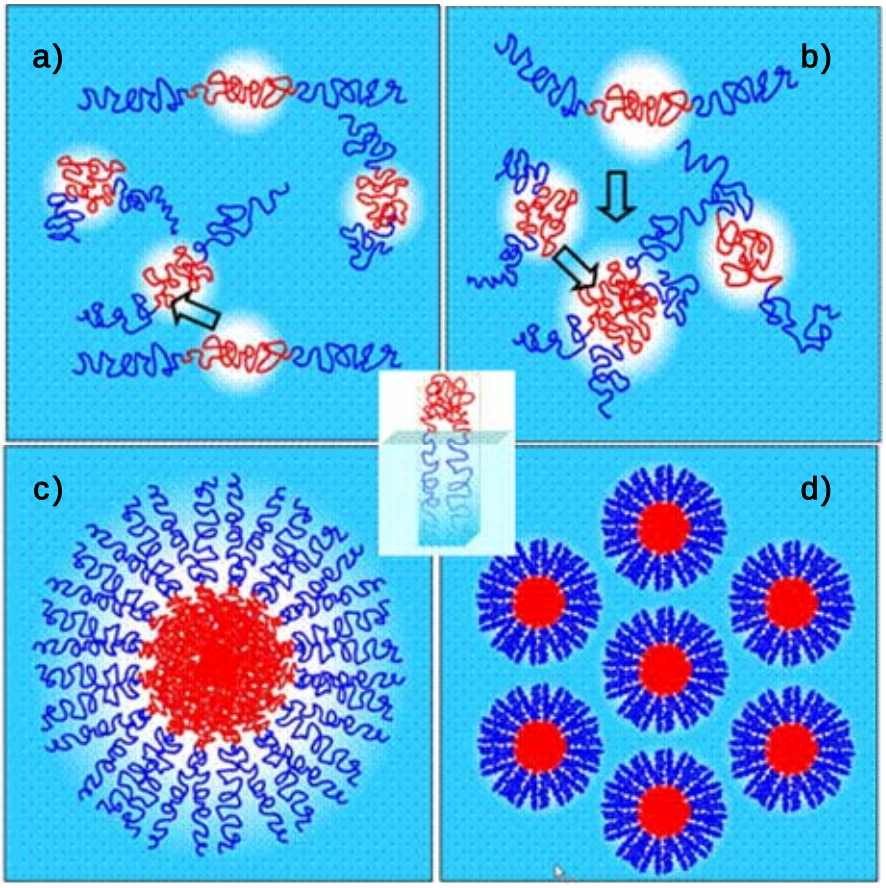

Figure 23 *Self-assembly process for no-ionic triblock copolymer in polar solution (a): apolar group interact each with other (b) giving rise to micelles (c) that rearrange in an ordered organic mesophase (d)*

the additional properties that have made silicon oxide the ultimate material for insulating layers[13].

Mesostructured oxide films of different compositions have attracted very much attention for their potential large impact in fabricating nano-engineered high performing materials. Examples are ultra-low dielectric films[11, 12, 14], low refractive index materials[14, 15, 16] and optical and electrochemical sensors[14, 17, 18, 19, 20]. Other interesting applications for self-assembled mesostructured oxide films are gas sensors[21] and separation membranes[22]. In this perspective it is important to achieve a macroscopically uniform orientation of the pores with engineered properties in terms of organization and surface control.

The discovery of simple chemical routes to synthesize mesostructured oxide materials has been of great interest to tailor pore sizes and shapes in powders and films of this class of materials, disclosing a large number of new applications. Several applications, in fact, require a full accessibility of the mesophase to make the most of the interfacial area of the material and a reversible response to environment changes without degradation. Many efforts have been addressed to improve the control of shape, dimensions, topology and accessibility of the pores during the preparation of self-assembled mesoporous films[23]. Furthermore, the possibility to functionalize the internal surface of the pores and to use mesostructured thin films as host matrix for functional nanoparticles increase their interest as sensors or protonic devices[2, 24]. Among the various methods to synthesize mesostructured materials, sol-gel chemistry used in combination with ionic surfactants[25] or block copolymers[26] as templating agents is the most used to prepare oxide thin films on different kind of substrates[27].

Mesostructured films are generally obtained via evaporation-induced self-assembly (EISA)[28], a deposition process which is driven by the preferential evaporation of the solvent, which is usually an alcohol.[29, 30, 27] The non-volatile surfactant and the inorganic species will be concentrated before reaching the equilibrium with atmosphere. The formation of the micelles and their organization in a liquid crystal template (Figure 23) can be adjusted, via the fine-tuning of the processing parameters, with the condensation of the inorganic framework, to give well-defined mesostructured materials

Thin films of surfactant-templated mesoporous silica have been prepared by a simple dip-coating or spin-coating method. In these methods an oligomeric solution of silica is prepared prior to the addition of surfactant. In many cases, coating is carried from a solution containing a highly volatile liquid so as to enhance the rate of film formation by rapid solvent evaporation.

Using the spin-coating method, the pore diameter could be controlled by surfactant chain-length as in bulk materials. In films with lamellar ordering, silica/surfactant ratio value was found to control the wall thickness of the silica. Macroscopic cracks, which were observed in films prepared by spin-coating, could be prevented by pre-treatment of the glass support with aluminium hydroxide: it was suggested that the pre-treatment invokes covalent bonds between the film and the substrate, and thus improves their adhesion.

Solvent evaporation, which increases the concentration of the solution to above the critical micellization concentration value, was found to induce mesophase formation during the dip-coating process. Different symmetries in films were reported in function of the initial surfactant concentration and surfactant type[31]: it was found that surfactants with a large polar head group lead to the formation of materials with three-dimensional symmetries.

Stable mesoporous silica thin films have been prepared by the above-mentioned methods in recent years, even if actually a good organic template removal is not simple: because of the thermal mismatch problem between substrates and films and the lower structure stability of the films than the powders, calcination often is not adequate.

An interesting field of application, where mesostructured oxide films are expected to play an important role in the next future, is in sensing. There is, in fact, an increasing request of cheap and reliable sensors to be used for environmental control. Next generation sensors require a high sensitivity coupled with a high resistance to external conditions where the sensor will be operating and new materials are always explored to increase the overall properties and performances. Notwithstanding the current state of research has not yet covered all the basic understanding, mesostructured oxide films have been used from the beginning to develop different types of sensors. There are some specific properties of mesostructured oxide films that are, in fact, particularly attractive such as the high specific area, the large porosity accessible from the external environment, the possibility to obtain through a flexible chemical synthesis route different oxide compositions and to functionalize the pore surface or doping the mesostructured oxide films with nanoparticles.

2.5 Mesostructured Silica Films as sensing membrane

After surfactant removal by calcination[32], chemical extraction or selective UV photocalcination[33], an ordered porosity in the range of 2-50 nm can be achieved within the material. Pore dimension can be controlled using different types of block copolymers. Cubic,

hexagonal or lamellar mesophases can be obtained controlling the copolymer concentration[9] and the processing conditions.Even mesostructured silica films, whose electrochemical response is expected to be quite low, can be used as the sensitive membrane for an electrochemical sensor. Water molecules, in fact, can be adsorbed from the external environment on a silanol-rich pore surface and their rearrangement in an ordered configuration ("ice-like" water) promotes the protonic conduction described by the "Grotthus model"[34]. Silica surface can moreover interact with alcohol vapours, so even in this case electrical conduction variation has been observed.

The basic mechanism enabling a silica sensor to detect humidity is the physisorption of water molecules on a chemisorbed layer of hydroxyl ions[35]. The process of chemisorption occurs at very low humidity levels and is unaffected by further changes in humidity. At higher humidity levels, however, the number of physisorbed layers increases. During the formation of the first physisorbed layer, a water molecule can interact with only one or two neighboring superficial hydroxyl groups: if two hydrogen bonds are formed, a proton may be transferred from an –OH group to a water molecule to form a H_3O^+ ion[36]. In a high-humidity environment, the dominant charge carriers (protons) are donated not only by H_2O, but also by the silica surface. The "water like" network (physisorbed layer consisting of singly bonded

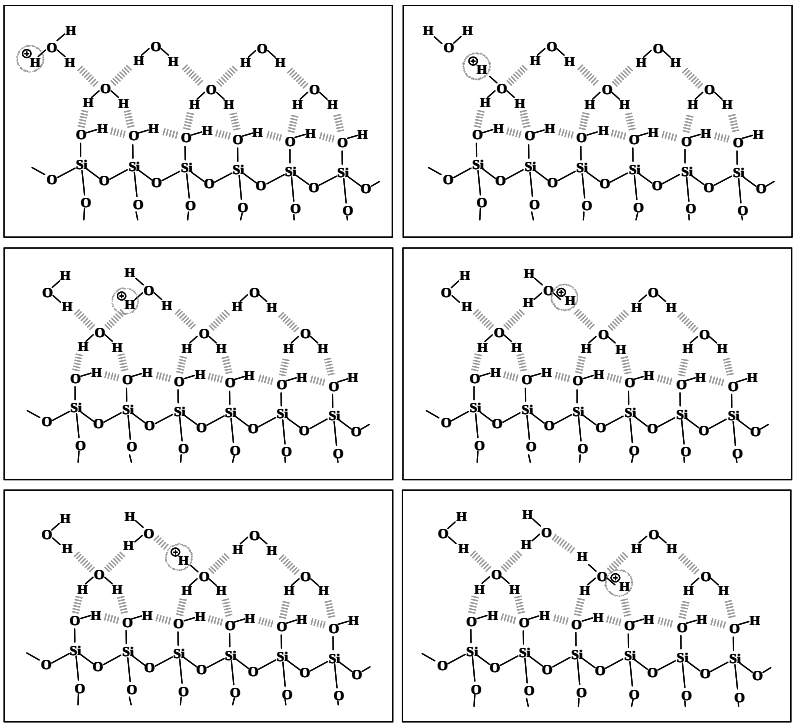

Figure 24 *Proton transfer in water layer absorbed on silica surface.*

water molecules), because of its high dielectric constant, is formed of dipoles that freely reorient under an externally applied field. At increasing humidity, the H^+ concentration also increases and they will be able to move in the material[37] (Figure 24).

Humidity sensors, in particular, are likely the type of sensors with the largest field of applications[38] and several types of humidity sensors are market available nowadays. There is still room, however, for developing better performing humidity sensors with very specific properties. Humidity sensors are, in fact, characterised by relative humidity (RH) range, sensitivity and operation temperature. High sensitive humidity sensors operating in a large range of RH, compatible with low production costs, are still lacking in the market. Mesostructured oxide films have been applied as membranes for humidity sensors[18] and have shown remarkably properties in terms of sensitivity and reliability of the RH measurements.

References of Chapter 2

1. C. T. Kresge, M. E. Leonowicz, W. J. Roth, J. C. Vartuli, J. S. Beck, *Nature* **1992**, *359*, 710-712
2. B. J. Scott, G. Wirnsberger, G. Stucky, *Chem. Mater.* **2001**, *13*, 3140-3150
3. P. D. Yang, D. Y. Zhao, D. I. Margolese, B. F. Chmelka, G. D. Stucky *Nature* **1998**, *396*, 152-155
4. C.J. Brinker, G.W. Scherer, *Sol Gel Science*, Academic Press, Orlando **1990**
5. W. Meier, *Curr. Op. Coll. and Int. Sc*. **1999**, *4*, 6-14
6. U. Ciesla, F. Schuth, *Micr. Mes. Mat.* **1999**, 27, 131-149
7. D. Zhao, P. Yang , Q. Huo, B. F. Chmelka, G. D. Stucky, *Curr. Op. Sol. St. and Mat. Sc.* **1998**, *3*, 111-121
8. Z. L. Hua, J. L. Shi, L. Wang, W.H. Zhang, *J. Non-Cryst. Sol.* **2001**, *292*, 177-183
9. P. C. A. Alberius, K. L. Frindell, R. C. Hayward, E. J. Kramer, G. D. Stucky and B. F. Chmelka, *Chem. Mater.* **2002** 14 3284
10. B. Smarsly, S. Polarz, M. Antonietti, *J. Phys. Chem. B* **2001**, 10473
11. S. Baskaran, J. Liu, K. Domansky, N. Koheler, X. Li, C. Coye, G. E. Fryxell, S. Thevuthasan and R. E.Williford, *Adv. Mater* **2000**, 12, 291
12. S. Seraji, Y. Wu, M. Forbess, S. J. Limmer, T. Chou and G. Cao, *Adv. Mater.* **2000**, 12, 1695
13. J. S. Beck, J. C. Vartuli, W. J. Roth, M. E. Leonowicz, C. T. Kresge, K. D. Schmitt, C. W. Chu, D. H. Olson, E. W. Sheppard, S. B. McCullen, J. B. Higgins and J. L. Schlenker, *J. Am Chem. Soc.* **1992**, 114, 10834
14. G. Wirnsberger, P. Yang, B.J. Scott, B.F Chmelka and G. Stucky, *Spectrochim. Acta A* **2001** 57, 2049
15. F.K. de Theijle, A.R. Balkenende, M.A. Verheijen, M.R. Balkanov, K.P. Mogilnikov and Y. Furukawa, *J. Phys. Chem B* **2003,** 107, 4280
16. G. Wirnsberger, P. Yang, H.C. Huang, B. Scott, T. Deng, G.M. Whitesides, B.F. Chmelka, G. D. Stucky, *J. Phys. Chem. B* **2001,** 105, 6307
17. P. Innocenzi, A. Martucci, M. Guglielmi, A. Bearzotti, E. Traversa and J.C. Pivin, *J. Eur. Cer Soc.* **2001**, 21 1985

18. P. Innocenzi, A. Martucci, M. Guglielmi, A. Bearzotti, and E. Traversa, , *Sensor Actuat. B.* **2001**, 76, 299

19. A. Bearzotti, J. Mio Bertolo, P. Innocenzi, P. Falcaro and E. Traversa*, Sensor Actuat. B.* **2003** in press

20. T. Yamada, H.S. Zhou, U. Uccida, M. Tomita, Y. Ueno, I. Honma, K. Asai and T. Katsube, *Micropor. Mesopor. Mat.* **2002**, 54 269

21**.** A. Cabot, J. Arbiol, A. Cornet, J. R. Morante, F. Chen and M. Liu, *Thin Solid Films* **2003**, 463, 64

22**.** G. Xomeritakis, S. Naik, C. M. Braunbarth, C. J. Cornelius, R. Pardey and C. J. Brinker, *J. Membrane Sci.* **2003**, 215, 225

23**.** S. Pevzner, O.Regev and R. Yerushalmi-Rozen, *Curr. Op. in Colloid & Interface Sci.* **2000**, 4, 420

24**.** F. Marlow, M. D. McGehee, D. Zhao, B. F. Chmelka and G. D. Stucky, *Adv. Mater.* **1999**, 11, 632

25. M. Klotz, P.Albouy, A Ayral, C. Mènager, D. Grosso, A. Van der Lee, V. Cabuil, F. Babonneau and C. Guizard, *Chem. Mater.* **2000**, 12, 1721

26. D.Grosso, A.R. Balkenende, P. Albouy, A Ayral, H. Hamenitsch, F. Babonneau, *Chem. Mater.* **2001**, 14, 1848

27. Y. Lu, R. Gangull, C. A. Drewlen, M. T. Anderson, C. J. Brinker, W. Gong, Y. Guo, H. Soyez, B. Dunn, M. H. Huang and J. I. Zink, *Nature* **1997**, 389, 364

28. C. J. Brinker, Y. Lu, A. Sellinger and H. Fan, *Adv. Mater.* **1999**, 11, 579

29. H. Yang, A. Kuperman, N. Coombs, S. Mamiche-Afara and G. A. Ozin, *Nature* **1996**, 379, 703

30. H. Yang, N.Coombs, O. Dag, I. Sokolov and G. A. Ozin*, J. Mater. Chem.* **1997**, 7, 1755

31. D. Zhao, P. Yang, D. I. Margolese, B. F. Chmelka, G. D. Stucky, *J. Chem. Soc. Chem. Comm.* **1998**, *22*, 2499-2500

32. A. Stein, B. J. Melde and R. C. Schroden, *Adv. Mater.* **2000**, 12, 1403

33. A. Hozumi, Y. Yokogawa, T. Kameyama, K. Hiraku, H. Sigimura and O. Takai and M. Okido, *Adv. Mater.* **2001**, 12, 985

34. N. Agmon, Chem. *Phys. Lett.* **1995**, 244, 456

35. E. Traversa, *Sens. & Act. B* **1995**, 23, 135

36. V. K. Khanna and R. K. Nahar*, Appl. Surf. Sci*. **1987**, 28, 247

37. O. K. Varghese, D. Gong, M. Paulose, K. G. Ong, C. A. Grimes and E. C. Dickey, *J. Mater. Res.* **2002**, 17, 1162

38. I.C. Kemp, Papers and Abstracts from the Third International Symposium on Humidity & Moisture (hosted by National Physical Laboratory, London, England, **1998**), vol.2 p.18

Chapter 3

Synthesis of Mesoporous Silica Thin films and their chemi-physical characterization

Introduction

At present, several types of self-assembled oxide films have been synthesised such as silica[1, 2, 3, 4], titania[5], zirconia and vanadia[6]. It has been also shown by different authors the possibility to obtain different pore topologies and dimensions by changing the organic template, which is generally an ionic surfactant or a block copolymer, and the synthesis conditions, for instance the humidity in the deposition room, the water/alkoxide ratio, the template concentration, and the aging time of the solution[7]. The synthesis of mesostructured films is, however, very much complicated by the difficult control of the process and the different parameters that can affect the final structure. Reproducibility of the results requires a deep understanding of the overall process and to set up a fabrication apparatus allowing a high control of the preparation conditions.

Silica mesostructured films have been produced using evaporation induced self-assembling processing via dip-coating. A block copolymer Pluronic F-127 has been used as the organic template and has been removed from the films by thermal calcination. The block-copolymer templated films have been characterized as a function of the calcination temperature by Fourier Transform Infrared Spectroscopy (FTIR) to obtain compositional informations, Low Angle X-Ray Diffraction (LAXRD), Grazing Incidence Small Angle X-ray Scattering (GI-SAXS), X-Ray Energy Dispersive experiment (EDXD and reflectometry) to obtain structural characterization.

3.1 Synthesis of mesostructured silica films

The synthesis of the precursor solution is illustrated in Figure 25. It was done at room temperature with ionic or non-ionic surfactants as structure-directing agents: cetyltrimethylammonium bromide (CTAB), two-block linear (Brij), three-block linear (Pluronic) and star-block copolymers (Tween). For each one, two different separate solutions were prepared; the first one, called the *stock solution,* was done by mixing

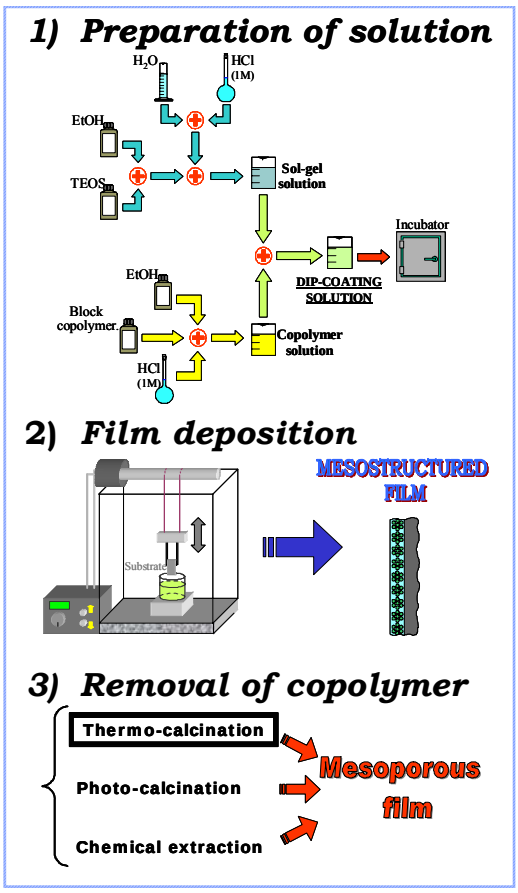

Figure 25 *Synthesis of mesoporous silica films by sol-gel method*

tetraethylorthosilicate (TEOS), ethanol (EtOH), H_2O and HCl. The second one, called the *templating solution*, contained a surfactant (CTAB, Brij-58, Pluronic F-127 or Tween-80), EtOH and a weakly acid aqueous solution (HCl). The stock solution was stirred for 1-2 hours to allow the hydrolysis of the silane units and then added to the templating solution. After 1-2 days of magnetic stirring the final solution was aged for 5-8 days. The surfactant

concentration was fixed at 5 wt% of the final solution for the linear-block copolymers (Briji-58 and Pluronic-127) and to 15 wt% for the star-block copolymer (Tween-80). For the cationic surfactant (CTAB)[8], the final molar ratios were TEOS/EtOH/H_2O/HCl/CTAB = 1:20:5:0.004:0.14. The solution was finally stirred at room temperature for 5 days.

Mesostructured silica films were deposited via-dip-coating in controlled conditions of humidity and temperature. Alumina and silicon were employed as substrate. All the depositions were performed at 30% RH, with a withdrawal speed of 20 cm min^{-1} and at 28°C. The films immediately after the deposition were fired at 150°C for one hour. Thermal treatments at higher temperatures were performed introducing the samples directly in the oven. The firing process was done in sequence, i.e. all the samples were fired at 150°C, then at 250°C and so on, up to 550°C.

3.2 FT-IR spectroscopy

The microstructural evolution of the films during thermal treatment, up to a complete removal of the organic phase, was observed by Fourier Transformed Infrared Spectroscopy (FTIR). Used instrument was a Perkin Elmer System 2000 FT-IR (resolution 4 cm^{-1}, 24 scansion for each spectrum). Spectra had been recorded in the 4500 – 450 cm^{-1} range (Figure

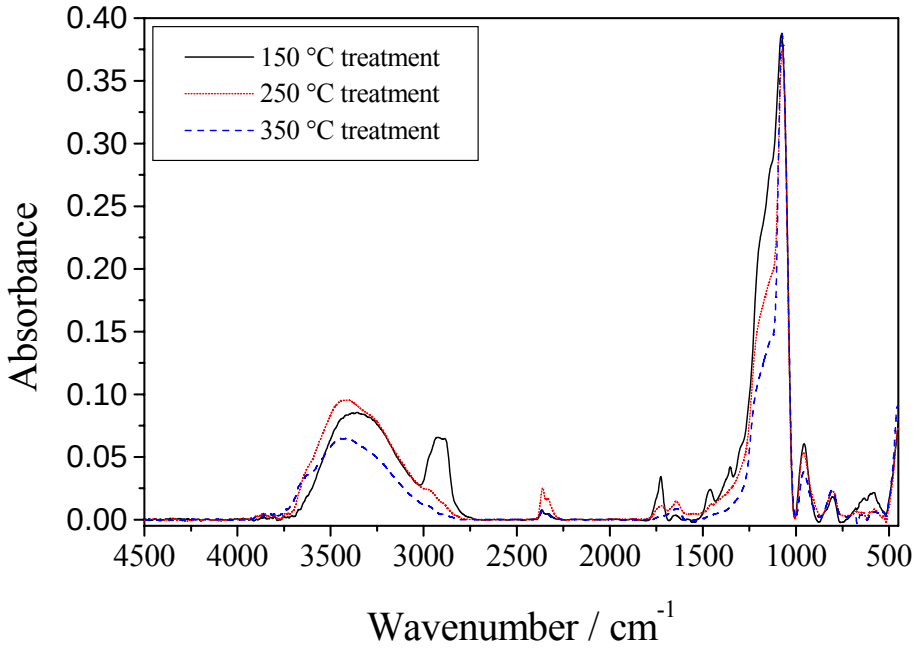

Figure 26 *FTIR spectra of the sample with Pluronic as templating agent treated at different calcination temperature*

26). Even if instrument works in transmittance (T), spectra will be here reported using absorbance (A) values obtained using

$$A = -\log T \qquad (3.1)$$

All analyzed sample has been prepared by dip-coating on silicon substrate.

The absorption band related to C-H mode vibration of the surfactant was clearly detected in the range 2700 – 3000 cm^{-1}. For example, for the sample containing Pluronic as templating agent, this band was complete absent after the 350°C thermal treatment (Figure 27). At 3000 – 3750 cm^{-1}, instead, there was the band of –OH groups (they are present at the surface of pore), at 1650 cm^{-1} the absorption of molecular water and finally at 500 – 1300 cm^{-1} the picks related to the silica polymerization.

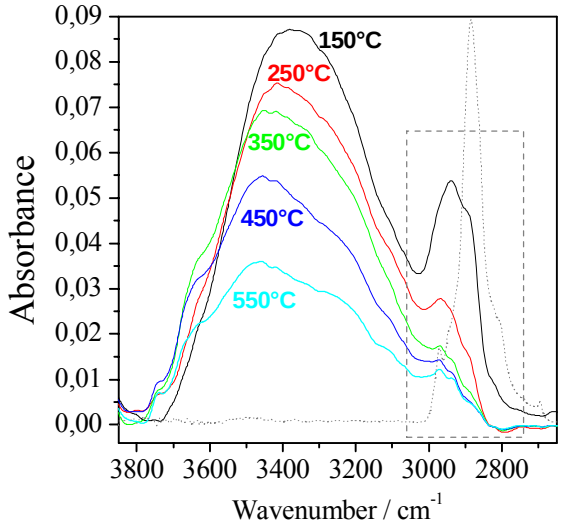

Figure 27 *FTIR absorption spectra in the range 3850 – 2650 cm^{-1} of mesostructured silica films calcined in air at different temperatures.*

Figure 27 shows the FTIR absorption spectra of silica mesostructured films in the range 3850 – 2650 cm^{-1}. Two overlapped regions of vibrational modes can clearly be distinguished. The first one in the lower wavenumber range (within the dot rectangle in Figure 27), due to absorption of organic groups in Pluronic F127, can be taken as a signature of the presence of the block co-polymer within the material, and a second one at higher wavenumber due to hydroxyls absorptions. This second broad band appears as composed of several overlapped bands assigned to different types of vibrational modes [9,10,11,12]. In particular, at the low wavenumber side three overlapped vibrational modes at 3743, 3676 and 3635 cm^{-1} are

observed (Figure 28). The bands, on the basis of the literature[9,10,13], are assigned as it follows: 3743 cm^{-1}, free single silanol groups; 3676 cm^{-1}, pairs of silanols mutually hydrogen bonded in linear configuration, where only one oxygen is participating in the hydrogen bonding (oxygen atoms form H-bonds with a hydrogen atom of an adjacent silanol); 3635 cm^{-1}, pairs of silanols mutually hydrogen bonded in linear configuration, where only one hydrogen is participating in the hydrogen bonding (hydrogen atoms form H-bonds with an oxygen atom of an adjacent silanol). These bands appear only after thermal treatments larger than 150°C; at this temperature these absorption bands are not observed, in fact, in the films.

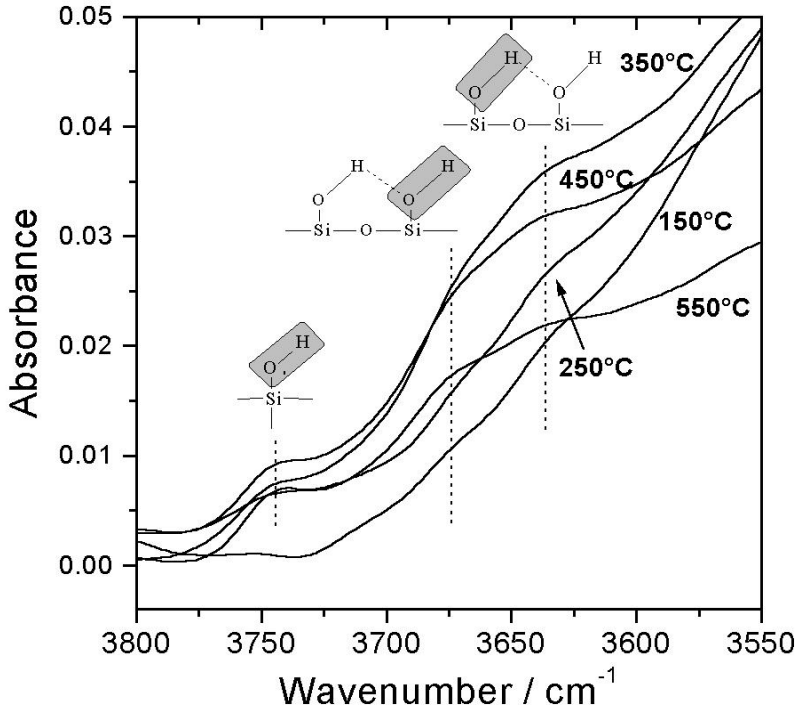

Figure 28: *FTIR absorption spectra in the range 3800 – 3550 cm^{-1} of mesostructured silica films. In this range different silanol species are detected: 3743 cm^{-1}, free single silanol groups; 3676 cm^{-1} and 3635 cm^{-1}, pairs of silanols.*

The three bands increased also in intensity from 250 to 450°C, after this temperature they reversed the trend. The block-copolymer is progressively eliminated with the increase of the temperature of calcination, but weak traces of Pluronic F-127 are still observed even after annealing at 550°C (Figure 27). The absorption maximum of the broad band peaking around 3370 cm^{-1} is progressively shifted to higher wavenumbers and decreases in intensity at larger temperatures of annealing. This band is due to hydrogen bonded silanols in chains that contain

more than a pair of mutually H-bonded OH groups. At 3340 cm^{-1} the overlapping of a broad band assigned to OH stretching mode of water molecules[14] (ν(OH)) is observed (Figure 27), the presence of this band is in accordance with the detection of the 1640 cm^{-1} band due to bending vibration (δ(OH)) of water[15]. To observe the different components of OH vibrational modes of water we have, however, preferred to select the O-H bending region of water at around 1640 cm^{-1}. In this interval, following the literature, three different vibrational components due to molecular water can be observed: water molecules that aggregate with strong hydrogen bonding (~ 1676 cm^{-1}) (type I), water molecule clusters with moderate intensity of hydrogen bonding (~ 1654 cm^{-1}) (type II) and water molecules that interact with each other with weak hydrogen bonding (~ 1592 cm^{-1}) (type III). Generally this last type of hydrogen bond is so weak that the water involved with this bonding can be considered like "free" water, whilst a lower absorption wavenumber is an indication of a decrease in the strength of the hydrogen bonding.

The 1740 – 1550 cm^{-1} region is shown in Figure 29**,** the three components of water bending modes are observed with different intensities in samples calcined at the various temperatures. In particular, in the samples fired at 150 and 250°C only two components are detected (III and II), due to water molecules with weak hydrogen bonding or "free" water. In samples calcined

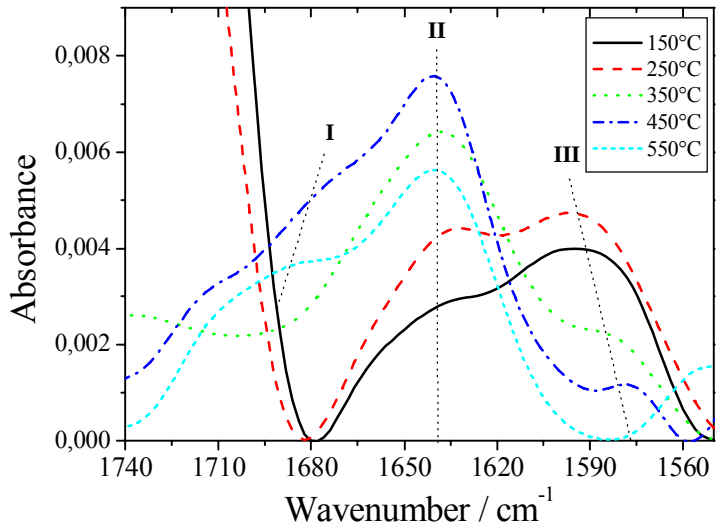

Figure 29: *FTIR absorption spectra in the range 1740 – 1550 cm^{-1}, where bending vibration modes of water in mesostructured silica films are detected: water molecules that aggregate with strong hydrogen bonding (I), water molecule clusters with moderate intensity of hydrogen bonding (II) and water molecules that interact with each other with weak hydrogen bonding (III).*

at larger temperatures, with the removal of the organic template, the II component is becoming predominant with the progressive disappearing of the free water. The I component is, instead, detected in samples after thermal treatments larger than 350°C.

These bands, which are in a region where no other absorptions are observed, have been used also to monitor qualitatively the changes of the absorbed water content in the samples by measuring the intensity changes as a function of the thermal treatment. We have deconvoluted the FTIR spectra, in the 1640 cm^{-1} region, by Gaussian fitting and we have used the sum of the absorption modes area of the three different water component to evaluate the water content variation in the films.

These values have been compared with the changes in intensity of the CH_2 stretching in Pluronic molecules (2940 cm^{-1}). Figure 30 shows the trends in the relative content of Pluronic F-127 and H_2O as a function of the calcination treatments. The absorption of water in the films increased when larger calcination temperatures were employed and the removal of Pluronic F-127 from the pores conversely increased. The water absorption showed a sharp increase after calcination of 450°C when great part of the block co-polymer was removed. Samples calcined at larger temperatures showed, instead, a decrease in water absorption.

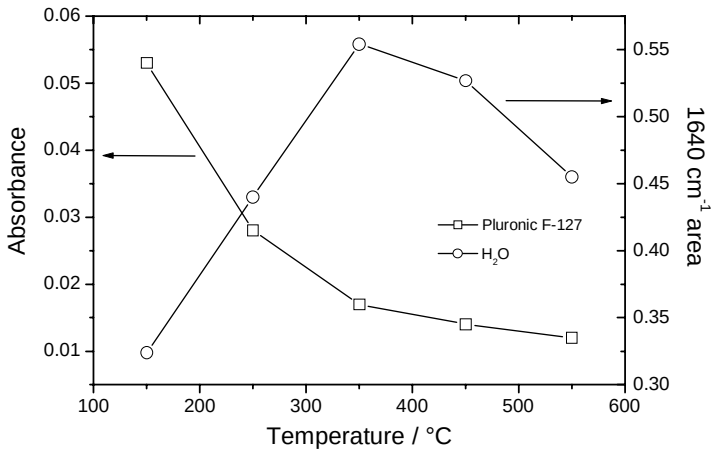

Figure 30: *Changes in the relative content of Pluronic F-127 and H_2O as a function of the calcination treatments. The changes in intensity of CH_2 stretching mode of Pluronic molecules (2940 cm^{-1}), left y axis, has been evaluated as a function of the calcination temperature. In the right y axis, deconvoluted areas of the water absorption components, in the 1640 cm^{-1} region, have been used to evaluate the water content variation in the films.*

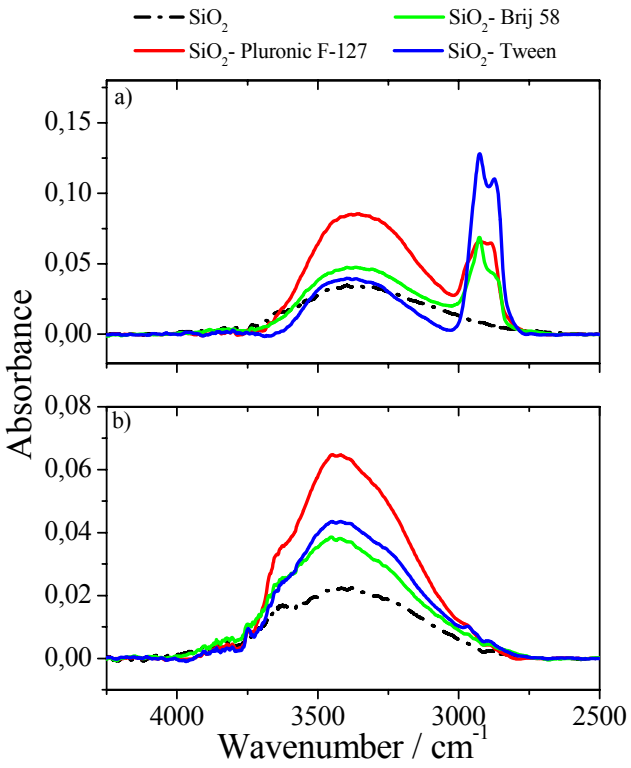

Figure 31 *FT-IR absorption spectra of mesostructured silica thin film deposited on a silicon substrate after 1 hour of thermal treatment at 150°C (a) and calcination at 350°C (b).*

Similar resuls can be obtained for sample synthesized using other surfactant (Figure 31a). After calcination at 250°C and 350°C for one hour (Figure 31b), the templating agents were removed (the copolymer bands disappeared) whilst the –OH concentration increased in intensity in comparison with the non-mesoporous silica film (broad band in the 3750-2800 cm^{-1} range[16]). Figure 32 shows the FTIR absorption spectra for a film synthesized with CTAB as templating agent: the surfactant (bands at 2950 and 2860 cm^{-1} [16]) was removed upon thermal calcination between 300 and 350°C. A maximum –OH concentration for 350°C that could be related to several factors (as not only the residual copolymer amount but also the presence of its decomposition products or the dependence of silica structural properties on the treatment temperatures) is observed.

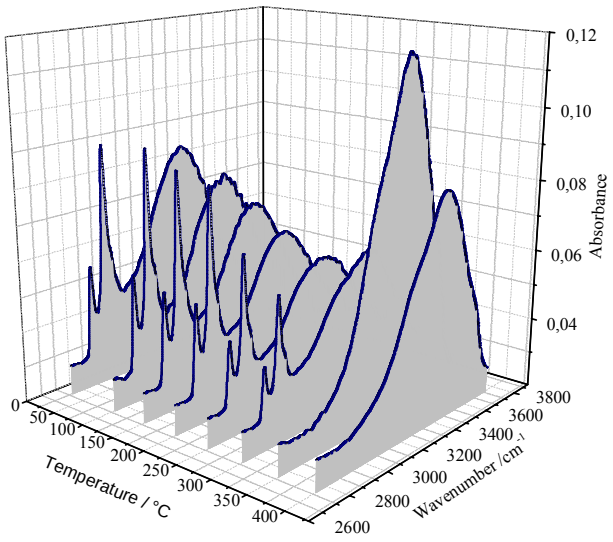

Figure 32 *FTIR absorption spectra of mesostructured silica thin film deposited on silicon substrate synthesized using CTAB as templating agent after progressive 1 hour thermal treatments.*

3.3 LA-XRD spectroscopy

To evaluate the degree of order related to porosity, Low Angle X-Ray Diffraction (LAXRD) was used.

LAXRD spectra showed that the silica mesoporous films have an ordered pore distribution,

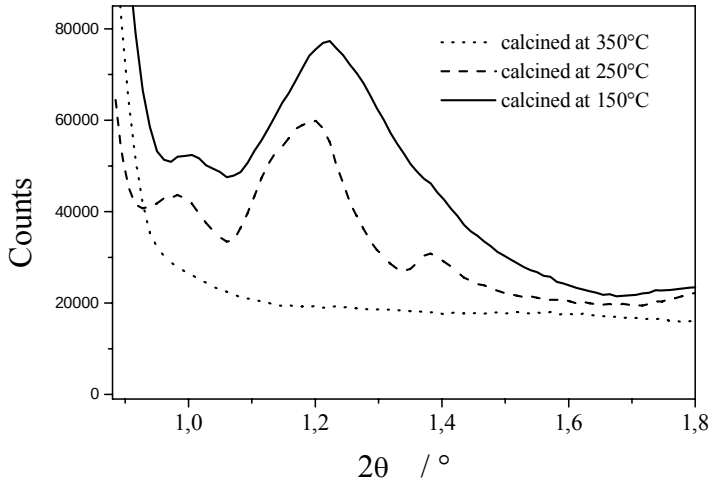

Figure 33 *Low angle XRD pattern of silica mesoporous films obtained using Pluronic-127 as templating agent (X-ray source: CuK_α).*

even if the degree of order and the interplanar distance clearly decreases with the thermal treatment of sample (Figure 33).

Moreover, we have certainly a normal shrinkage of the lattice symmetry (Figure 34): calcination modifies the structure from 2-D hexagonal to 2-D centred rectangular[17]. This mesoporous films evolution could be confirmed by Small-Angle X-Ray Scattering (SAXS) 2-D patterns.

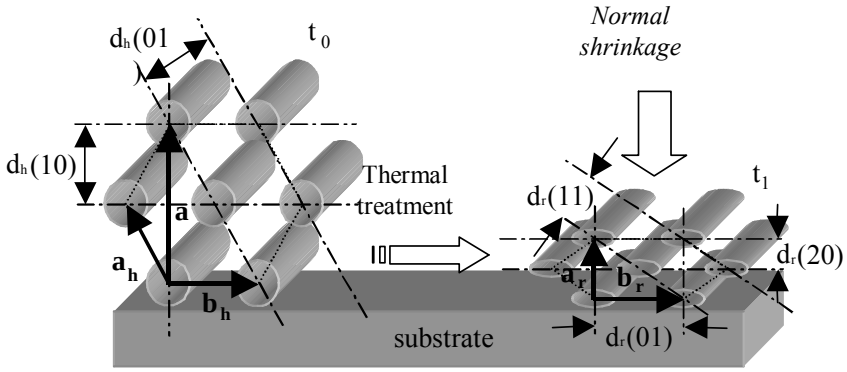

Figure 34 *Evolution of the hexagonal 2-D cell in a centred rectangular cell with thermal treatment*

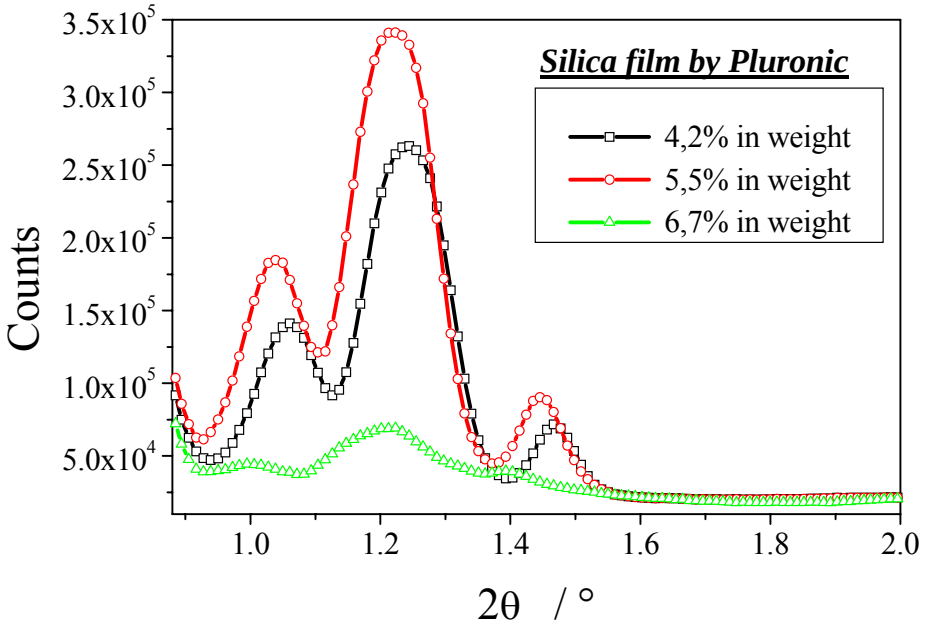

Figure 35 *Low angle XRD spectra obtained from samples synthesized using different Pluronic concentrations (X-ray source: CuK_α)*

LAXRD spectra revealed also that the order has a maximum value in function of the concentration of block-copolymer: this aspect is shown in Figure 35, as example, for samples synthesized by Pluronic-127. Therefore, an important parameter to control the preparation process of mesoporous films is the concentration of templating agents: this concentration should allow the aggregation of supramolecolar units exceeding the critical micelle concentration.

It is found that another important variable to control the obtaining of a good organisation of the mesoporous order is the withdrawal speed: at larger speed, in fact, the order decrease. The organisation is related to a dynamic process: the single molecules have to organize in supramolecolar ordered units during solvent evaporation. The nucleation process start from the interfaces of deposited thin film (substrate and solution/air) and move along the film during the extraction: in accordance to this model high extraction speed (that results in high withdrawal speed) do not allow a good organisation of the organic molecules and they can result frozen without forming an ordered structure.

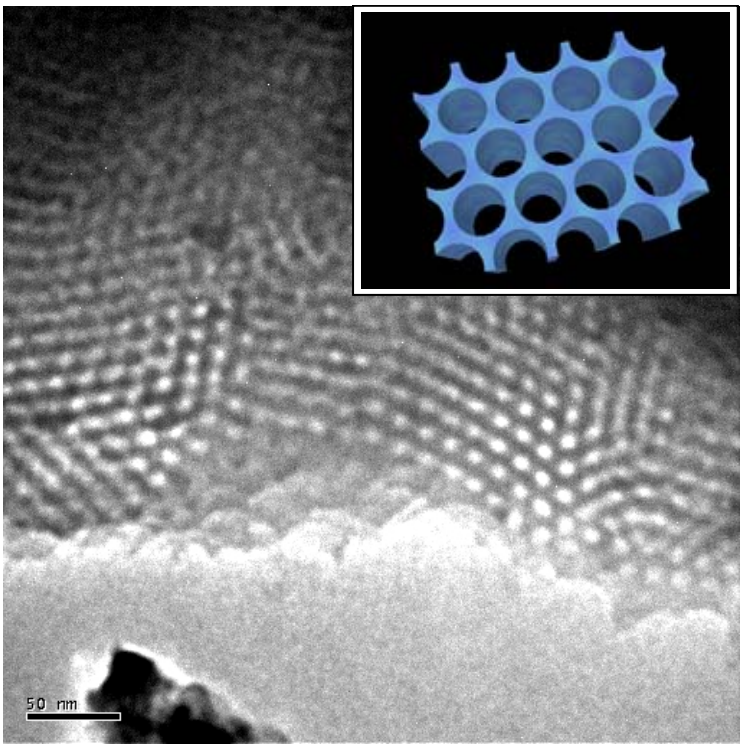

Figure 36 *TEM image of a mesostructured silica film synthesized using Pluronic F-127 as surfactant. The insert is a schematization of the meso-ordered structure.*

3.4 GI-SAXS analysis

Micrographs of the films and monoliths were obtained by a JEOL 100 CXII transmission electron microscope (TEM). In Figure 36 is reported the TEM image obtained for a silica mesostructured film, synthesized using Pluronic F127 as surfactant, before calcination treatment.

The mesophase geometry is 2-D hexagonal (P6m space group), as it is depicted on the upper corner of the Figure 36; the pores and silica walls have similar dimensions (from 6.5 to 7 nm). The thermal calcination removed the templating agent (tri-block copolymer micelles) from the channels from leaving an ordered porosity. The films showed to retain the mesostructured porous phase up to 950°C. The thermal treatment induced an increasing shrinkage in the direction normal to the substrate without, however, cracking in the films.

The ordering of the mesostructure in films deposited on silicon substrates was investigate using the Grazing Incidence Small Angle X-ray scattering (GI-SAXS) apparatus at the Austrian SAXS beamline (2 GeV electron storage ring) of ELETTRA Synchrotron (Trieste, Italy)[18]. The used wavelength was 1.54 Å and the sample to detector distance was set to 1.5 m. The substrate grazing angle was smaller than 3° and kept constant during the measurements. From the recording of the CCD detector we observed the "in plane" as the "out of plane" diffraction maxima, taking for each image the average of 10 single acquisitions and 3 seconds of exposition time.

The GI-SAXS images showed that the ordered mesophases after deposition and calcination or chemical extraction are maintained. In Figure 37, the pattern is referred to a mesophasic silica film containing Brij 58. At its right side, the corresponding P6m phase is schematized and the interplanar distances are highlighted. Using a reference sample (silver behenate), the pore distance, both along d(10) and d(01) directions, has been estimated to be 5.4 nm.

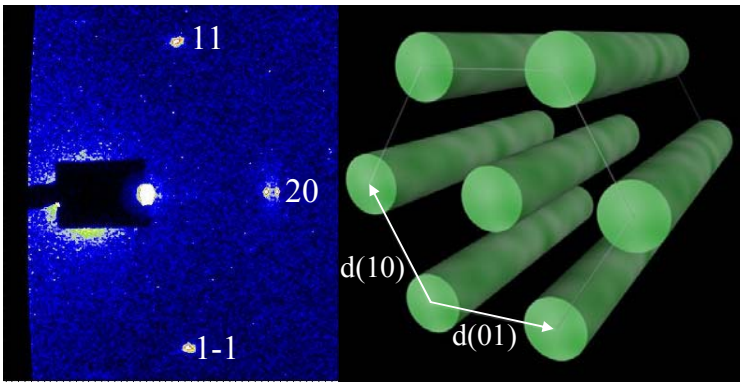

Figure 37 *GI-SAXS image (left side) and corresponding ordered structure (right side) of a mesostructured silica thin film (Brij-58).*

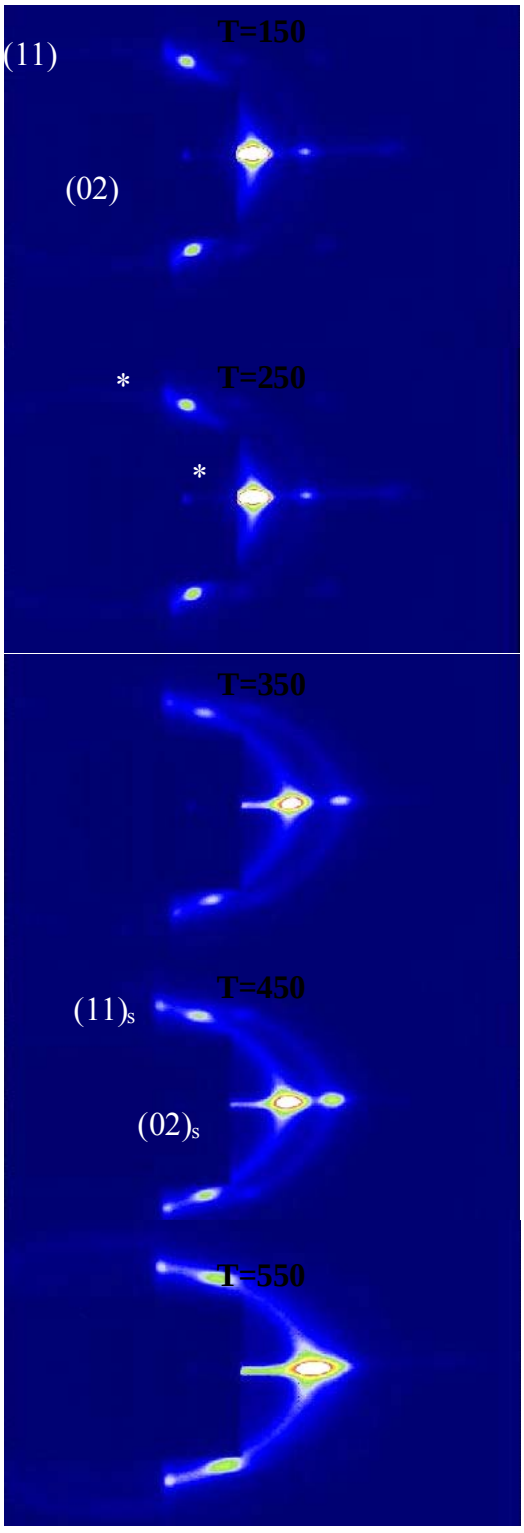

Figure 38 *SAXS images of the silica films taken at gracing incidence*

Figure 38 shows the GI-SAXS images obtained from the different samples (from 150 up to 550°C), well resolved reflections due to the organized mesophase are observed in every

diffraction pattern. The spots are indexed as (10) and (02) planes of a beginning 2D-hexagonal phase and at higher temperatures orthorombic c2m phase (space group) (Figure 33 – 150°C). In the images a double circle is also seen, this effect is particularly enhanced in the 350°C frame and is related with the presence of a second organized phase partly contracted, which is attributed to the top layer which is contracting faster during the calcination. The second order attributed to the spots (02) and (11) is evidenced with the asterisks in the 250°C image (it gives the reflections (04), (12)), the spot related to the (20) was also detectable from 250°C. In the samples calcined with different heat treatments the maximum attributed to the (02) plane diffraction moved from the beam centre, corresponding to a decreasing of lattice parameter from 154 Å to 114 Å.

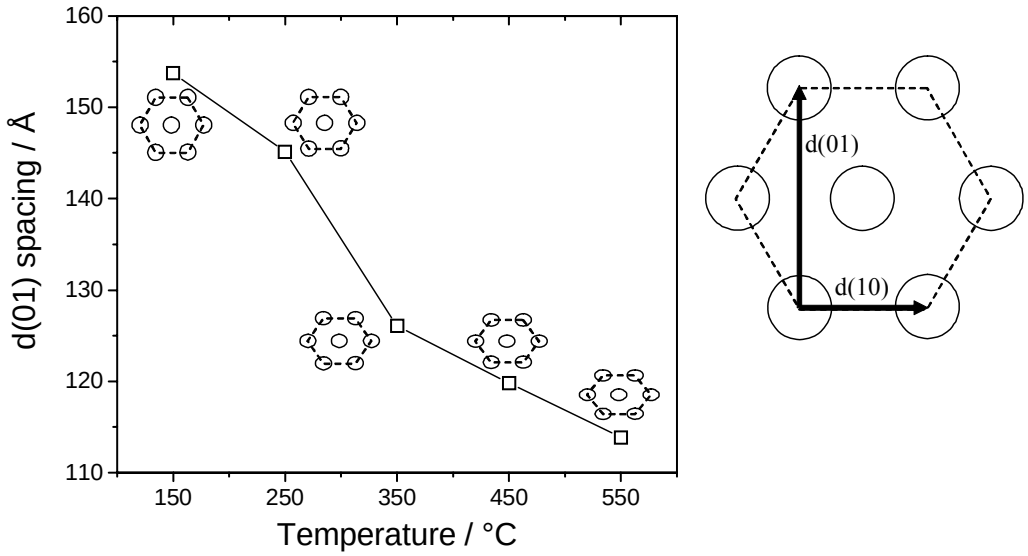

Figure 39 *Changes in the interplanar spacing, d(01), as a function of the calcination temperature. The cell has been indexed as 2D-hex (c2m).*

The change of the d(01) space in the different mesostructured films (c2m structure) is shown in Figure 39, a contraction in the 01 direction is observed at larger calcination temperatures. This contraction is in agreement with the measured thickness shrinkage in the films, from around 550 (150°C calcined samples) to 450 nm (550°C calcined samples).

Furthermore, to evaluate the porosity order, low angle X-ray diffraction (LAXRD) was used. Measurements confirmed that the mesostructure is maintained, even if with a

monodirectional contraction (normal to the substrate plane) that is induced, as previously observed, by the thermal treatments.

3.5 EDXD Analysis: Diffraction and Reflectivity spectra

X-Ray Diffraction experiment were carried out by using an EDXD apparatus elsewhere describe[19, 20]. The intensity distribution scattered by mesoporous material is function of the module of the momentum transfer q expressed as a function of the wavelength of the incident radiation λ and the scattering angle θ by relation: $q = (2\sin\theta)/\lambda$; in the EDXD experiment θ is fixed while λ varies.

The X- ray reflectometry is a technique sensitive to surface and interface morphology at the Ångstrom resolution and is commonly utilized to probe the properties of surfaces and interfaces of layered samples (films deposited on substrates, multilayers, superlattices, etc.) .

The method makes use of the optical properties of X-rays briefly outlined in the following and fully reported elsewhere[21].

In optics, referring to the film surface, the Snell law can be expressed as $n_1\cos\theta_1 = n_2\cos\theta_2$, ($\theta_1$ and n_1 being the incidence angle of the primary beam and the refractive index of the first medium and θ_2 and n_2 the reflection angle and the refractive index of the second medium). If the first medium is vacuum (or air), $n_1 = 1$ and the previous equation, at the critical angle θ_c, takes the form: $\cos\theta_c = n_2$, since when $\theta_1 = \theta_c$, $\theta_2 = 0$.

In the X-ray energy range, the refractive index can be expressed as:

$$n = 1 - \left(\frac{\lambda^2}{2\pi}\right)\rho r_0 Z^2 + i\left(\frac{\lambda}{4\pi}\right)\mu$$

(λ being the incident wavelength, ρ the material density, r_0 the classical electron radius, Z the atomic number and μ the linear absorption coefficient, tipically 10^{-6}-10^{-7} thus negligible).

Therefore, the total reflection conditions are fulfilled when $\cos(\theta_c) = 1 - (\lambda^2/2\pi)\rho r_0 Z^2$ that, at the second order approximation, can be summarized as $q_c = \theta_c/\lambda = \text{constant}$, where q_c is the critical scattering parameter (momentum transfer). The q range of interest, containing all the morphological information, is around this critical value.

Indeed, the position of the critical edge (q_c) and the slope of the reflectivity profile are determined by the material density and the surface roughness (variance from the average thickness), respectively. Furthermore, if the sample consists of a thin film deposited on a thick

substrate, the signal exhibits oscillations produced by the interference of the two waves reflected at the surface and interface: the frequency of the oscillations is roughly proportional to the film thickness, while their damping is related to the interface roughness.

To collect an X-ray reflection spectrum, that is the reflected intensity as a function of q, two ways can be used. In fact the q scan can be accomplished either by utilizing a monochromatic beam and an carrying out an angular scan (angular dispersive mode) or using a polychromatic X-ray beam at fixed angle and carrying out an energy scan [energy dispersive (ED) mode], no movement being required[22].

The advantages of the ED technique on the angular dispersive counterpart, mainly related to the immobility of the experimental setup, are particularly remarkable when reflectometry measurements are concerned[23, 24]. Indeed, in the ED mode, a single spectrum collected at fixed angle which covers a range of some 10^{-1} $Å^{-1}$, is made of a collection of several hundred points so that the q resolution approaches 10^{-4} $Å^{-1}$. Such q-resolution would be hardly achieved using a conventional laboratory angular dispersive reflectometer. Moreover, the stationarity of the experimental setup reduces the systematic errors induced by the angular scan (misalignments and aberrations) and guarantees the reproducibility of the experimental conditions (particularly critical at small angles) when many consecutive measurements have to be performed, as in the present case. This allows to perform in situ investigations with an extremely high level of confidence. On the other hand, the main drawback of the ED mode, i.e. the decrease in the q-resolution due to the uncertainties on both the angle and the energy,

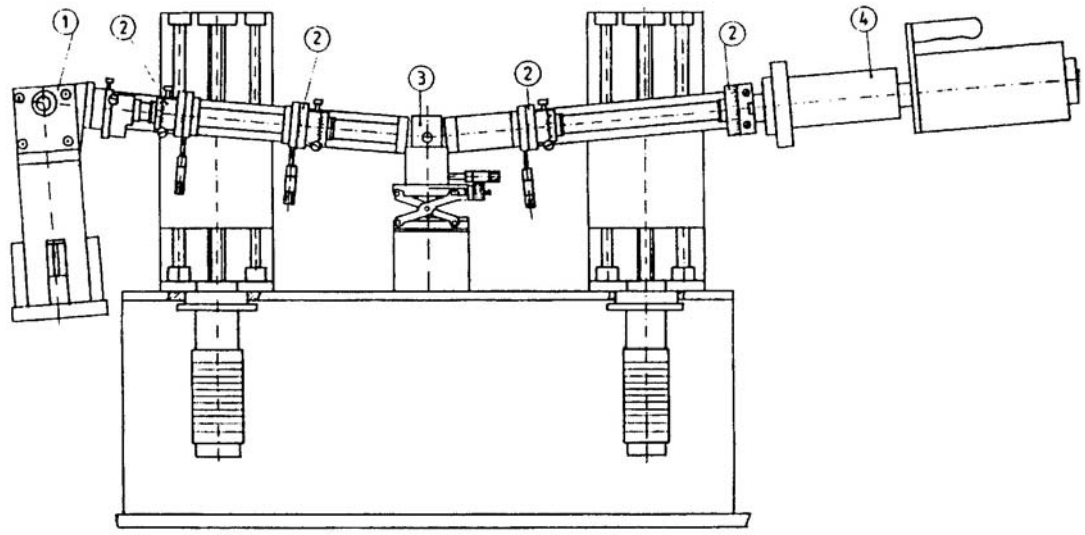

Figure 40 *Energy dispersive X-Rays reflectometer.*

does not affect a reflectivity measurement since the EDXR pattern of a thin film is characterized by long period oscillations.

The energy dispersive X-ray reflectometer used is a non commercial machine[25] (Figure 40). The instrument is provided with two benches, one carrying the x-ray tube, the other the energy sensitive detector, pivoting around a single central axis. The X-ray optical path is defined by four variable slits mounted on the arms. The arms are moved by two linear actuators driven by step motors and the tangent of the angle is read by two linear encoders. Both the minimum step movement and the resolution are of the encoders are 1 μm, that, in our case, guarantees a reproducible minimum angle increment of 0.004°. The white incident beam is produced by a standard 2kW tungsten anode X-ray tube and the detection is accomplished by an EG&G high purity germanium solid-state detector. The detector is connected to a PC via ADCAM hardware and the signal is processed by a Maestro software, which performs the necessary analogue to digital conversions. The energy resolution ΔE/E is ca. 1.5% in the energy range of interest (20-50 keV). Neither monochromator nor goniometer are required in the energy dispersive mode.

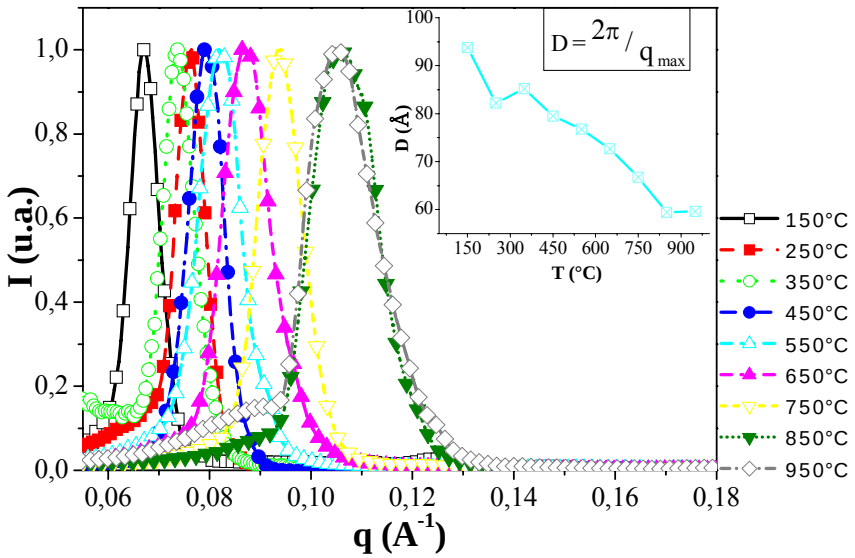

Figure 41 *The diffraction peaks in function of the q momentum and therefore of the interplanar space D are clearly visible in the EDXD spectra.*

All samples calcinated at various temperatures in the range 150°C - 1050°C were tested. In Figure 41 the EDXD spectra of the samples treated between 150°C-950°C show an increasing of transfer momentum q or a decreasing of interplanar space d=2π/q (insert Figure 41) with

increasing calcination temperature. The curve values in Figure 41 were normalised. This shift of the main diffraction peak suggests that the material structure suffers a shrinkage.

This shrinkage is homogeneous in each direction, in fact successive Bragg peaks position have the same behaviour in temperature function, in Figure 42, we reported the momentum transfer q($Å^{-1}$) as function of calcination temperature. We suppose that to increasing the temperature improve the copolymer removal and at the same time modify the silica properties, causing a close to pores. A correlation with a SAXS data, indicates that the cubic phase is most probably structure. The relative peak position are $\sqrt{4}$ and $\sqrt{8}$, the absence of other reflection peaks prevents to distinguish between a body-centre cubic phase or a face-centre cubic phase. The Miller index for three reflections are (100) (200) (220). The sample at T = 1050 °C have not showed any Bragg peak, because elevate temperature doesn't allow silica to evolve in a stable configuration, but the structure has a collapse destroying any ordered phase.

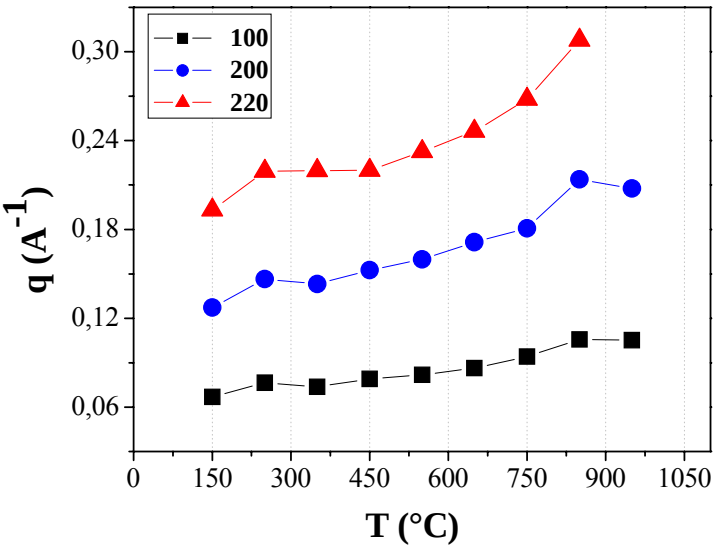

Figure 42 *Momentum transfer q($Å^{-1}$) from EDXD spectra as function of calcination temperature.*

A systematic reflectivity analysis was performed in order to achieve morphological and long range structural information upon samples of these materials, calcinated at various temperatures in the range 150°C - 1050°C.

All reflectivity patterns were collected in the same conditions, at grazing incidence (theta = 0.125°) and in a controlled atmosphere (N_2 flux, 180 nmol/sec). Superlattice Bragg peaks are

visible in the reflectivity spectra (Figure 43), witnessing an internal order of the thin films. Indeed, since the reflected signal is due to the optical contrast between the scattering materials, such peaks can be attributed to the presence of an ordered porous structure inside the films. In particular, the reflection pattern of the sample calcinated at 150°C differs from those of the others, because it exhibits an anomalous (convolved) double peak. This can be attributed to the presence in the bulk of two ordered materials with different scattering length densities, the surfactant still being present at such low calcinations temperatures. Indeed, as the temperature grows, only the signal coming from the mesoporous structure remains and the Bragg peaks get broader, indicating that the internal order is decreasing due to the thermal treatment. Finally, at 1050°C, no reflections are no longer visible indicating the lack of the mesoporous structure order.

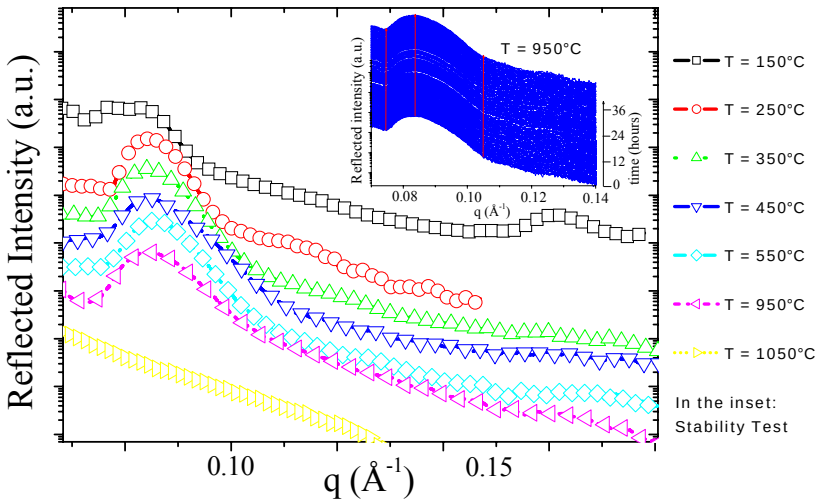

Figure 43 *X-Ray Reflectivity spectra are plotted as a function of the scattering parameter q, comparing the profiles upon different temperatures and a stability test upon the less ordered film is shown.*

Surface roughness were calculated by the Parrat model for reflectivity profiles. All the films exhibit a roughness value in the range 6-8 Å, except for the one calcinated at 1050°C, whose value is as high as 13Å. This is another evidence confirming the disorder characterizing such high calcination temperature, not only in the bulk, but even on the surface.

The sample calcinated at 950°C is the last one to show a kind of internal structure, even though the reflection is now very weak and the Bragg peak is extremely broad. This sample, being the last that retains a certain degree of order, is the most critical and on it the following

stability test was performed. The sample was submitted to alternate conditions, i.e. in the controlled atmosphere described above, then at room conditions (temperature, pressure and relative humidity), and finally under the controlled atmosphere, again. The residence time in such conditions was 12 hours each. During the overall 36 h (insert Figure 43), the sample was irradiated by an X-ray beam at grazing incidence and a sequence of 15 minutes long X-ray reflectivity spectra was collected. Passing from the N_2 gas flux to room conditions (and back), no variation was observed either in the peak position, in its shape or in the slope of the underlying reflectivity profile. This is an evidence of no morphological and structural modifications occur, namely that the film is stable even when left in air.

References of Chapter 3

1. M.Klotz, P.A.Albouy, A.Ayral, C.Menager, D.Grosso, A. Van der Lee, V.Cabuil, F.Babonneau, C.Guizard, *Chem.Mater.* **2000**, *12*, 1721
2. Grosso, D.; Balkenende, A.R.; Albouy, P.A.; A. Ayral, H.Amenitsch,; Babonneau, F. *Chem.Mater.* **2001**, *13*, 1848.
3. Ogawa, M. Supramol. Sci., **1998**, *5*, 247.
4. Zhao, D.; Yang, P.D.; Melosh, N.; Feng, Y.L.; Chmelka, B.F.; Stucky, G. *Adv.Mater.* **1998**, *10*, 1380.
5. Grosso, D.; Soler-Illia, G.J.A.A.; Babonneau, F.; Sanchez, C.; Albouy, P.A., Brunet-Bruneau, A.; Balkenende, A.R. *Adv.Mater.* **2001**, *13*, 1085.
6. Crepaldi, E. L.; Grosso, D.; Soler-Illia, G. J. A. A.; Albouy, P.-A.; Amenitsch, H.; Sanchez, C. *Chem. Mater.* **2002**, *14,* 3316.
7. Soler-Illia, G.J.A.A.; Crepaldi, E.L.; Grosso, D.; Durand, D.; Sanchez, C. *Chem.Comm*. **2002**, 2298.
8. P. Innocenzi, P. Falcaro, D. Grosso and F. Babonneau, J. Phys. Chem B **2003**, 107, 4711
9. Chen, J.; Li, Q.; Xu, R.; Xiao, F. *Angew.Chem.* **1995**, 34, 2694 **1995**,
10. Plotnichenko, V.G.; Sokolov, V.O.; Dianov, E.M. *J.Non-Cryst.Solids* **2000**, 261, 186
11. Davis, K.M.; Tomozawa, M. *J.Non-Cryst.Solids* **1996**, 201, 177
12. Innocenzi, P. *J.Non-Cryst.Solids*, **2003**, 316, 309
13. Zhao, X. S.; Lu, G. Q.; Whittaker, A. K.; Millar, G. J.; Zhu, H. Y. *J. Phys. Chem. B* **1997**, 101*,* 6525
14. Broodsky, P.A.; Fawcett, W.R. *J.Phys.Chem. A* **2000**, 104*,* 8307
15. Shen, Y.; Wu, P. *J.Phys.Chem. B* **2003**, 107, 4224
16. P. Innocenzi, J. of Non-Cryst. Solids **2003**, 316, 309
17. D. Grosso, G. J. Soler-Illia, F. Babonneau, C. Sanchez, P. A. Albouy, A. Brunet-Bruneau, A. R. Balkenende *Adv. Mat*. **2001**, *13*, 1085-1090
18 Amenitsch,H. ; Bernstorff, S.; Kriechbaum, M. ; Lombardo, D. ; Mio, H. ; Rappolt, M. ; Laggner, P. *J.Appl. Cryst.* 30, 872 (**1997**)
19. Roser S. J.; Felici R.; Eaglesham A.; *Langmuir* **1994**, 10, 3853.

20. R. Caminiti and V. Rossi Albertini, International Review in Physical Chemistry **18** (2), 263(1999).
21. X.L. Zhou, S.H. Chen, Theoretical Foundation of X-ray and Neutron Reflectometry, Physics Reports **257,** 223-348 (1995).
22. A. Generosi, V. Rossi Albertini, G. Rossi, G. Pennesi, R. Caminiti, The Jour. of Phys. Chem. B., **107**, (2) 575-579 (2003).
23. K. Orita, T. Moritura, T. Horiuchi, K. Matsushige, Synthetic Metals **91,** 155-158 (1997).
24. V. Rossi Albertini, A. Generosi, B. Paci, P. Perfetti, G. Rossi, A. Capobianchi and R. Caminiti, *Applied Physics Letters* **82**, 22, 3868 (2003).
25. Caminiti R.; Sadun C.; Rossi Albertini V.; Colloco F.; Patent No. 01261484, Italy, 1993.

Chapter 4

Sensors based on Mesoporous Silica Thin Film and studies on their electrical responses

Introduction

The number of articles appeared on films is comparatively lower, even if organized films with pores in the order of 2-50 nm have an enormous range of potential applications to be exploited. Some few examples are optical[1] and electrochemical sensors[2, 3, 4, 5], films with low refractive index and films with ultra-low dielectric constant[6].

An important property of mesoporous films for their practical sensing applications is the accessibility from the external environment of the mesophase, which has a large interfacial area. In fact, at the surface of mesoporous film water molecules are adsorbed from the air arranging themselves in an ordered configuration which promotes the protonic conduction that is outlined by the "Grotthus model".

The interesting feature is that mesoporous silica films, where silica materials generally show very low electrical response to changes of humidity in the external environment, have exhibited high humidity sensing performances. The pores of mesoporous silica films, that have been obtained by non-ionic block copolymer self-assembly processes, are covered of silanol species that are acting as the anchoring sites to form "ice-like" organized layers of water where protonic conduction is easily realised. We have explored the performances of mesoporous silica thin films as humidity sensing membrane and we focus the attention on the conduction mechanism in mesoporous silica.

In this chapter we will describe the substrate processing and the sensor devices production. We will study the sensors response both to relative humidity than alcohols vapours changes using our designedly testing apparatus. We will at last study electrical properties and conduction phenomena in the sensing membrane trough Electrochemical Impedance Spectroscopy (EIS) measurements.

4.1 Substrate processing for mesoporous silica thin film based sensor devices

The devices used for this work were obtained by using both alumina substrates and silicon substrates with a passivated layer of thermal silicon dioxide with metallic interdigitated electrodes (Figure 44).

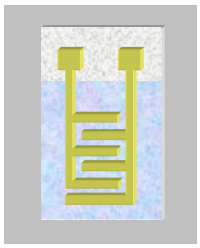

Figure 44 *Substrates with metallic interdigitated electrodes.*

In the first case (Figure 45a, Table 2) eight pairs of gold fingers 280 μm wide and 120 μm spaced with a length of 4500 μm were deposited through a metallic mask (screen printing).

In the second case, using AutoCAD 14, different masks were designed and realized by laser photolithography. The masks allowed reproducing the same geometries on any substrate by optical lithography using a mask-aligner. Forty pairs of electrode fingers (Figure 45b, Table 2) with a width of 20 μm and length of 5640 μm were geometrically defined on a

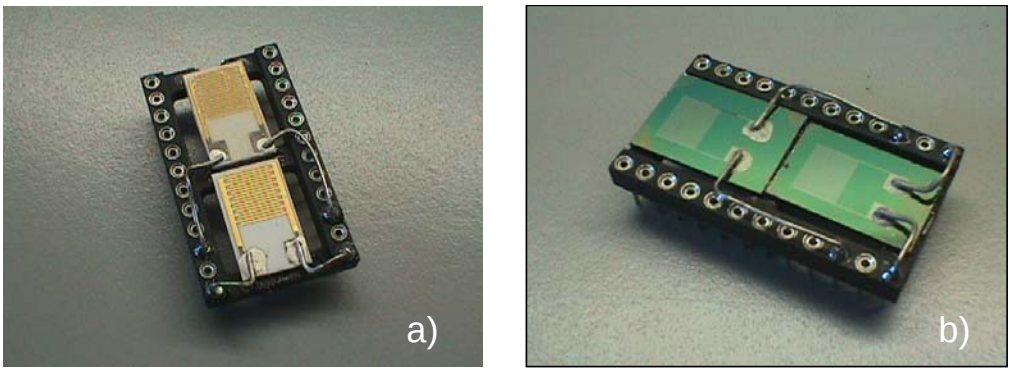

Figure 45 *Alumina substrates with gold interdigitated electrodes (a) and silicon substrates with chromium interdigitaed electrodes*

chromium film, 200 nm thick, previously thermally evaporated. The gap between the fingers was 20 µm. The batches of wafers obtained were then cut with a dicing system saw to separate each interdigitated electrode.

The mesoporous silica films were deposited on these substrates by dip-coating obtaining different thicknesses changing the withdrawal speed and calcination temperature.

	Cr-electrodes	*Au-electrodes*
Finger wide	*20 µm*	*280 µm*
Finger length	*5640 µm*	*4500 µm*
Space between fingers	*20 µm*	*120 µm*
Pair of fingers	40 + 39	9 + 8

Table 2 *Electrodes geometrical properties on used substrates*

4.2 Experimental Setup for Electrical Sensing Response measurements

The electrical response to humidity changes was analyzed by d.c. measurements in dark condition in a suitable cell where both temperature and humidity were monitored (Figure 46).

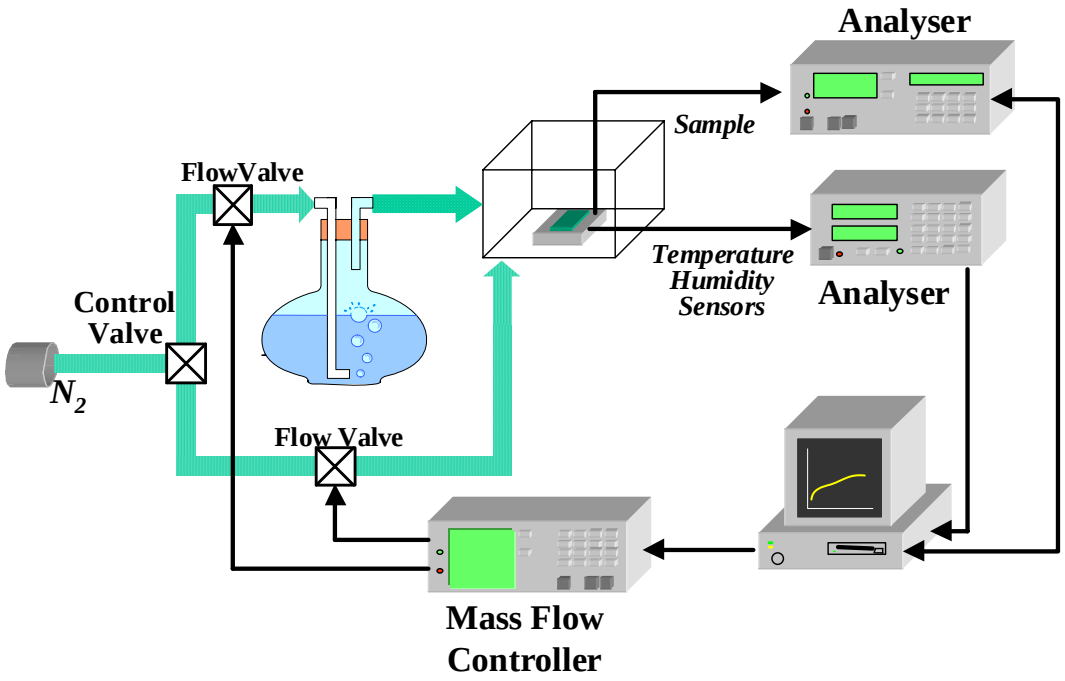

Figure 46 *Experimental set up for electrical sensing response measurements.*

Relative humidity (RH) was measured using a commercial sensor (Honeywell HIH 3602 C), which gave an accuracy of ±1%. The current response due to RH variations (from 5 to 95% with step of 2.5% every 100 seconds) was measured by a Keithley Quasistatic CV meter and recorded. A MKS mass-flow controller was used for nitrogen fluxes regulation to obtain both a dry and water (or alcohol vapours) loaded stream: changing the mix of these two streams, which is introduced in the "test chamber" (Figure 47), the relative humidity or the alcohol concentration was controlled.

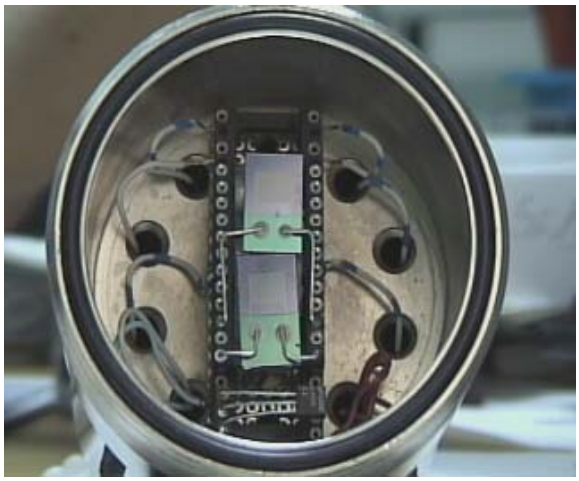

Figure 47 *Measurement chamber.*

4.3 Electrical Response of Mesoporous Silica Thin films on Alumina substrate to Relative Humidity

4.3.1 Dependence on templating agent

Measurements performed on alumina substrates have shown large current variations (upon four order of magnitude) related to exposure in a humid environment and are reported in Figure 48: if we compare the dependence from the RH% value of the steady state current response with that of the silica sol-gel film (not mesoporous), we can observe a more sensitivity for low humidity concentrations that is attributed to the large amount of porosity and surface area in the mesostructured films. In fact, the porosity improves the highly active surface (covered of silanol species) that can absorb water molecule. Therefore, the current intensity related to the protonic conduction increase whereas the reference silica sample exhibit only a weak response modification upon changes of the humidity environment (for low RH% values).

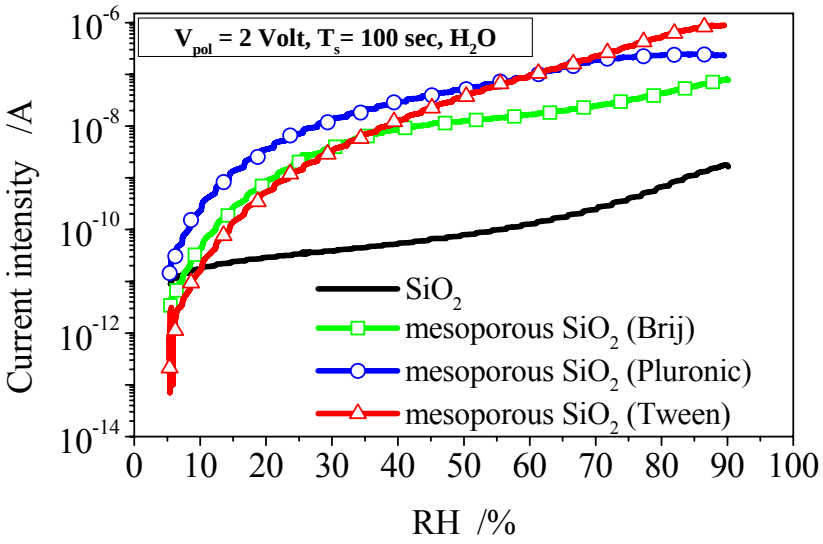

Figure 48 Above: *Electrical response vs. RH variation as a function of the different block copolymers used for the synthesis of mesoporous silica films (Operating temperature: 24.7°C).* **Below:** *ON/OFF cycles to test the stability of the device response*

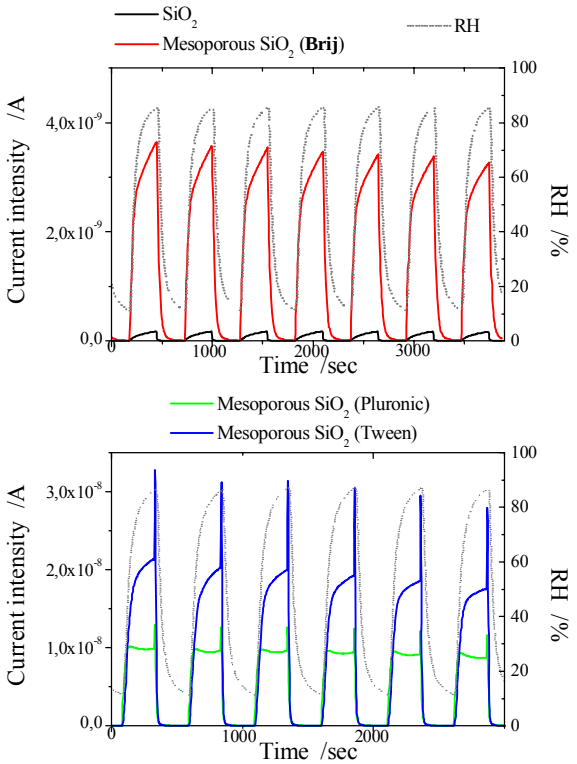

Samples prepared using different block copolymers as templating agent show some differences in the response, which are probably related to their microstructural differences.

However they difficult to correlate because of many parameters that can affect the performances of the materials: pore dimension, overall porosity, pore accessibility, amount of silanol species on the pore surface, presence of micropores in the silica walls. The response curve of all the samples shows a very sensitive region for high values of humidity concentration.

On/off cycles in dry and wet atmospheres have been performed to test the stability as a function of the operating time (Figure 48). The devices show a response without significant memory effects increasing the number of working cycles. Moreover, variation of electrical response appears fast with the change in RH value in the chamber atmosphere. The sensor performance has been found to also be dependent on the kind of substrate: mesoporous silica thin films on silicon substrates have shown a worst response curve with respect to that obtained on the alumina ones (as we will see in *paragraph 4.4*). We must point out that alumina substrates are not optically polished, and thus they have a rugosity (that can be estimated to be on the order of 1 μm) that can affect the sensor response.

4.3.2 Dependence on calcination temperature

Figure 49 shows the steady state current response of the mesoporous silica films as a function of RH changes in the measurement chamber, different curves due to samples calcined

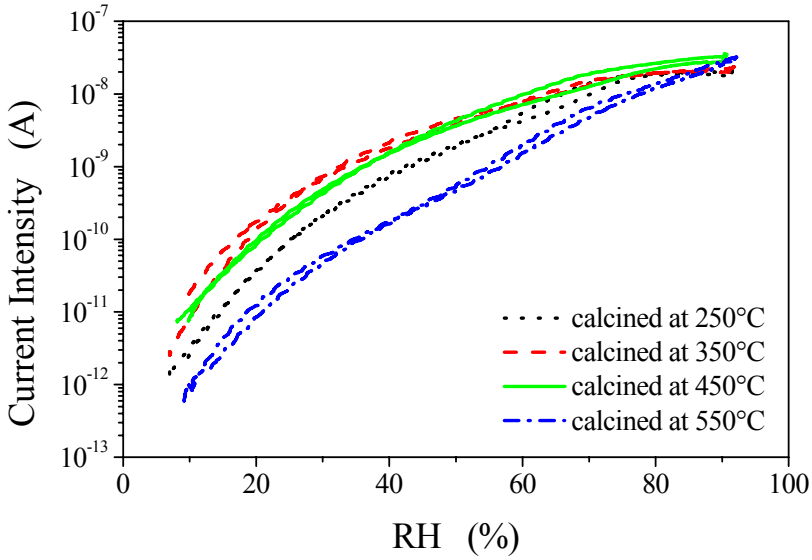

Figure 49 *Steady state current response of the mesoporous silica films on alumina substrate as a function of RH changes in the measurement chamber: effect of calcination temperature.*

at 250, 350, 450 and 550°C are shown. Each curve was recorded in a cycle of increasing and decreasing RH to evaluate the electrical response changes and the memory effects in the material.

Two almost overlapped curves were observed in all the samples, indicating a very little hysteresis loop. The current intensity change was up to 5 orders of magnitude, in films calcined at 550°C, for instance, the current increased from $5 \cdot 10^{-12}$ A (9% RH) up to $8 \cdot 10^{-7}$ A (92% RH).

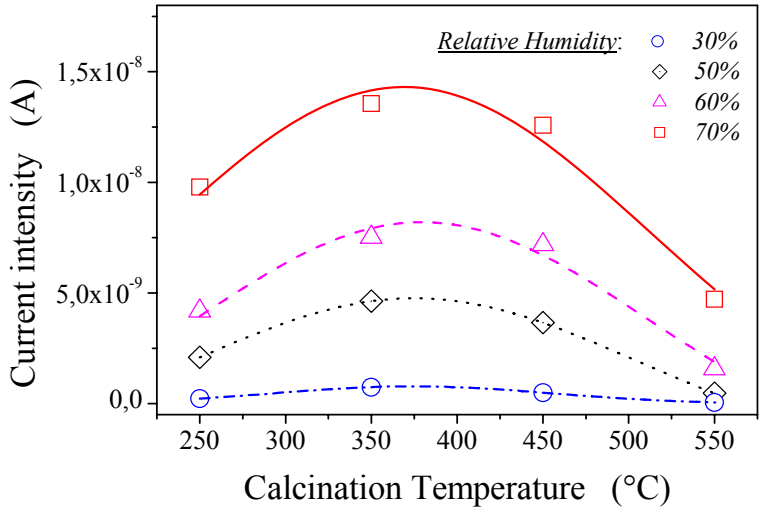

Figure 51 *The relationship between the current intensity and the calcination temperature as a function of relative humidity. The curves were fitted by a Gaussian function.*

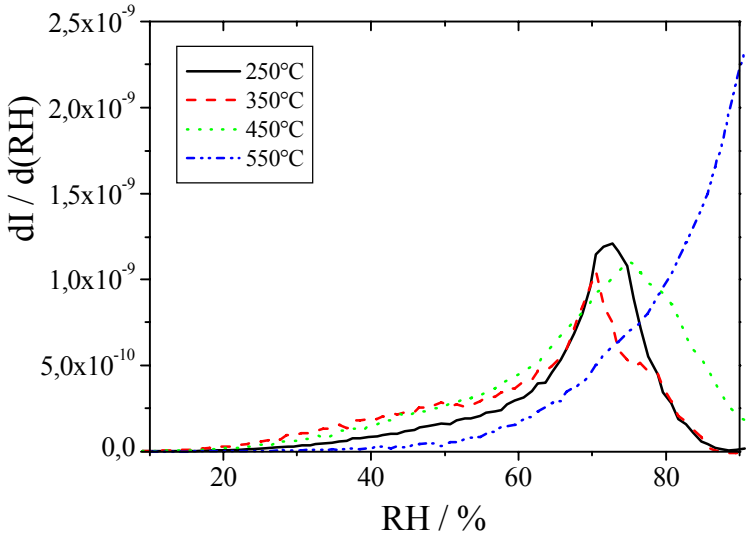

Figure 50 *Sensitivity curves have been obtained from the electrical characterizations versus the relative humidity content.*

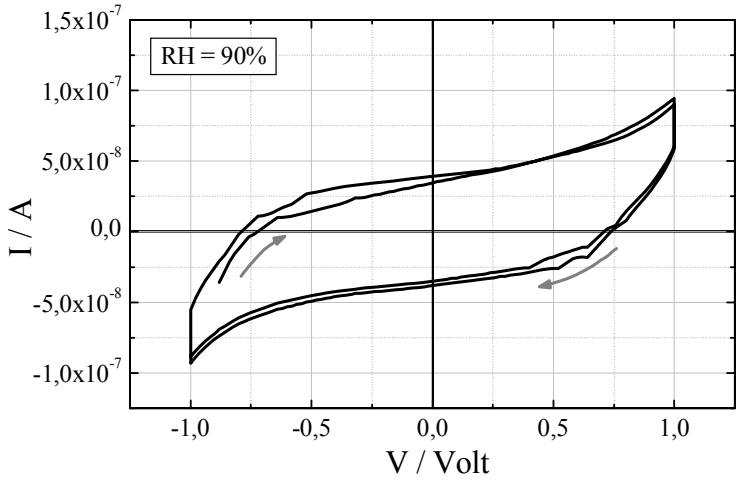

Figure 52 *Cyclic amperometric characteristics, performed at fixed 90% RH.*

The relationship between the current intensity and the calcination temperature as a function of relative humidity is shown in Figure 50. The curves were fitted by a Gaussian function. The larger absolute current value were observed for samples thermally treated at 350 and 450°C. The films annealed at 550°C showed the lowest current intensity response, which indicates a lower performance of the sensing device, at least in the considered range (30-70% RH).

The curves of sensitivity[7] (first derivative of the current intensity vs. RH) are shown in Figure 51. The sensors exhibited an enhanced sensitivity with the increase of the RH, with a steady peaking around 70% RH. After this RH value the sensitivity quickly decreased and at RH larger than 85% the curves showed the tendency to saturate. The 550°C calcined samples showed, however, a quite different behaviour, with a low sensitivity up to around 50% of RH and a constant increase in sensitivity at larger RH.

I/V characteristics (Cyclic amperometric characteristics) were performed at different relative humidity environmental conditions from –1 to 1 Volts. They showed a good stability with the time (Figure 52 at fixed 90% RH) and a large current hysteresis was observed during the cycle.

To correlate the structural properties with the current response to humidity changes of the films it is important to discuss all the features related with thermal calcination of the mesostructured materials: removal of the template, thermal dehydroxylation with reduction in length of the hydrogen bonded hydroxyl chains, formation of isolated and terminal species of silanols, decrease of porosity and pore diameter. As observed in Figure 2, the block copolymer used as organic template is progressively removed at increasing temperatures of calcination.

With the removal of the copolymer, the content in water within the mesoporous film increases (Figure 30), but the capability to absorb water is reduced with calcination higher than 350°C. The calcinations and the progressive removal of the template are also affecting the type of water molecules that are present within the pores. When the template is still partially occupying the mesoporous structure is hindering the formation of water aggregates with strong hydrogen bonding and mainly the absorbed water is in the form of little clusters and free molecules (Figure 29). It is interesting to note that the material showed a high electrical response to the changes in humidity, even if the template is not completely removed. It must also be underlined the relationship existing between the electrical response of the device and the presence of type II and III of water molecules. When the template is almost totally removed (550°C calcined samples) a quite different electrical response is measured (Figure 40), with respect to the samples where the pores are still partially occupied by the block co-polymer. This is likely due to partially hindering of water absorption by the residual template. From Figure 4 we can observe, in fact, that at 250°C around 50% of the template, with respect to the samples calcined at 150°C, is removed and more than 75% at 350°C, with the water absorption exactly following a reversed trend.

In the Grotthus model hydronium ions move from one H_2O molecule to the next one, via hydrogen bonding, in a complex "tunnelling" process of charge transfer and structural reorientations. The ionic migration must be associated with the presence of hydrogen bonded clusters; stronger and more extended clusters favour the migration. Stronger hydrogen bonding causes the O···O distance to be shorter, easing the protonic transfer. Even if recent experimental evidence is questioning the full validity of the Grotthus model[8], this model is still largely used to explain ionic mobility.

If we apply the classical Grotthus model to explain the current response of the material, the mechanism that generates the current in the device is assumed to be the movement of protonated water ions in "ice-like" layers formed on the pore surface. Surface hydroxyls groups are the sites where physical adsorption of water is realized, when the surface is completely hydroxylated, water will cover all the available OH sites forming a hydrogen bonded multilayer. The previous observations point out that there is a combinatory effect due to the presence of water molecules that are more or less strongly hydrogen bonded and the presence of silanol species that are acting as anchoring sites for the formation of "ice like" water layers. If we suppose that the formation of the "ordered" layers of water on the pore surface is correlated with type I and II of water, we can deduce that they will be really present

only in samples after calcinations at 350°C. A good electrical response should be therefore correlated, in this view, to the formation of the "ice like" layers and the presence of water molecules with higher hydrogen bonding. This is actually an optimum condition observed in the samples upon calcinations at 350 and 450°C (Figure 50). At 550°C the "free" water is no more detected and the electrical response of the system is different (Figure 49). We can note indeed that the template presence can enhance the current intensity at low RH value but, on the other hand, it leads to promote a saturation phenomenon and then to reduce the device sensitivity at higher RH value (Figure 51). Otherwise, the device calcined at 550°C, even if its current intensity and selectivity are lower up to 70 – 80% RH, it shows a better performance at higher humidity values. It is important to note that silica sol-gel films, as observed in previous works, show only a very low current variation to relative humidity[9].

The samples showed, in general, a quite good reproducibility. The variability in sensing performances in different set of samples, was within 5%, which should be also evaluated taking into account that the larger variability is introduced during the deposition of the films, realized in controlled laboratory conditions but not in a fully controlled environment, such as a clean room.

4.3.3 Sequential thermal treatments

After testing a sensor device with a sensing membrane treated at 350°C, we have

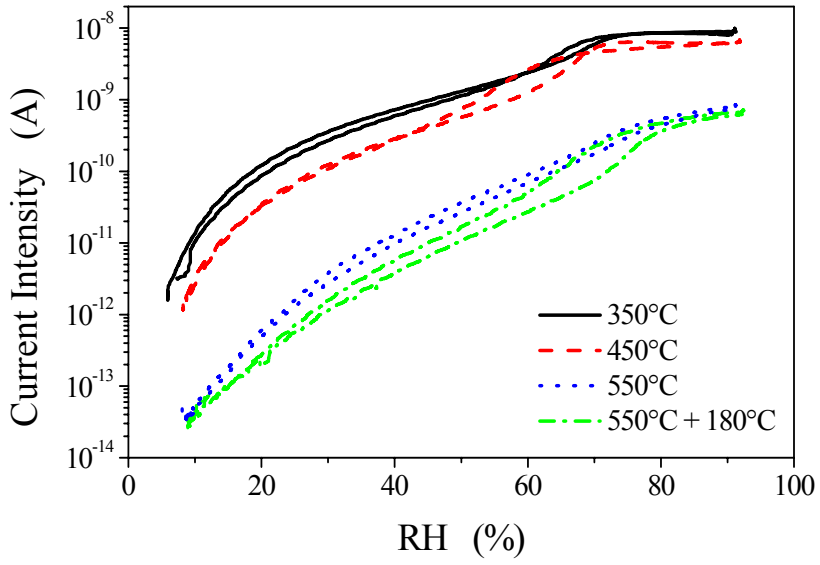

Figure 53 *Steady state current response of the mesoporous silica films on alumina substrates as a function of RH changes in the measurement chamber: effect of sequential thermal treatments.*

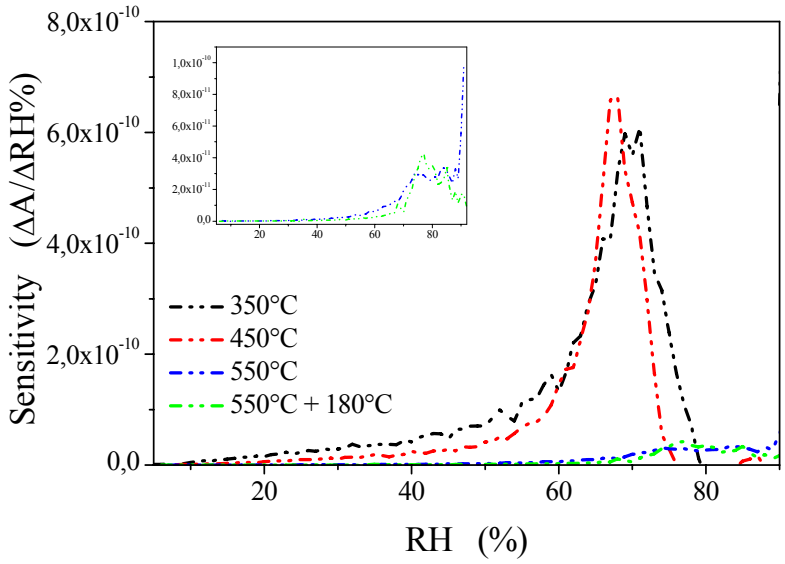

Figure 54 *Sensitivity curves have been obtained from the electrical characterizations versus the relative humidity content: effect of sequential thermal treatments.*

performed calcination at higher temperature in succession (450 and 550°C for 20 minutes) to evaluate how response of same sensor device accordingly is changed (Figure 53).

Current intensity clearly decreases increasing temperature. This result accord to measures previously showed (Figure 50): prolonged calcination and higher temperatures than 350°C probably allow a better surfactant removal but also a reduced ability to absorb water molecules by pores surface. The importance of calcination length is confirmed by further current decrease observed in the same sample after a final thermal treatment at 180°C, noticeably lower than previous calcination temperature.

According to results obtained in previous section, sensor device sensitivity (Figure 54) shows a maximum value for relative humidity nearly 70% after calcination at 350 and 450°C, but this value is an order lower than observed one for previous measurements (Figure 51). Sensitivity maximum clearly decreases after calcination at 550°C and it show a small shift to higher relative humidity value (around to 75-80%).

This can be explained by a decreasing of active group on surface (than can interact with water molecules) that involves lower current intensity and sensitivity but also with a contemporary later saturation phenomenon that involve a more difficult absorption.

I/V characteristics performed at different relative humidity environmental conditions from –1 to 1 Volts showed a good stability with the time (Figure 55, at fixed 50% RH) and a large

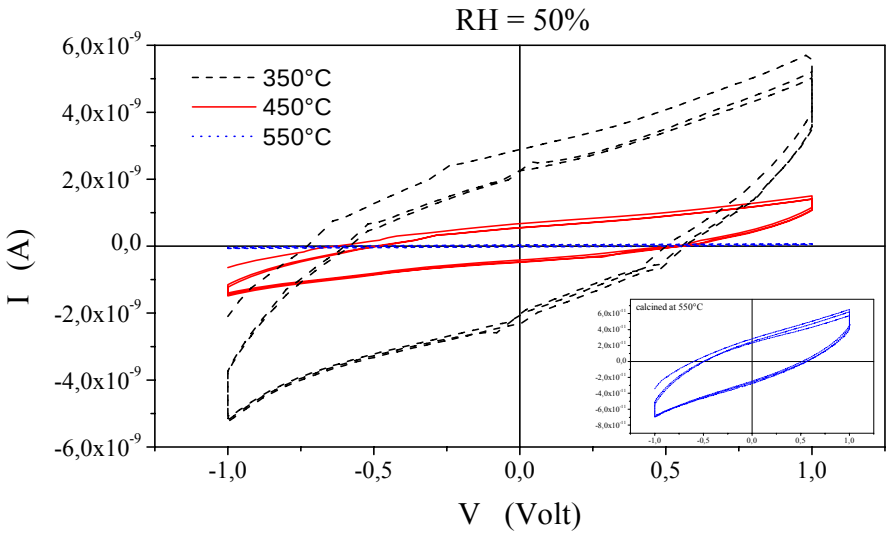

Figure 55 *Cyclic amperometric characteristics, performed at fixed 50% RH: effect of sequential thermal treatments.*

current hysteresis was observed during the cycle. Even if current intensity clearly decrease, characteristic hysteresis are similar after all calcination temperatures.

4.4 Electrical Response of Mesoporous Silica Thin films on Silicon substrate to Relative Humidity

Measurements performed for mesoporous silica thin film on silicon substrates, if

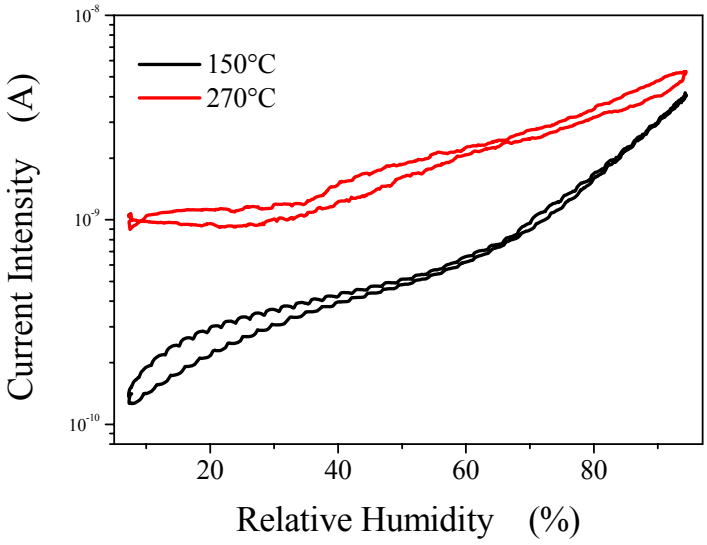

Figure 56 *Steady state current response of the mesoporous silica films on silicon substrate as a function of RH changes in the measurement chamber: effect of calcination temperature.*

compared to results obtained with alumina substrates, have shown smaller current variations (upon only one order of magnitude) related to exposure in a humid environment and are reported in Figure 56.

Calcination seems to have different effects on humidity response of sensor devices respect that seen above. Bigger and better (for sensing applications) current change has been observed with sample calcined at 150°C, while higher current intensity has been recorded for the 270°C treated one. These sensors have not shown wide hysteresis effects.

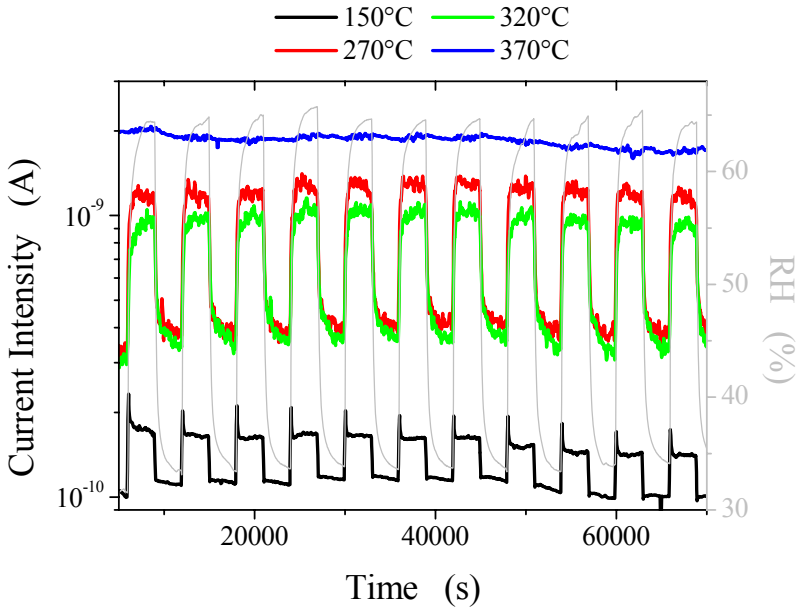

Figure 57 *ON/OFF cycles to test the stability of the device response*

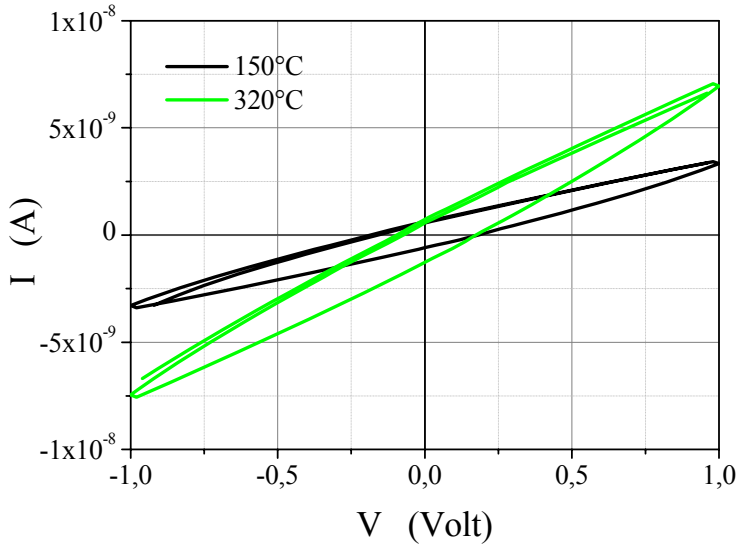

Figure 58 *Cyclic amperometric characteristics, performed in dry conditions.*

No memory effects and very fast response to humidity have been observed in long time dry-wet cycles testing (Figure 57). Better results have been obtained with sensing membrane calcined at 270°C or 320°C. No changes of current intensity in relation of relative humidity variations have been recorded for 370°C-treated sample.

I/V characteristics performed at different relative humidity environmental conditions from –1 to 1 Volts showed a good stability with the time (in Figure 58, at fixed 50% RH) and current hysteresis was observed during the cycle, even if smaller than previous alumina samples ones (Figure 55). Even if current intensity clearly decrease, characteristic hysteresis are similar after all calcination temperatures.

4.5 Electrical Response of Mesoporous Silica Thin films to Alcohol Vapours

Sensor devices have also been tested on alcohol vapours introduced into the measurement chamber. This kind of measurements has been suggested by the presence in alcohols

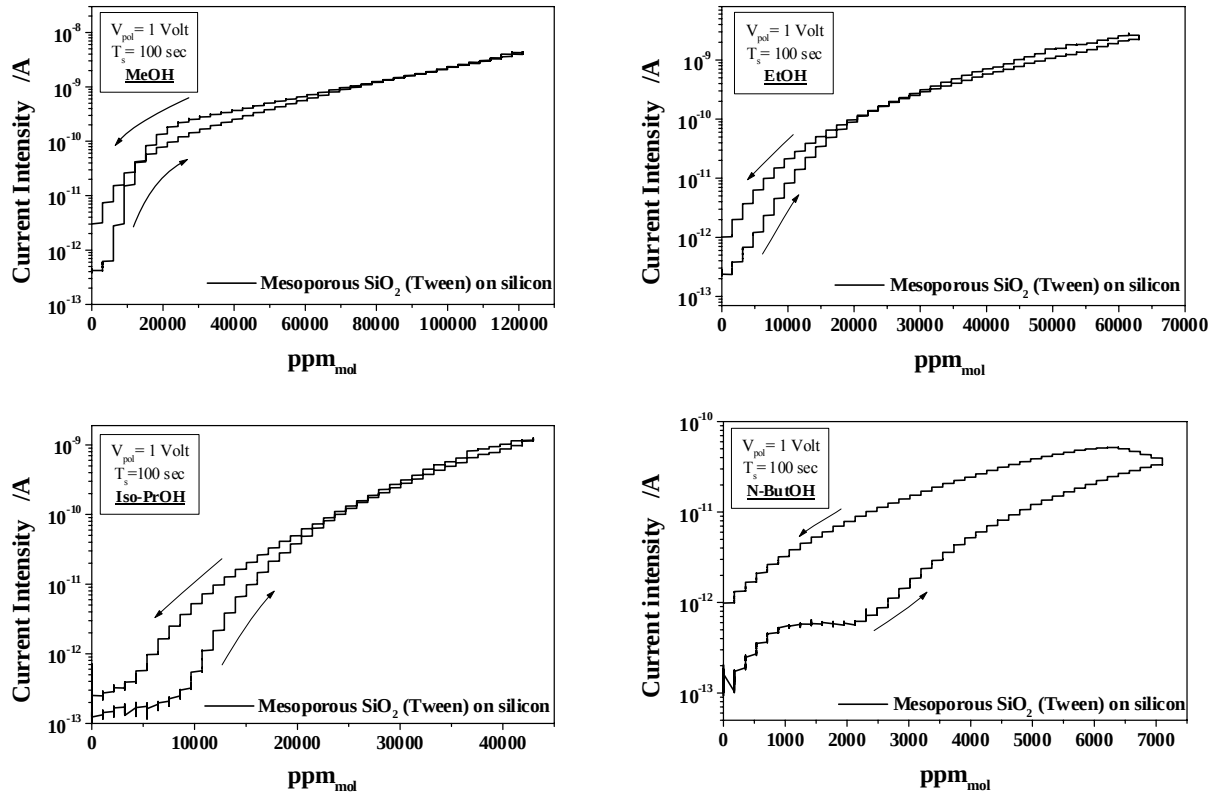

Figure 59 *Hysteresis loop in the response of the sensor device (mesoporous silica thin film with Tween-80 as templating agent) exposed to methanol, ethanol, iso-propanol and n-butanol vapours.*

molecules of the –OH group that can interact in similar manner to water molecule with silica surface groups. Methanol, ethanol, iso-propanol and n-butanol have been chosen because they are highly volatile compounds and they have linear chain that progressively increases.

Alcohol vapours have previously been measured as a function of the carrier stream of nitrogen to obtain a conversion table for alcohol concentration vs. flux (see *Appendix A*): thus the electrical response of sensors has been determined as a in function of alcohol vapour concentration (in ppm)[10].

Better results have been obtained with mesoporous silica film with Tween-80 as the templating agent and using silicon substrates (Figure 59); this could be related to the pore dimensions, which are bigger for the star copolymer if compared with materials synthesized with the other smaller block copolymers. Even if only a small hysteresis loop has been observed between the electrical responses recorded for increasing and reducing RH% value, a wider hysteresis loop can be found for the alcohol vapour measurements. These hysteresis suggest that alcohol molecules are trapped in the pores. Trapping is certainly related to alcohol molecular structure properties like polarity or chain dimensions. Response has not shown substantial changes for subsequent cycling response curves.

4.6 Electrochemical Impedance Spectroscopy measurements

Interesting elucidation on humidity sensing mechanism of some ceramic materials has been obtained using electrochemical impedance spectroscopy (EIS) measurements. This technique allows to separate different electrical contributions of each microstructural component to the total electrical resistance of the material at room temperature. Application of EIS in sensor characterization gives also important information on the nature of its electrical conductivity, capacitance and dielectric constant, correlating them to the processes associated to environmental changes.[11, 12] Recently EIS analysis was used to study the electric properties of a mesoporous acid functionalized silica powder to evaluate its proton conductivity in the presence of water. [13]

Three electrical parameters (complex impedance (Z^*), complex modulus (M^*), and complex relative dielectric constant (k^*)) were used to describe the electrical properties of the sensors at different levels of RH.[14, 15] The "non-Debye" capacitance can be considered, which is given by the relation

$$C_n(\omega) = C(j\omega)^{n-1} \qquad (4.1)$$

where C is a constant, $j = (-1)^{1/2}$, $\omega = 2\pi f$ is the angular frequency (f) and the exponent n is less than one.[16] The measured AC data used to plot in the complex plane diagrams can help in deducing an equivalent circuit model to study sensing membrane. Moreover relative dielectric dispersion is a function of frequency and relative humidity (RH). Finally it can be also evaluated to elucidate the effect of water adsorption on the humidity sensing mechanism. In this terms dielectric loss tangent ($tg\delta$) can also represent the dielectric behavior of the device in different frequency ranges.[17]

EIS was performed in dark conditions and at room temperature (RT) in a testing cell with a working volume of 40 cm^3. Relative humidity (RH) variations from 5% to 90% were obtained by introducing into the cell streams of wet and dry nitrogen, controlling their mixing using an MKS mass flow controller (flow rate = 200 sccm (standard cubic centimeter per minute)). The EIS data, measured in the 10 mHz –10 MHz frequency range and with an amplitude of the applied voltage equals to 1 V, were collected using a Frequency Response Analyzer (Solartron 1255) connected via GPIB with a dielectric interface (Solartron 1296). The EIS data were obtained after increasing and then decreasing RH, att constant values of RH. All EIS data were analyzed using Zview software.

EIS data allow to study both conductivity and dielectric nature of the material. It is known that impedance diagrams allow to derive an equivalent circuit which is associated to a given physical model. Resistance and capacitance are correlated with both conduction and polarization mechanism of the material. Conductivity and dielectric parameters for the films that underwent to different thermal treatments can be derived from EIS data. The frequency dependence of the dielectric constant $k(\omega)$ and the conductivity $\sigma(\omega)$ can be studied separately by different formalisms starting from the same EIS data. In all the following calculations, which needed the knowledge of the cell constant parameter K, we have always considered K = 1 cm^{-1} , due to the difficulties in evaluating the geometrical parameters for the interdigiated electrodes. This assumption was given because the electrode geometry used was identical and the average films' thickness was supposed almost equal for all the specimens Therefore $k(\omega)$ and the conductivity $\sigma(\omega)$ can be directly related to C and R extracted from complex impedance values.

It is important to note that, in own case, for values of resistance larger than 10^9 Ω (measurement device upper limit) the value of R was calculated by an extrapolation of the

impedance diagram. Also, the constant phase element (*CPE*) parameters (Z_{CPE}) can be evaluated from the impedance diagram fits. The distribution time constants represented by the *CPE* impedance can be substituted by a capacitor and a decentralization angle (β), where β values are related to the sample heterogeneity and are related with the distribution time constants. The capacitance (C) values were calculated from the relation

$$C = \frac{1}{(\omega_0 R)} \tag{4.2}$$

where ω_0 is the frequency for maximum imaginary part of impedance of the *R*//*CPE* circuit. The decentralization angle values were calculated from the relation β=90(1-n)

$$\beta = \frac{\pi}{2}(1 - n) \tag{4.3}$$

where n can be extracted form the relation

$$A_{CPE} = \frac{\omega_0^{-n}}{R} \tag{4.4}$$

where A_{CPE} and n are the *CPE* parameters.

4.6.1 Conductivity

Devices conductivity was directly extract from the resistance in equivalent circuits evaluated from impedance diagrams. A resistance (R) in parallel with a constant phase element (*CPE*) was used for all measurements in the different RH conditions to fit impedance diagrams points at higher frequencies. In dry conditions (dry N_2 flux; measured RH lower than 10%) materials shown only one incomplete semicircle with high real axis intercept resistance (R higher than 10^{11} Ω). In this case R and *CPE* elements led to highest deviations from experimental data, while, for RH > 10%, the measure accuracy strongly increase.

The variation range of the resistance (high real axis intercept semicircle) and capacitance (mean values at relaxation frequency) for each devices in the range 20%< RH < 80% values are shown in Table 3. Films treated at 250 °C (250MPS), 350 °C (350MPS) and 450 °C (450MPS) change their resistance through six orders of magnitude with RH while their capacitance values resulted nearly constant for every sensor (around 10^{-12}F). Moreover, it is shown how the relaxation frequencies, related to the semicircle, decrease with increasing RH values. All the devices showed a comparable behavior for the RH > 20% while the time constants were evaluated to be around 10^{-5} sec in RH saturation limit (RH around 80%) where conduction mechanisms are strongly related to the water sorption conditions. Slight variation

for the 450MPS capacitance values can be probably attributed to a geometrical modification of the film for higher thermal treatment. In fact, shrinkage of the mesoporous silica film with a modification after the calcination of the mesochannels order[18] has been reported in previous chapter.

	RH%	***R***[Ω]	***C*** [F]	f_{max} [Hz]
250°C	5 20 30 50 70	$2.28\cdot10^{12}$ $3.8656\cdot10^{10}$ $3.5883\cdot10^{9}$ $1.0308\cdot10^{8}$ $3.4086\cdot10^{6}$	$8.24\cdot10^{-13}$ $5.97\cdot10^{-12}$ $5.61\cdot10^{-12}$ $5.67\cdot10^{-12}$ $5.8\cdot10^{-12}$	10^{-1} 5 50 $1.7\cdot10^{3}$ $5\cdot10^{4}$
350°C	5 15 30 50 70 90	$1.5273\cdot10^{11}$ $1.271\cdot10^{10}$ $3.8798\cdot10^{8}$ $5.4766\cdot10^{7}$ $1.9639\cdot10^{6}$ $3.32\cdot10^{5}$	$5.58\cdot10^{-12}$ $6.02\cdot10^{-12}$ $6.36\cdot10^{-12}$ $6.03\cdot10^{-12}$ $6.23\cdot10^{-12}$ $6.60\cdot10^{-12}$	2 10 20 $5\cdot10^{2}$ $1.6\cdot10^{4}$ 10^{5}
450°C	5 20 30 50 70 90	$5.11\cdot10^{-10}$ $1.73\cdot10^{8}$ $2.78\cdot10^{7}$ $2.51\cdot10^{6}$ $2.89\cdot10^{5}$ $1.14\cdot10^{5}$	$5.33\cdot10^{-12}$ $6.11\cdot10^{-12}$ $6.05\cdot10^{-12}$ $5.93\cdot10^{-12}$ $6.19\cdot10^{-12}$ $6.34\cdot10^{-12}$	3.68 $2\cdot10^{2}$ 10^{3} 10^{4} 10^{5} $2.5\cdot10^{5}$

Table 3 *Variation range of the resistance (high real axis intercept semicircle) and capacitance (mean values at relaxation frequency) for each devices changing Relative humidity value.*

Figure 60 shows a comparison between the impedance diagrams of the mesoporous silica (mesoporous silica) films calcined at 250 °C, 350 °C and 450°C, measured at about 50% relative humidity (RH) and room temperature (RT) stable values. In such case two contributions to the impedance can be found in figure 60. First contribution at low frequencies (f < 10 Hz for both 250MPS and 350MPS, $f < 10^2$ Hz for 450MPS) is attributed to the polarization of the electrodes. The second one, a semicircle at higher frequencies ($10^7 < f < 10^2$ Hz for 250MPS and 350MPS and $10^7 < f < 10^3$ Hz for 450MPS) is related to a charge transfer process.

A resistance (*R*) in parallel with a constant phase element (*CPE*) can be easily used to fit obtained impedance response: straight lines in figure 61 indicates fit for 450MPS. This high frequency contribution is probably related to the ionic relaxation in the pores. While dense silica is an insulator, mesoporous silica has a large specific surface area due to porous inner space that can be thought as a cubic ordered path where charge transfer takes place. Complete resulting equivalent circuit is therefore the parallel of a resistance and a capacitance in series

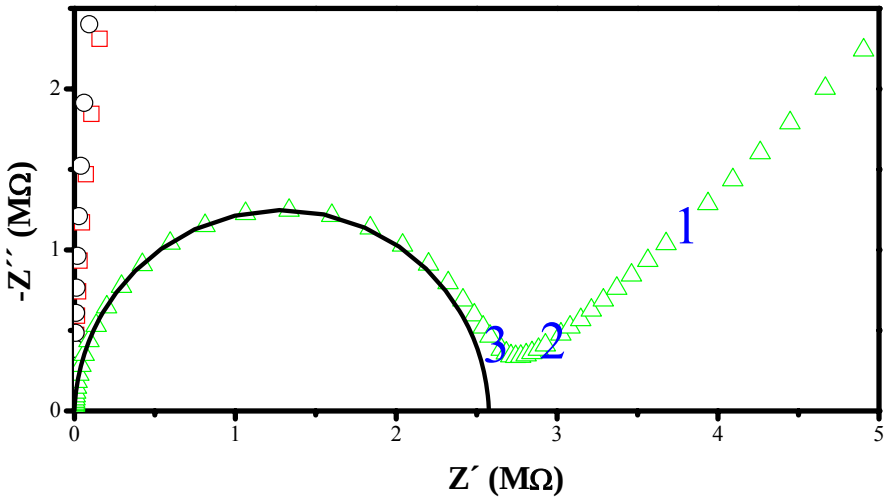

Figure 60 *Impedance diagrams of the mesoporous silica films calcined at 250 °C, 350 °C and 450°C (50% relative humidity and room temperature).*

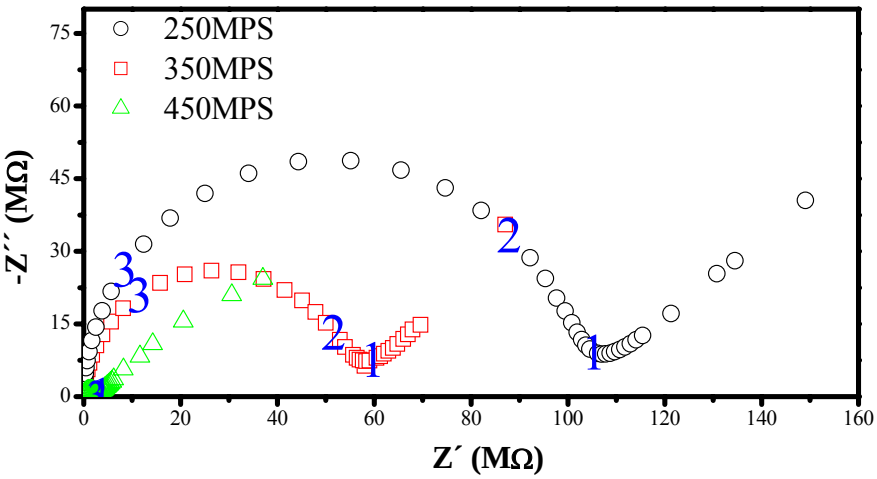

Figure 61 *Impedance diagrams of the mesoporous silica films calcined a 450°C (50% relative humidity and room temperature).*

with a infinite Warburg element. The *R*//*C* element is directly associated to the water adsorbed at the pore and the film surface. Migration phenomena leads to a liquid electrolyte-like behaviour. While the Warburg element is related to the Nernst layer at the blocking gold electrodes. The mesoporous silica thermal treatment changed the sensor electrical response both for the resistance values and the times' constant involved. The electrical resistance decreasing observed for the sample calcined at 450 °C if compared to other sensors can be explained by the lower surfactant content as the result of better organic mesophase removal with a higher thermal treatment, confirming that a good accessibility of the porous network to the external changes is useful to optimize the use the material as sensing membrane. A slight different distribution of frequencies for the 450MPS respect of both 250MPS and 350MPS can be correlated to a different clustering of the water molecules onto porosity surface which can directly affect proton conduction mechanisms. Dissimilar coordination state between H_2O molecules, Si-OH and Si-O-Si groups at the pore surface has bees detected by FT-IR analysis for mesoporous silica films calcined at different temperatures. Not only thermal treatment but also RH causes change in frequencies distribution.

Figure 62 shows imaginary part of impedance *–Z''(f)* for 350MPS taken in some RH values where it can be observed how, varying the humidity level of the chamber, the *–Z''* maximum (corresponding to the apex of the semicircle) changed relaxation frequency values. Such effect can be related to different clustering of water molecules at different level of adsorbed water

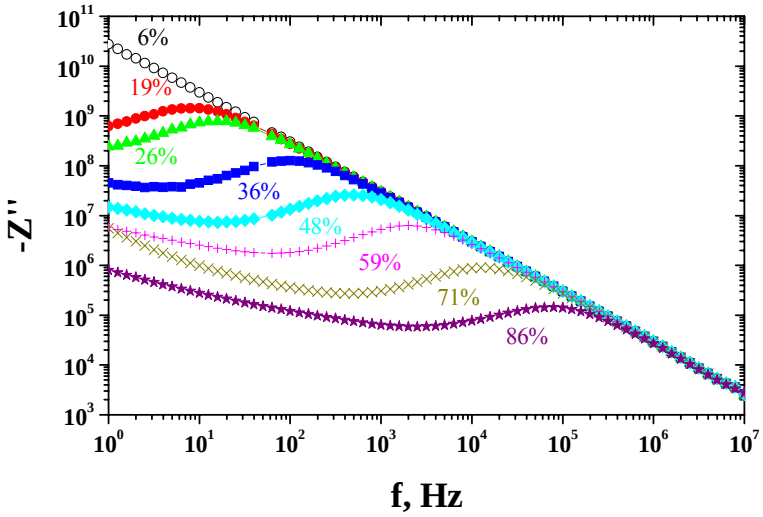

Figure 62 *Imaginary part of impedance –Z''(f) for 350MPS taken: varying the humidity level of the chamber, the –Z'' maximum (corresponding to the apex of the semicircle) changes relaxation frequency values.*

amount (mono- o multilayer). In fact Grotthus model is based on the dipole-dipole interactions of the water which directly control the proton migration through ice-like layered water. Figure 62 shows how this mechanisms are faster (higher frequencies) for bigger amount of adsorbed water.

No others charge transport phenomena are detected from impedance spectroscopy at high frequency and only one semicircle can be extract from impedance diagrams. Figure 63 shows

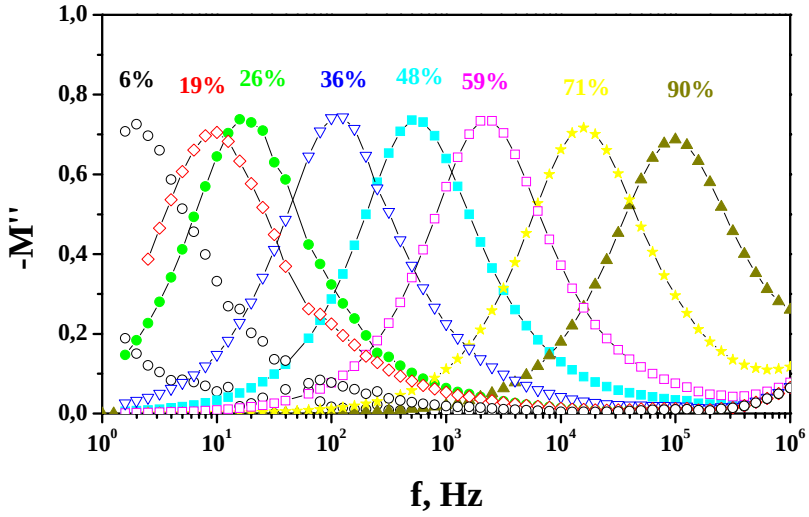

Figure 63 *Imaginary part of modulus M for the sensor calcined at 350 °C.*

the spectroscopic plot of imaginary part of modulus for the sensor calcined at 350 °C. A comparison between *–Z''(f)* (figure 62) and *M''(f)* (figure 63) confirms the presence of only one maximum point for the imaginary component of impedance. Modulus plot pick out those elements with smallest capacitance since the M'' peak maximum is equal to $\varepsilon_0/2C$ for each particular element[19]. Thus, in the sensor, single peak is related to a unique relaxation time of the *R*//*C* element at higher frequencies for every RH value. This phenomenon can be assigned both to a single polarized species contribution and homogeneous charge transport at the pore surface. *M''(f)* maximum shift from low frequency to higher frequency increasing RH value. This can be correlated to a faster alignment of dipoles to the field applied as a consequence of a better mobility of layered water. The absence of relaxation effects at lower frequencies, for RH > 50%, better confirm a dependence of the electrodes phenomena to diffusive and mass transfer mechanisms.

Conductivity can be evaluated by figure 64 which shows the electrical resistance variation of 350MPS with the RH values, measured in a stable condition of RH described upon increase or decrease of RH. A very large electrical resistance variation of six orders of magnitude, from 10^5 Ω to 10^{11} Ω, was observed, indicating the good sensitivity of the device to the RH concentration.

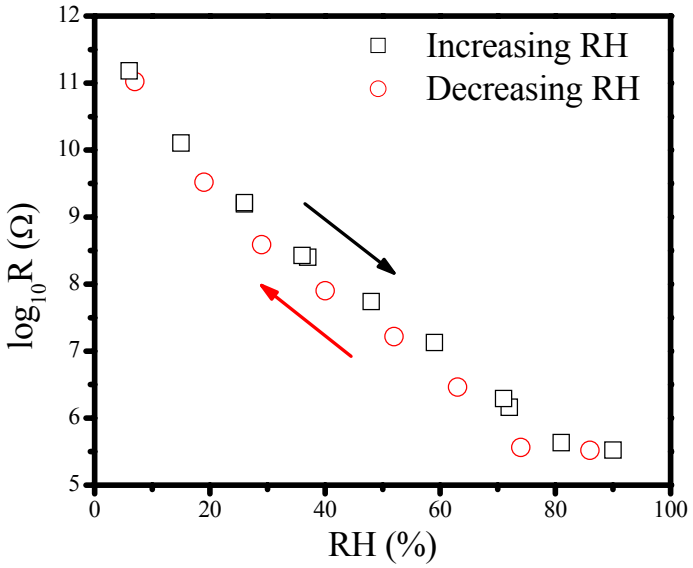

Figure 64 *Electrical resistance variation of 350MPS with the RH values*

Another feature of Figure 64 for RH values above 75% was a saturation limit as observed both for decreasing and increasing RH conditions. The linear fit of the resistance values below this saturation threshold shows a convergence to a same resistance value in 0% of RH. The saturation observed at values of RH>75% is probably caused by the complete filling of the porosity of the mesoporous silica thin film by water. This suggests that the amount of water adsorbed can influence the conduction in mesoporous silica materials: at low RH the water adsorbed can form a layer of clusters along the pore walls; at higher RH values new water molecules start filling the porosity trough capillary condensation where there are the charge carriers[20].

From FE-SEM (figure 65) tubular mesostructured pore size obtained by Pluronic F-127 was evaluated to be around 5nm. The quantity of condensed water depends on the available

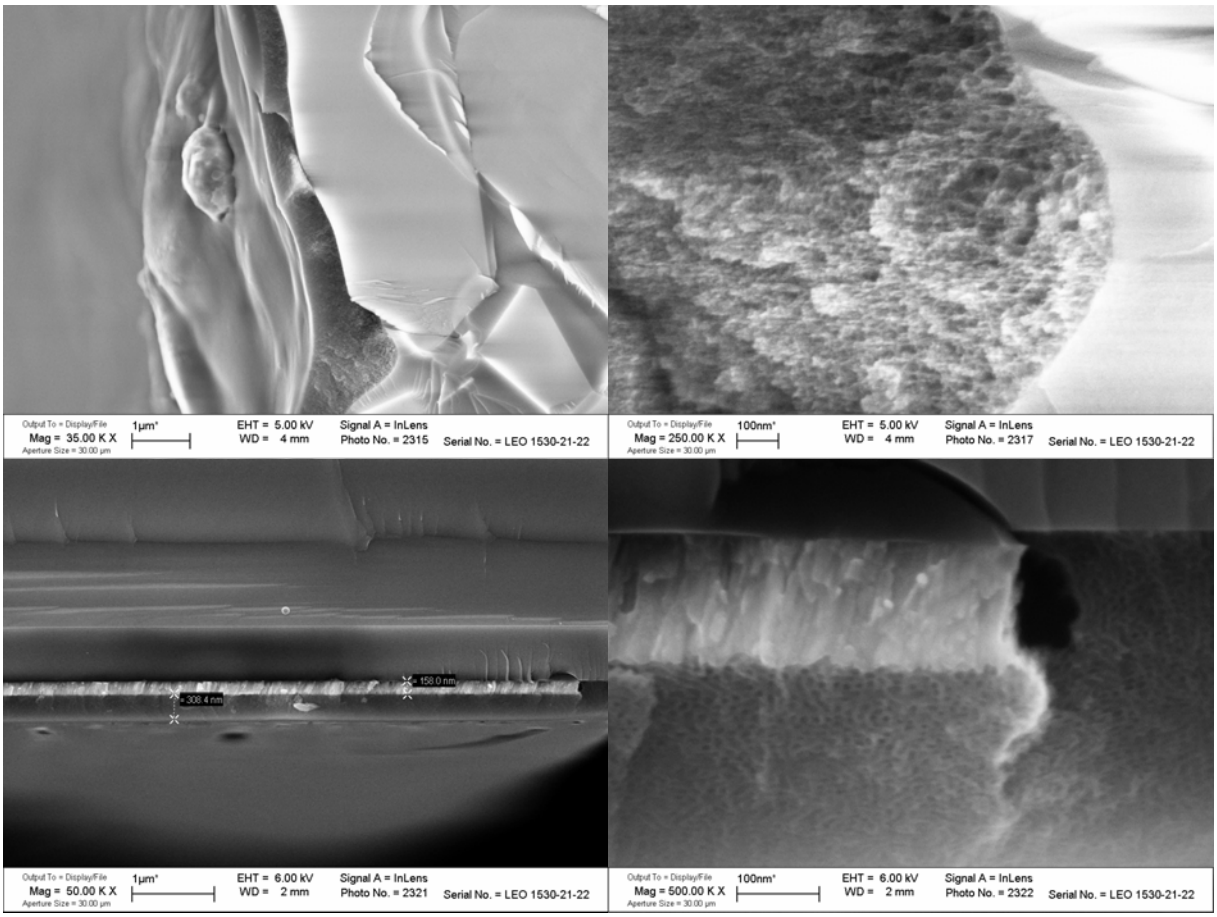

Figure 65 *FE-SEM images (sequential reducing scale) of mesoporous silica thin film on silicon substrate.*

pore sizes and their distribution. It is possible to evaluate the pore radius at which capillary condensation occurs at different temperatures (T) by using the Kelvin equation[21]:

$$\ln\left(\frac{P_s}{P}\right) = \frac{2\gamma M}{r_K RT\rho} \qquad (4.5)$$

where r_K is the Kelvin radius, P is the water-vapor pressure, P_s is the water-vapor pressure at saturation and γ, ρ and M are the surface tension, density and molecular weight of water respectively. Being $(P_s/P)\cdot 100$ equal to RH (%), for a temperature of 28 °C and with r_k = 2.5 nm , condensation occurs at RH = 73% which is very close to the experimental material's saturation limit found for the devices. This confirm that it is probably that pores are completely filled with liquid water already at 75% RH, and thus no conductivity change are observed above this RH value.

Further interesting feature in figure 64 is that EIS measurements performed at constant value of RH, in both drying (decreasing of wet N_2 flux) and wetting (increasing of wet N_2 flux) cycles, shows a slight resistance displacement. This small hysteresis in the electrical

response of the sensor for different values of RH was performed in static condition describes above.

4.6.2 Dielectric constant

EIS data processed and presented in the complex modulus showed clearly how the Z'' plot (figure 62) contains a single relaxation peak, corresponding to the semicircle of the electrolyte in the Nyquist plot (figure 60 and 61). Moreover, imaginary modulus part -*M*'', in figure 63, shows only one peak which can be matched to the imaginary component of impedance *(-Z'', f)* as the equivalent circuit relaxation frequency.

As described, the semicircle was associated to the charge migration phenomena on the mesoporous silica pores' surface which can be related to Grotthus mechanisms while the line at lower frequencies is related to the electrodes polarization. The whole equivalent circuit model must be evaluated in terms of both these phenomena.

It is known that electrodes polarization mechanisms happen at electrodes-electrolyte interface and Warburg element can be used to model the blocking effect of the electrodes, the charge and mass transfer at the Nerst layer. In mesoporous silica films both *R*//*C* and Warburg elements are strongly affected by the water vapor content in the test chamber. As shown in table 3 relaxation frequencies change at different RH values and mesoporous silica film dielectric properties vary with RH% as observed in *-Z''(ω)* and *-M''(ω)* relations. Thus, while sensor capacitance is nearly constant the dielectric properties of the material are related to the AC frequencies. The devices geometrical parameters (cell constant parameter $K = A/l$) can be considered unvarying for the device at different test' conditions while the dielectric properties can be analyzed in terms of the complex dielectric relative constant

$$k^* = k' - jk'' \tag{4.6}$$

where *k'* is the real part, *k''* the imaginary part and $j = (-1)^{1/2}$. Tseng showed how the relative dielectric dispersion at low frequencies can be evaluated to be

$$k'(\omega) \approx \frac{l/A}{\varepsilon_0 (R)^2 C_1 \omega^{n_1+1}} \tag{4.7}$$

where *R* is reduced to the electrolyte resistance and *l/A* is constant cell parameter, C_1 and n_1 from C_{en} non-Debye capacitance related to the device: $C_{en} = C_1 \omega^{n_1+1}$.

$$C_{en} = C_1 \omega_1^{n+1} \tag{4.8}$$

The equation (2) indicates that $k'(\omega)$ is inversely proportional to C_1, ω^{n1+1} and R^2 at low frequencies.

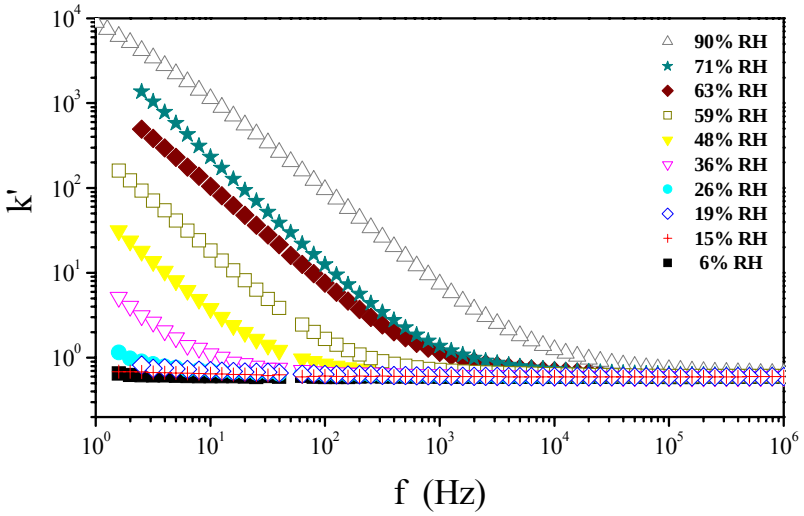

Figure 66 *Real part of complex dielectric relative constant K^* at fixed relative humidity value:dependence from frequency for 350MPS sample.*

The dependence of the k^* to the frequencies was evaluated from the impedance spectra data collected at different RH values by a different formalism using a unitary cell constant. In figure 66, $k'(f)$ is shown the plot for 350MPS in 6% < RH < 90% range. $k'(\omega)$ was evaluated to be proportional to $\omega^{-1.21}$ and n_1 is 0.21 at the lower frequencies. It can be observed that films' dielectric dispersion starts at higher frequencies for higher RH values and that deviation from the k' constant value ($k' = 0.6$) can be observed for this sample even for RH of 26% at low frequencies (starting from 20 Hz). The deviation from $k' = 0.6$ reached $k' = 10^4$ for RH = 90% at 1 Hz while the dielectric dispersion started at 10^5 Hz. A constant slope and a wide k' dispersion for all calcination treatments were observed.

Figure 67 shows $k'(f)$ the same plot for 250MPS at different RH stable value. The device shows a constant k' value around 0.6 in dry condition and at the higher frequencies for all the RH values. Such a value was common to all the calcination treatments. Analogously to the 350MPS (Figure 66), 250MPS $k'(f)$ dependence is strongly related to the RH with $k'(f)$ slope which is nearly constant (-1.21).

Such a dependence of *k'* to the frequencies at the different RH is clearly related to the water adsorbed to the sensor. A high polarization of adsorbed water is even possible at low RH value because of high surface area of the silica films. In the electrode polarization region adsorbed water molecules reorientation is more relevant because of long time constant involved. For those mechanism layered, single and double linked molecules can rotate by the

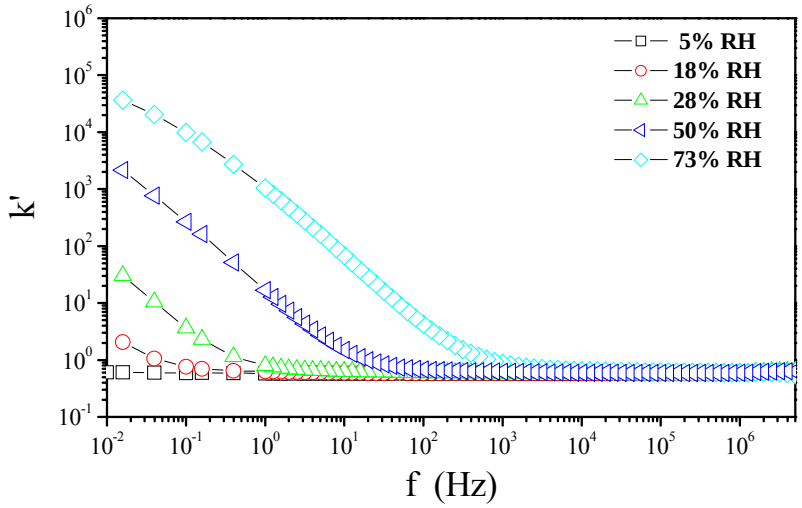

Figure 68 *Real part of complex dielectric relative constant K^* at fixed relative humidity value: dependence from frequency for 250MPS sample.*

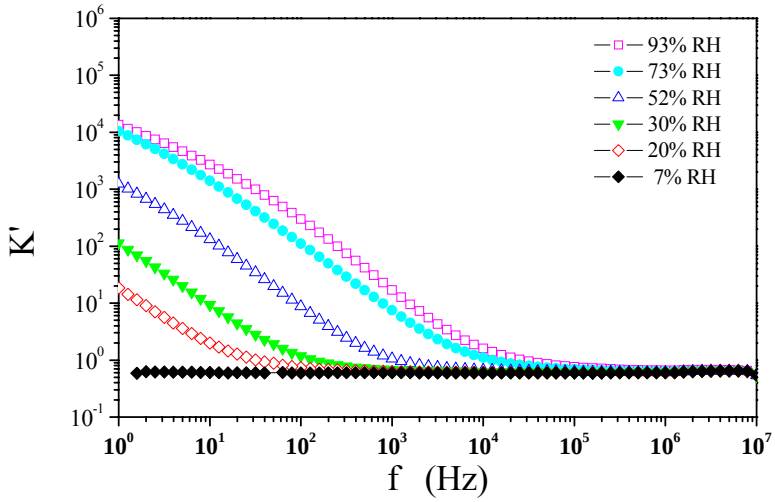

Figure 67 *Real part of complex dielectric relative constant K^* at fixed relative humidity value: dependence from frequency for 450MPS sample.*

field applied. Many ceramic materials based humidity sensors showed such properties. Tseng et al. applying TiO_2, $Ba_{0,5}Sr_{0,5}TiO_3$ as humidity sensor found this kind of trend but only at RH values around 65%

In figure 68 is shown *k'(f)* at different RH value for the film calcined at 450°C. In such a case the *k'* dispersion is also relevant at low RH: the dielectric dispersion starts at 100 Hz for RH = 20% and k' = 20 for *f* = 1Hz while k' remains unvaried for both 350MPS and 250MPS. The polarization mechanism for 450MPS are faster (higher frequencies) at low RH than for 250MPS and 350MPS.Moreover, in figure 8, the *k'(f)* slope smoothly changes from –1.21 to –0.64, at low frequencies, for RH > 50% . In such a case a different adsorbed water molecules configuration can be considered as a consequence of a different chemical composition of the silica pore walls surface due to the higher thermal treatment.

A comparison of *k'(f)* at RH = 50% between each devices is shown in figure 69. It can be observed that, at high frequencies, dielectric constant is the same for each sensor (*k'* = 0.6) while the response change at low frequencies in different ways depending on the calcination treatments. The 450MPS changed faster the *k'* rather than 350MPS and 250MPS. This effect must be related to the active surface available after an almost complete surfactant removal from the film. A slight variation of the *k'(f)* slope for the 450MPS sensor was observed in lower frequencies for RH > 50%. It might be related to a different orientation kinetics of layered water on the mesoporous silica pore walls surface and to a higher charges diffusion at the polarized electrodes. Charge concentration and mobility are slightly larger for 450MPS

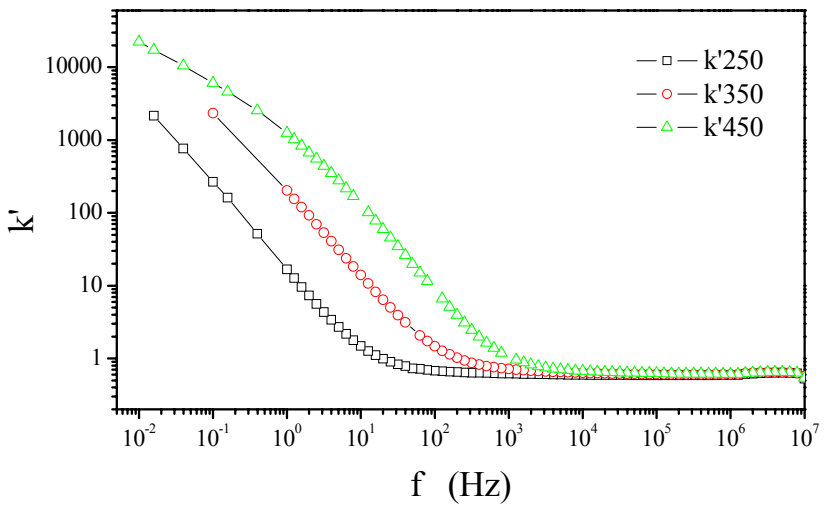

Figure 69 *Comparison of k'(f) at RH = 50% of each sample.*

than for 350MPS and 250MPS (table 3).

Figure 70 shows the *log(k')* dependence on RH for the 350MPS and 450MPS devices in three different frequencies 1Hz, 100 Hz and 100 kHz . The water polarization is already relevant starting from t ≈ 10^{-2} sec for both the devices. The dielectric constant varied in more than four orders of magnitude at 1Hz and in almost two orders at 100Hz magnitude from dry condition to around 70% RH. In figure 9 is also confirmed how the 450MPS is more reactive at low RH starting from 100 Hz. Moreover, for RH = 20%, *k'(1 Hz)* is more than one order of magnitude larger for 450MPS than for 350MPS.

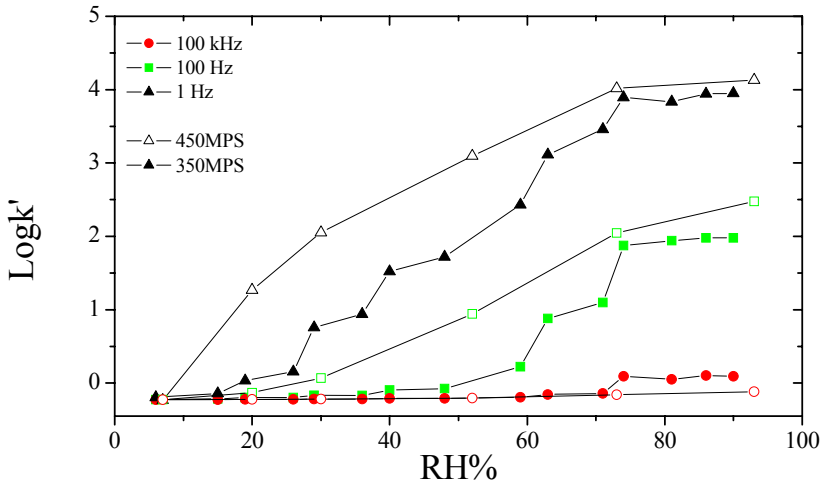

Figure 70 *Log(k') dependence on RH for the 350MPS and 450MPS devices in three different frequencies 1Hz, 100 Hz and 100 kHz*

Figure 72 shows *k''(f)* experimental plot for 350MPS film at different RH stable conditions while figure 71 is a comparison of 250MPS, 350MPS and 450MPS k''(f) plots at 50% RH fixed value. The *k''(ω)* slope at different RH value is nearly constant. The *k''(ω)* in 250MPS, 350MPS and 450MPS is proportional to ω^{-1} in the frequency range from 10^{-1} to 10^{5} Hz as shown in fig 71. The *k''* value showed a slight variation from the exponential value of –1 for f < 4 Hz for 450MPS measured at RH = 93%. This agrees with the measured results as observed in *k'(ω)* plots for 350MPS sensor at different RH values (Figure 66).

Figure 73 and 74 show respectively dielectric loss tangent for 350MPS and 450MPS sensors. The sensor calcined at 350° C showed a continuous increment of the maximum dielectric loss with the RH increment. The frequencies related to those maximum varied in the frequency range in correlation to the RH level. This phenomena is probably due to the different alignment to the field of water in function of their concentration on the mesoporous silica surface and to migration of the free charges at the electrodes. Lower polarization at low

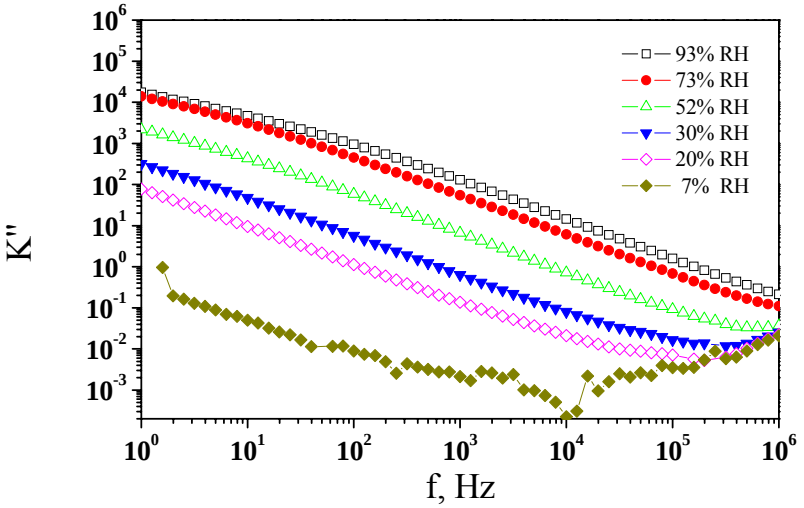

Figure 71 *k''(f) experimental plot for 350MPS film at different RH stable conditions.*

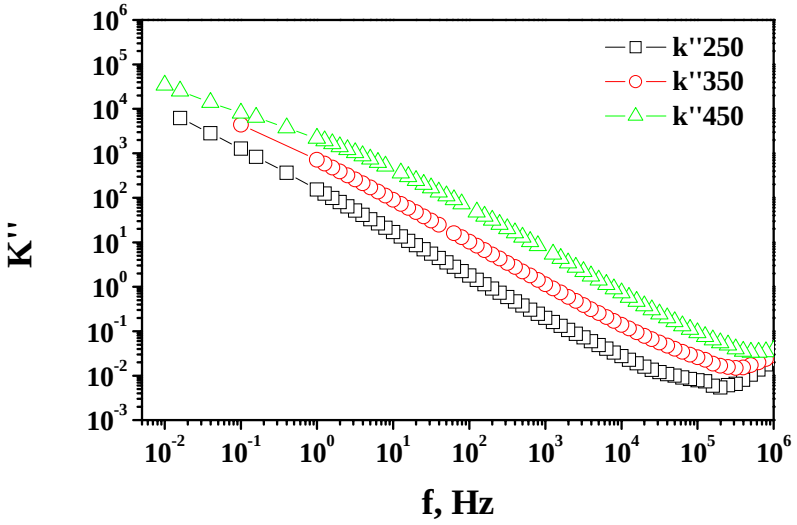

Figure 72 *Comparison of k''(f) at RH=50% for 250MPS, 350MPS and 450MPS*

RH can be attributed to a double link of the molecules on the surface and to a lower concentration of charge carriers accumulated at the electrodes. High resistance values showed above confirm this hypothesis. The sensor calcined at 450°C showed the same trend but the value of the maximum is high also at low RH while decrease at higher RH.

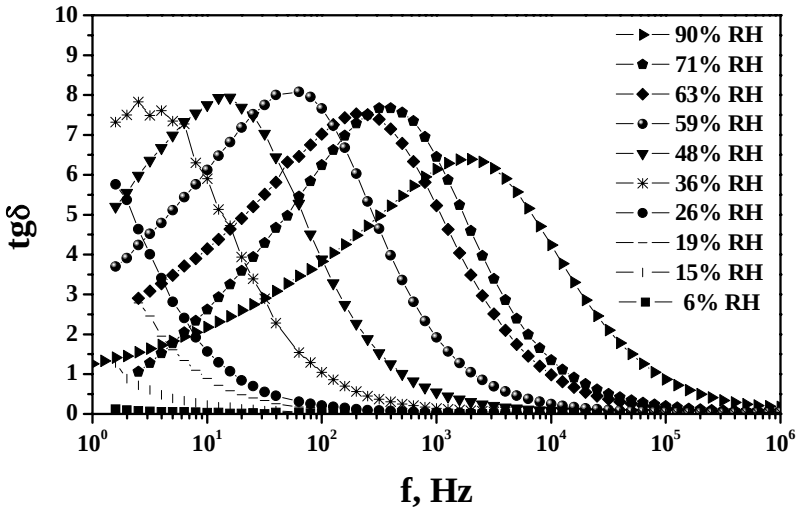

Figure 73 *Dielectric loss tangent for 350MPS.*

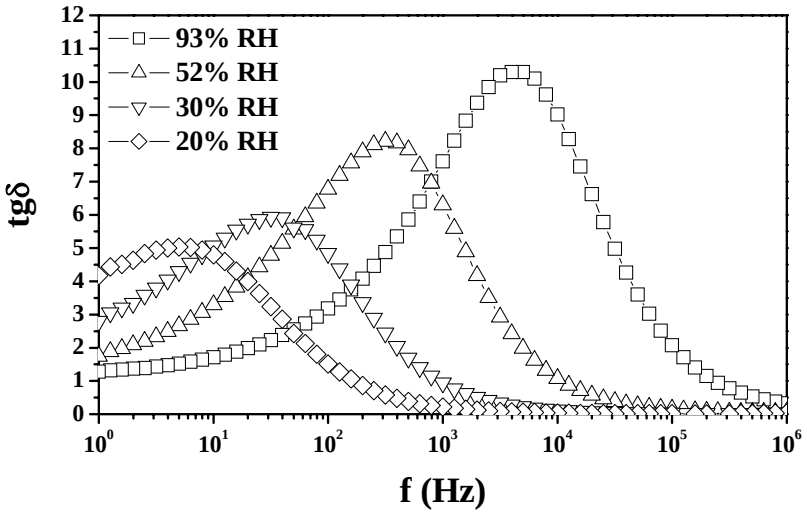

Figure 74 *Dielectric loss tangent for 450MPS.*

The devices 250MPS, 350MPS and 450MPS didn't show the same dielectric dispersion because of their different organic matter content and Si-OH condensation level after calcination.

The impedance diagrams shown the same trend for 350MPS and 450MPS tested sensors in whole RH range while the film calcined at 350°C M''(f) maximum change with the frequencies at different RH values. The relaxation time constant decrease with increasing of RH% while M'' maximum is nearly constant. In the 250MPS, M''(f) changed in non-uniform way probably for a evolution due to the chemical or physical modification of the organic matter left in the film. So morphological properties can affects water absorption-desorption mechanism and specific surface area. Dielectric parameters are probably influenced by both organic content from surfactant and chemical and physical properties of the mesoporous silica film. Different concentration of Si-OH groups on the pores surface at different calcination temperature can be due to a condensation of Si-OH groups in Si-O-Si bridges at the surface. Increasing the Si-OH concentration, the concentration of the single bonded molecules decrease.

References of Chapter 4

1 Wirnsberger, G.; Scott, B.J.; Stucky, G.D. *Chem.Commun.* **2001**, 119.

2 Olson, D.H.; Stucky, G.D.; Vartuli, J.C., US Pat. N. 53644797 (1994)

3 Yamada, T.; Zhou, H.S.; Uchida, H.; Tomita, M. *Microp. Mesop. Mater.* **2002**, *54*, 269.

4 Innocenzi, P.; Martucci, A.; Guglielmi, M.; Bearzotti, A.; Traversa, E.; Pivin, J.C. *J.Europ. Ceram. Soc.*, **2001**, *21*, 1985.

5 Innocenzi, P.; Martucci, A.; Guglielmi, M.; Bearzotti, A.; Traversa, E. *Sens. Act. B*, **2001**, *76,* 299.

6 Yang, C.-M.; Cho A.; Pan F.; Tsai, T.; Chao, K. *Adv.Mater.* **2001**, *13*, 1099.

[7] D'Amico, A.; Di Natale, C. *IEEE Sensors Journal* 1, 183 (**2001)**

[8] Cowin, J. P.; Tsekouras, A. A.; Iedema, M. J.; Wu, K.; Ellison, G. B. *Nature* 398, 405 (**1999**)

[9] Innocenzi, P.; Martucci, A.; Guglielmi, M.; Bearzotti, A.; Traversa, E. *Sens. Act. B* 76, 299 (**2001**)

[10] J. Mio Bertolo, A. Bearzotti and L. Palummo, Proceedings of AISEM 2003, World Scientific Publication – Singapore ***in press***

11. J. R. Macdonald, Impedance Spectroscopy - Emphasizing Solid Material and Systems, Wiley Interscience, New York (1987)

12. C. Gabrielli, " Identification of Electrochemical Processes by Frequency Response Analysis" Technical report number 004/83, Instruments division Schulberber Technologies pag. 13, Issue 2, 1984

13. S. Mikhailenko, D. Desplantier-Giscard, C. Danumah, S. Kaliaguine, Micropor. Mesopor. Mater., **52** (2002), 29

14. Y.-C. Yeh, T.-Y. Tseng, D-A. Chang, J. Am. Ceram. Soc., **73** (1990), 1992

15. Y.-C. Yeh, T.-Y. Tseng, J. Mater. Sci. Lett., **7** (1988), 766

16. Y.-C. Yeh, T.-Y. Tseng, IEEE Transaction on Component, Hybrids, and Manufacturing Technology, **2** (1989), 259

17. G. Gusmano, G. Montesperelli, P. Nunziante, E. Traversa, Electrochimica Acta, **17** (1993), 2617

18. D. Grosso, A.N. Balkenende, P.A. Albouy, M. Lavergne, L. Mazzerolles, *J. Mater. Chem.* **10** (2000), 2085

19. J. T. S. Irvine, D. C. Sinclair, A. R. West, *Adv. Mater.* **2** (1990), 132

20. M. T. Colomer, M. A. Anderson, J. Non-Cryst. Solids **290** (2001), 93

21. H. Arai and T. Seiyama, in W. Göpel, J. Hesse and J.N. Zemel (eds.), *Sensor: A Comprehensive Survey*, Vol.3, VCH, Weinheim, 1992, Ch. 20, pp. 981-1012

Conclusions

Mesoporous silica thin films have been synthesized using supramolecolar self-assembly with block copolymers as structuring agents and have been tested for humidity sensing applications. Humidity sensing devices based on mesoporous silica thin film have been fabricated via dip-coating.

The films have shown completely different response with respect to no-mesoporous silica sol-gel thin film used as reference in testing measurements. The mesophase is easily accessible by the external environment and increases the performances for sensing applications and different types of water molecules are absorbed in the samples upon the different calcination treatments and as a function of the presence of residual surfactant within the pores.

Possibility to obtain different mesophase and therefore mesoporous structure trough change of copolymer molecule has been verified: both hexagonal and cubic order has been observed with several analytical technics. Above all a relatively new instrument based on X-rays energy dispersion has been seen as very interesting one because it give similar information of SAXS measurement but using a simpler and more accessible instrumental set-up.

A different response as function of the surfactant used as templating agent has been observed. A good reproducibility of the electrical response has been obtained. The sensor device has also shown no memory effects after cyclic testing in dry-wet condition and a fast response to change of RH% value.

Moreover, mesoporous silica thin films have shown discrimination between alcohols with different molecular structure.

A substrate dependence of electrical response has been observed and it could be explain by different superficial rugosity between alumina and silicon (that obviously changes the morphology of deposed film) and greater possibility of gold diffusion as ions in the sensing thin film if compared to chromium (that increases the measured current intensity with a fixed applied electric potential).

Silica mesostructured thin films fabricated via evaporation induced self-assembly processes have shown a current response to changes in the external environment larger than 5 orders of magnitude.

Sensing material structure has been studied using energy dispersion x-ray techniques: diffraction and reflectivity spectra has been collected and examined for samples that have been treated at temperature in the 150-1050°C range. Stability of the film structure in air has been observed. An interesting correlation for sensing properties and porosity or silica structural changes has been observed.

We can therefore conclude that mesoporous silica thin film have shown interesting chem-phisical properties useful for sensing applications and overall for relative humidity monitoring.

Appendix A

Evaporation rate determination for water and alcohols in bubbler.

In our sensor testing set-up, we use a bubbling system[1]. A bottle is filled with a liquid (water or alcohol in our case) and a stream of inert gas (nitrogen, for example) is forced to pass through a fritware plunged in the liquid in order to obtain a large number of small bubbles. These bubbles act as molecular carriers, favoring the evaporation as result of the increased liquid-gas surface. The parameters that can be controlled are environmental temperature, flux and pressure of the carrier gas. In order to test a vapour sensor, the obtained vapour charged flux is mixed to a dry inert gas and the total flux is forward to the measurement chamber.

First of all we consider the case of water, in which if we contemplate the *ideal gas equation*

$$p_{H_2O}V = nRT\ , \tag{A.1}$$

the *relative humidity definition*

$$RH = (p_{H_2O} / p_{sat}) \cdot 100 \tag{A.2}$$

and the *molar volume* of an ideal gas, assuming a temperature of 20°C, we have that the relative humidity in the total flux is related to the evaporation rate of water. Its value is function of the instant inert gas flux value by the following mathematical relation

$$\%RH = \frac{p}{p_{sat}} \frac{\Phi_x \dfrac{\Delta M}{M_w \Delta t \Delta \Phi_x}}{4.464 \cdot 10^{-7} \Phi_{tot}} \tag{A.3}$$

where ΔM is the liquid mass loss, M_w the molecular weight, Φ_x the vapour charged flux, Φ_{tot} the total flux in measurement chamber, p the total pressure, p_{sa}t the saturation pressure and Δt the time. The particular case here considered is of primary usefulness since commercial vapour sensors are easily available: this could permit us to control the RH% value obtained by equation (A.3) with the effective value in testing sensor chamber and to evaluate the goodness of our approach to solve the problem.

Likewise, to estimate the alcohol concentration (in ppm) in the total flux we have

$$ppm = \frac{\Phi_x \dfrac{\Delta M}{M_w \Delta t \Delta \Phi_x}}{4.464 \cdot 10^{-11} \Phi_{tot}} \qquad \text{(A.4)}$$

Therefore, in equations (A.3) and (A.4), it is clear the importance of the knowledge of the liquid evaporation rate $\Delta M/\Delta t$ to correctly convert the nitrogen flux value to the effective vapour concentration. From theoretical point of view[2], the water evaporation rate in function of temperature would be expressed with the equation (valid for a free planner surface)

$$\frac{\Delta M}{\Delta t} \approx Ap\sqrt{\frac{M_w}{2\pi RT}} \qquad \text{(A.5)}$$

where A is a constant.

Dynamical weight loss measures at different fixed temperature and gas flux value were performed in order to obtain the temperature dependence of the parameter B, defined as

$$B = \frac{1}{M_w} \frac{\Delta M}{\Delta t \Delta \Phi_x} \qquad \text{(A.6)}$$

so Eq.(A.4) can be expressed

$$ppm = \frac{B}{4.464 \cdot 10^{-11}} \frac{\Phi_x}{\Phi_{tot}} \qquad \text{(A.7)}$$

Our purpose was to verify how this expression is affected by bubbling system and to evaluate if alcohols have a similar behavior to the water one. Temperature dependant measurements to evaluate liquids mass losses for different environmental situations where performed in a suitable climatic chamber.

Experimental set-up is represented in Figure A.1. A filled bubbler was put on a balance in the chamber. The inert gas flux (nitrogen) in the bubbler was maintained at fixed value in the range from 0 to 200 Standard Cubic Centimeters for Minute (Sccm) by a Mass Flow Controller (MKS multi gas controller 147).Temperature was changeable from 15 to 40°C using Peltier Cells and a ventilator; its value is monitored by a Pt resistor. Liquid weight

(water or alcohol) in function of time was recorded by the computer controlled "closed" balance (Sartorius BP221S, max weight 220g, sensibility 0.1mg).

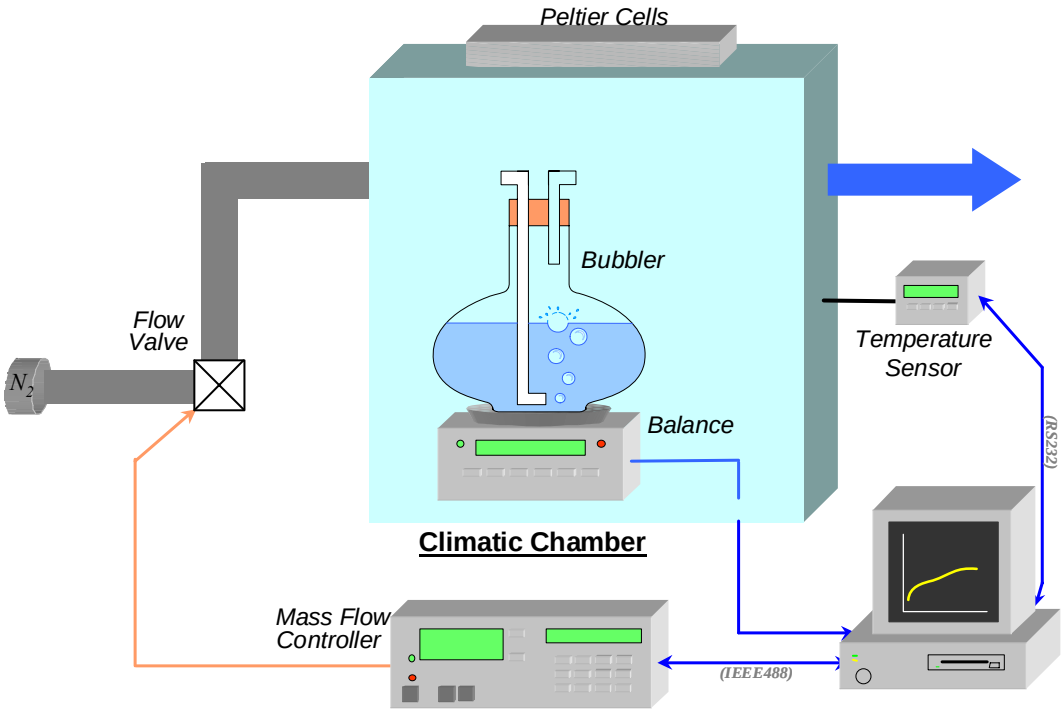

Figure A.1 *Experimental set-up for evaporation rate studies.*

Measurements were performed at ambient pressure in the following steps:

1. By maintaining fixed temperature and flux, we have recorded weight variations vs. time for each liquid considered
2. We have then repeated the previous measurements for different flux values (from 50 to 200 Sccm)
3. All previous steps were performed again at different temperatures (from 15 to 40°C).

Fixing flux value and temperature, liquid weight losses have shown linear time dependence. Moreover, calculated angular coefficient has exhibited a linear behavior versus flux. We have collected data concerning measurements done on five different liquids including water (Figure A.2). B values are been obtained using Eq.(A.6).

We have obtained good approximation between experimental results (given by a commercial humidity sensor) and values obtained by substitution of B values in (Eq.(A.3)). Obtained data were compared with those collected by a commercial humidity sensor

(Honeywell HIH3602C). Ethanol has shown a behavior similar to the water one. Very different results have been obtained for methanol, n-propanol and n-butanol: further studies will regard the causes of this unlike.

	Temperatura (°C)		
	18	23	29
H_2O	$7.7319 \cdot 10^{-7}$	$1.2378 \cdot 10^{-6}$	$2.2591 \cdot 10^{-6}$
MeOH	$3.0866 \cdot 10^{-6}$	$4.0977 \cdot 10^{-6}$	$4.7875 \cdot 10^{-6}$
EtOH	$1.9253 \cdot 10^{-6}$	$2.1380 \cdot 10^{-6}$	$3.3427 \cdot 10^{-6}$
nPrOH	$5.7074 \cdot 10^{-7}$	$1.0250 \cdot 10^{-6}$	$1.6640 \cdot 10^{-6}$
nButOH	$2.9140 \cdot 10^{-7}$	$6.1788 \cdot 10^{-7}$	$6.7859 \cdot 10^{-7}$

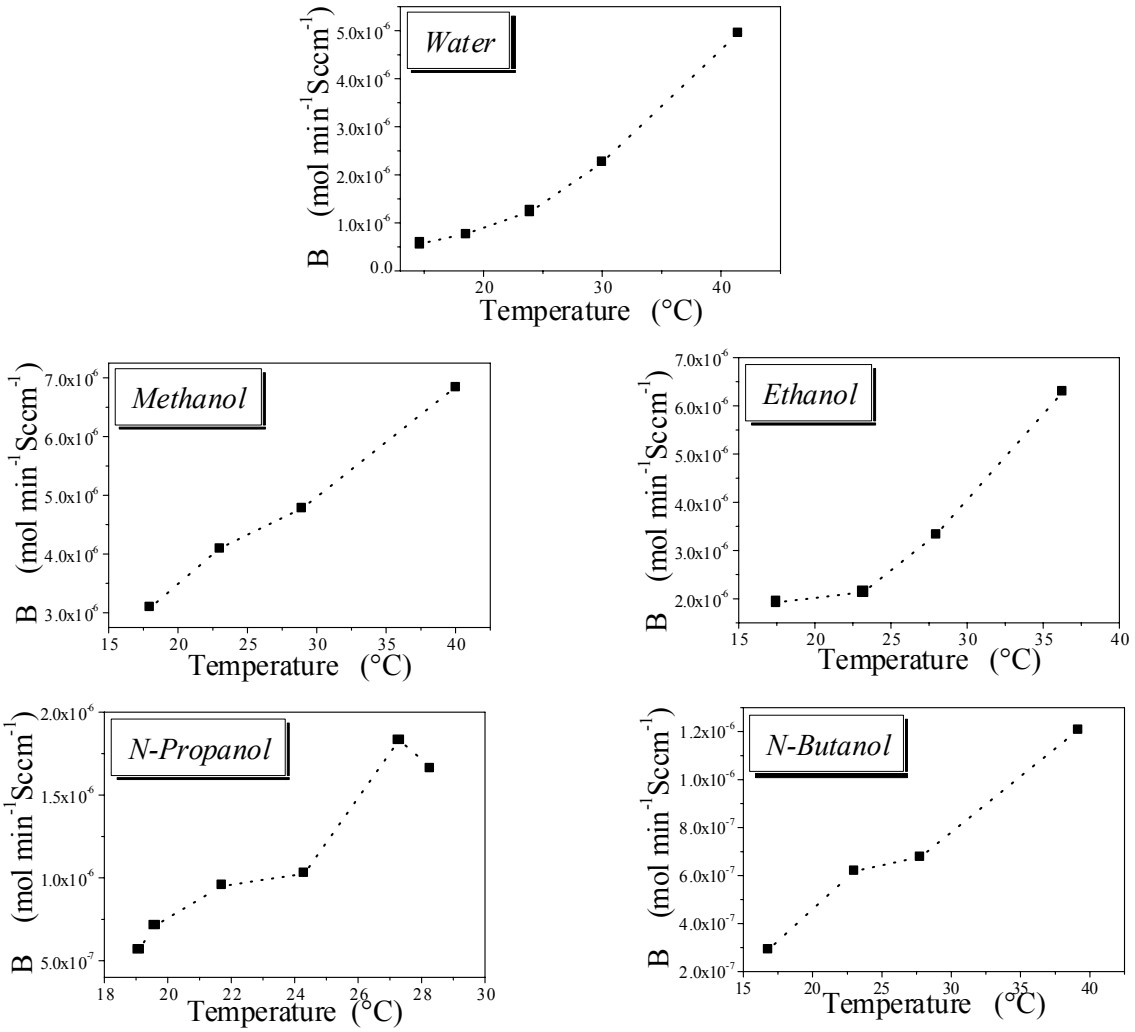

Figure A.2 *Water and VOCs molar evaporation rate vs. temperature*

The obtained B values corresponding to liquid temperature at sensors testing time have been used to convert their responses in function of vapour charged flux (in Sccm) to functions of alcohol vapours concentration (in ppm) using Eq. (A.7).

References of Appendix

1. P. Innocenzi, A. Martucci, M. Guglielmi, A. Bearzotti and E.Traversa, *Sens. Act. B* **76**, 299 (2001)

2. Zemansky and Dittman, *Heat and Thermodynamics,* McGraw (1981)